DEVELOPMENT OF TOOLS FOR MECHANICAL CHARACTERIZATION AND MECHANICAL STIMULATION OF TISSUE ENGINEERED CONSTRUCTS

A Dissertation

by

RAGHUVEER LALITHA SRIDHAR

Submitted to the Graduate and Professional School of
Texas A&M University
in partial fulfillment of the requirements for the degree of

DOCTOR OF PHILOSOPHY

Chair of Committee,	Michael R. Moreno
Committee Members,	Kumbakonam R. Rajagopal
	John C. Criscione
	Andrew B. Robbins
Head of Department,	Guillermo Aguilar

May 2022

Major Subject: Mechanical Engineering

ABSTRACT

Tissue engineering is a rapidly expanding field, with billions of dollars being invested each year. Despite all the attention and the resources expended, applications of tissue engineering technologies in a therapeutic setting is conspicuously limited. This could be because while the response of biological cells to biochemical stimuli has been well studied and understood, the effect of the mechanical environment on cell response has not been explored sufficiently. Cells are mechanotransducers i.e. they respond biochemically to mechanical stimuli. In order to improve the viability of tissue engineering technologies in a clinical setting, there is a need to understand the mechanical behavior of biological tissues and tissue engineering scaffolds as well as study cell response to physiological mechanical cues. This document details experimental validation of a novel theoretical framework for mechanical characterization of soft tissues, and the development of a bioreactor to study cell response to mechanical stimuli.

A QR decomposition of the deformation gradient allows for a novel decomposing any arbitrary deformation into three distinct modes: dilation, squeeze, and shear. The study of biological materials in simple shear is quite complex, and typically the boundary conditions in a rectilinear simple shear experiment are not fully measured. A novel device that produces a simple shear deformation while measuring the loads and the moments applied at the grips is detailed here, along with experimental validation. The three modes of deformation are then applied on silicone to get a sense of the experimental error inherent in the system. Rat skin was then studied in all three modes of deformation, and the resultant stress-strain curves were modelled with the 3 parameters Freed-Rajagopal model extended to 2D planar membranes, thus obtaining 9 material parameters for rat skin. Finally, the design and validation of a uniaxial bioreactor is presented, and its potential use in studying cell response with this novel framework is discussed.

DEDICATION

To friends and family.

ACKNOWLEDGMENTS

I would like to thank Dr. Alan Freed and everyone in the Biomechanical Environments Laboratories (BMEL), especially Dr. Michael Moreno, Dr. Andrew Robbins, Caleb Davis, Shannon Ingram, Zachary Lawson, Ji-Wan Han, and Dr. Mingliang Jiang for all of their help, guidance, mentor-ship, and moral support. This work would not have been possible without all of you.

I would also like to thank Dr. Alan Freed and Dr. Michael Moreno for their support and guidance throughout, on matters in and outside of the research. I am deeply grateful to you both.

Finally, I would like to thank my family and friends who have motivated and supported me throughout the program.

CONTRIBUTORS AND FUNDING SOURCES

Contributors

This work was supported by a dissertation committee consisting of Professors Michael Moreno (chair) of the J. Mike Walker 66' Department of Mechanical Engineering and Department of Biomedical Engineering, Professor Kumbakonam Rajagopal of the J. Mike Walker 66' Department of Mechanical Engineering, Department of Biomedical Engineering, and the Department of Ocean Engineering, Professor John Criscione of the Department of Biomedical Engineering, and Professor Andrew Robbins of the J. Mike Walker 66' Department of Mechanical Engineering, Department of Biomedical Engineering, and the Department of Interdisciplinary Engineering.

The initial idea for the shear device in Chapter 2 was provided by Dr. Alan Freed at Texas A&M, and developed further by Professors Mingliang Jiang at Texas A&M and Professor Andrew Robbins. Dr. Alan Freed was also a primary contributor for all the mathematical models used in Chapters 2, 3, and 4, as well a significant contributor towards the experimental design and subsequent data analysis presented in those Chapters.

Yan Yao at Texas A&M made substantial contributions to the control system code for the uniaxial bioreactor discussed in Chapter 5, and Caleb Davis at Texas A&M performed the experiments and data analysis on the Human Dermal Lymphatic Endothelial cells.

All other work conducted for the dissertation was completed by the student independently.

Funding Sources

Graduate study was partially supported by a Spring 2019 Graduate Excellence fellowship and a Fall 2021 Continuing Student Fellowship from the J. Mike Walker '66 Department of Mechanical Engineering. Additionally, the study was supported by Texas A&M Triads for Transformation Graduate Research Assistantship under Dr. Alan Freed, and a Graduate Research Assistantship under Dr. Michael Moreno.

TABLE OF CONTENTS

Page

LIST OF FIGURES

FIGURE Page

LIST OF TABLES

TABLE Page

1.1 Background

Tissue Engineering refers broadly to the development of tissues and organs that can substitute injured or diseased counterparts [1]. Typically, a scaffold is manufactured using a biodegradable material. Biological cells are seeded on this substrate and subjected to the appropriate biochemical and mechanical environment; this allows them to differentiate and otherwise respond in a favorable way. The cells may then produce their extra cellular matrix (ECM) that replaces the engineered scaffold as it degrades. Optionally, the tissue is then decellularized for further applications.

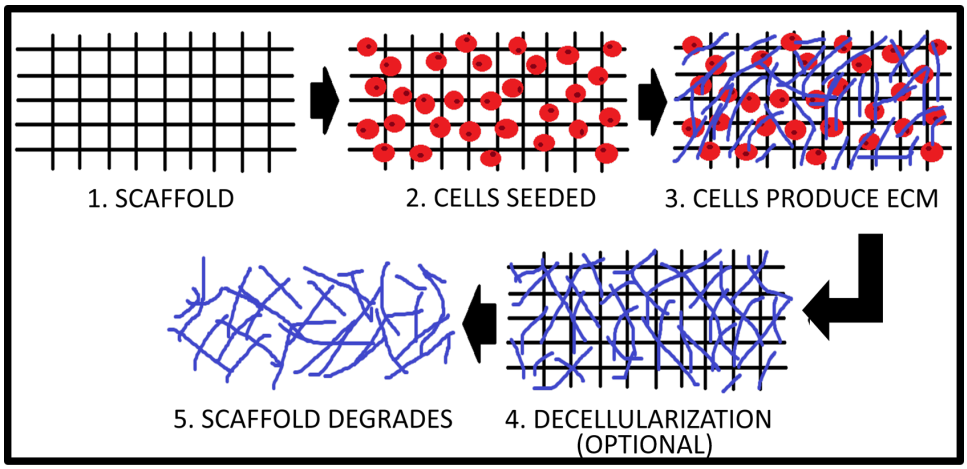

Figure 1.1: A typical tissue engineering work flow

Despite the huge investment of resources in tissue engineering research, there has been relatively low impact therapeutically. This could be because while a lot of effort has been spent understanding the relevant biochemical environments, not a lot of research has been done to properly characterize the mechanical environment and understand the cell response to the complex physiological loading they undergo *in vivo*. Cells are mechanotransducers[2] i.e they

respond biochemically to mechanical stimuli. In order to subject cells to physiologically relevant environments, the mechanical environment in the body has to be well understood, following which the response of particular cell types to physiological mechanical conditions can be studied. Of course, understanding the mechanical environment is merely one of the many challenges faced by tissue engineers [3]. This dissertation chooses to focus on the tools required by tissue engineers to engineer mechanically biomimmetic scaffolds.

1.2 Engineering mechanically biomimmetic tissue scaffolds

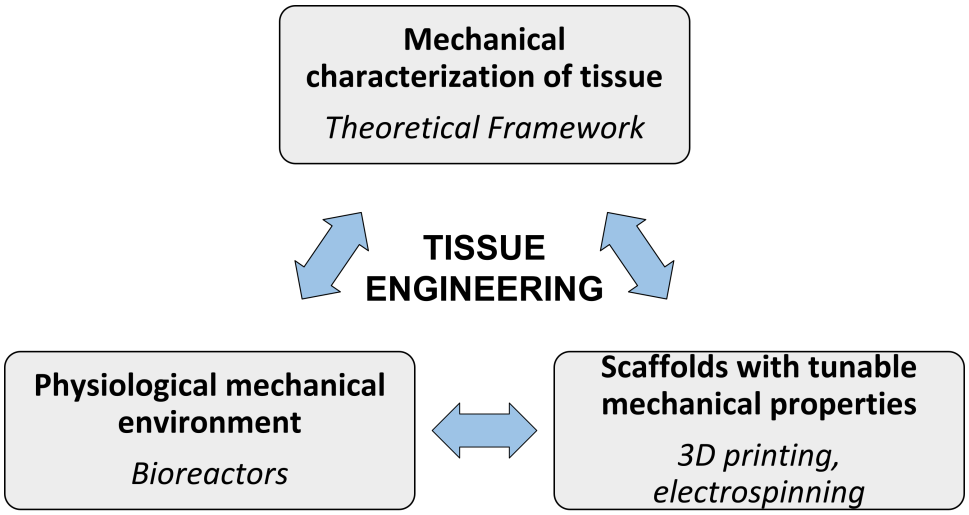

Figure 1.2: Tools for developing mechanically biomimmetic tissues

In order to engineer viable, mechanically biomimmetic tissue, there is a need to:

1. Understand the mechanical properties of the target tissue, and the mechanical environment of the cells *in vivo*

2. Design and fabricate tissue scaffolds with tunable mechanical properties

3. Seed cells on these scaffolds and subject them to the appropriate mechanical (and biochemical) environment

This is a feedback loop, with each step informing and guiding the other two steps.

1.2.1 Mechanical characterization of soft tissue

In order to produce biomimmetic scaffolds, we need to be able to accurately characterize the native tissue. Biological tissues are often characterized using linearized elasticity theories, since the mechanical properties can be obtained using simple uniaxial tensile tests. However, biological tissues are non-linear, anisotropic, inhomogenous, and viscoelastic, thus violating most of the assumptions made in linearized theories. Typically, the non-linear toe region of the stress strain curve is simply ignored, and a Young's modulus is calculated from the linear region. Stiffness measures are insufficient to uniquely characterize this non-linear behavior. In addition, it has been shown that cells are bioactive in the toe region of the curve[4]. By ignoring this region entirely, critical information about cell response to the engineered scaffold is lost.

There have been several theories proposed that try to capture the non-linear behavior of biological tissues[5, 6]. Some of the most used theories however do not provide physically meaningful parameters that a tissue engineer can target. Fung's model (in 3D) for example has arbitrary mathematical constants that are not unique and do not have any physical significance. While these models have great utility in computational endeavors to accurately represent the load-deformation behavior of these tissues, they are not suitable for the forward design context used in tissue engineering.

1.2.2 Fabricating tissue scaffolds with tunable mechanical properties

There have been several methods developed to fabricate tissue engineered constructs: 3D printing[7], electrospinning[8], decellularization of tissues[9], hydrogels[10], etc. Decellularization refers to the process of isolating ECM from harvested tissues and organs by removing the biological cells present in them. It has potential to be highly biomimmetic since it is obtained from the actual tissue in consideration, but the manufacturing method is complex and time consuming. It is also difficult to find mechanical analogues for human tissue in animal models. Electrospinning of tissue constructs is quite popular due to the ease of production, as well as

the ability to produce nano-scale fibers that can interact with cells in 3D. However, it is difficult to accurately control the microstructure with electrospinning. 3D printing offers great potential for fabrication of tissue scaffolds. A variety of biomaterials (like collagen, hydrogels, etc) can be printed with 3D bioplotters, as well as cell-laden bioinks. This technique has great versatility in the architecture that can be achieved in the scaffolds. Sacrificial bioprinting even offers the ability to construct vasculature inside the construct[11].

While there are a variety of methods to produce tissue engineering constructs that are biocompatible and biodegradable, the challenge remains in mechanical biomimmicry. The target tissues are not characterized with physically intuitive and meaningful parameters that offer the tissue engineer guidance towards tweaking the fabrication parameters to achieve the desired mechanical properties.

1.2.3 Understanding cell response to mechanical stimulation

Cells are mechanotransducers. In some cases, it is critical to understand how they react to certain mechanical conditions and whether the response is favorable or adverse to development of the engineered tissue. For this purpose bioreactors are commonly used[12]. Bioreactors are devices that mimic the *in vivo* physiological environment *in vitro*. This includes maintaining the pH, oxygen concentration, CO2 levels, temperature, nutrient transfer, etc. In order to study the mechanotransduction properties of cells, there are several classes of bioreactors[13] that apply some form of mechanical stimulation to the cells as well: tension, compression, torsion, fluid shear, to name a few. The purpose of bioreactors is two fold: First, to replicate *in vivo* conditions so that the cells respond and proliferate as required. Second, to study the response of cells to specific environmental cues. There are a variety of ways in which the cell response is studied: protein expression, gene expression, changes in morphology, collagen production, etc. In tissues that serve a mechanical function in the body, it is of particular interest to tissue engineers to understand how the physiological mechanical environment aids the functioning of that tissue, and which mechanical cues are vital for the development of the tissues *in vitro*.

1.3 Addressing the challenges in Tissue Engineering

A novel theoretical foundation for mechanically characterizing biological tissues and tissue engineered constructs has been developed. It uses the triangular decomposition of the deformation gradient (initially proposed by McLellan[14], rediscovered by Srinivasa[15], and subsequently extended by Freed et al[16]) and implicit elasticity(initially proposed by Rajagopal[17] and used by Freed and Rajagopal[18]) to give physically meaningful parameters based on thermodynamically sound theory. This represents a shift in the paradigm of mechanical characterization of biological tissues.

In order for tissue engineers to start adopting this framework, it first needs to be validated experimentally. The framework decomposes any arbitrary strain into 3 modes: dilation, squeeze, and shear. The material response is studied in these three modes of deformation. This has been explored in the context of 2D membranes, which is relevant for many types of tissues commonly targeted by tissue engineers, such as skin. Here we attempt to perform experiments that validate the theory, establish its usefulness, as well as establish methods and protocols for tissue engineers to test soft tissues and subsequently the engineered tissues. The shear deformation in particular has traditionally been a difficult experiment to perform, but provides invaluable information about the material behavior that can't be obtained in any other mode of deformation.

In order to capture the attention of the tissue engineering community, it needs to be established that the novel theoretical framework proposed is relevant in a tissue engineering design context. For this purpose, bioreactors are needed that can apply apply mechanical cues to cell seeded substrates. If it can be shown that some cell types are responsive to certain parameters in the proposed model, it might further the use and incorporation of these theoretical efforts into design considerations and help fabricate more effective solutions.

1.4 Specific Aims

Broadly, this PhD will be focusing on developing the tools that lead to mechanically biomimmetic engineered tissues. It will focus mainly on validating a promising theoretical framework and model, and will also include some tools to understand the importance of the parameters obtained in this model, and their relevance in tissue engineering. That is, of the three steps discussed in Section 1, steps 1 and 3 are explored here (theoretical framework for mechanical characterization of biological tissues and tissue engineered constructs, and bioreactors for studying cell response to mechanical cues). Accordingly, the following Specific Aims are proposed:

1.4.1 Develop the ability to perform simple shear experiments on soft membranes

This aim will be considered complete when simple shear deformation is applied on 8 silicone membranes, the boundary loads are measured as defined in [19], and statistical analysis is performed on the uniformity of deformation.

1.4.2 Perform dilation, squeeze, and shear modes of deformation in 2D

This aim will be considered complete when 8 sets of silicone membranes are deformed in the three modes of deformation arising from a QR decomposition of the deformation gradient [16], and a 95% confidence interval of the stress-strain curves for the conjugate stress/strain pairs are obtained.

1.4.3 Mechanically characterize a biological tissue in 2D with the Freed-Rajagopal model

This aim will be considered complete when stress-strain curves for the three conjugate stress/strain pairs are generated from 8 sets of experiments performed on rat skin, a total of 9 material parameters are obtained in accordance with the Freed-Rajagopal implicit model for elastic biological tissues[16] (from the 95% confidence intervals calculated for these curves), and the model's viability for rat skin is assessed.

1.4.4 Develop a bioreactor that can apply uniaxial stretch on cell-seeded substrates

This aim will be considered complete when a bioreactor capable of applying physiological uniaxial stretches is developed, the biocompatibility of all the components contacting the cells is verified, and NIH 3T3 fibroblasts are seeded on a suitable substrate and cyclically stretched inside the bioreactor for at least 10 hours, with a subsequent live/dead assay to confirm that the bioreactor is cell viable.

The following chapters will look at each of these aims in detail.

Biological tissues undergo complex deformations physiologically. In order to characterize their mechanical behavior adequately, tests such as uniaxial tensile tests, equi-biaxial tests, confined compression tests, etc. are performed. One of the most challenging tests to perform on soft tissue membranes is the simple shear test. Traditionally, pure shear experiments are performed to obtain the shear modulus. However, it has been shown that the elastic modulus is many orders of magnitude larger than the shear modulus for biological tissues [20] and therefore pure shear experiments are not sufficient. Even in experiments where simple shear is performed, the reaction forces and moments applied by the material on the clamps are typically not measured and so the boundary conditions are insufficient for constitutive modeling.

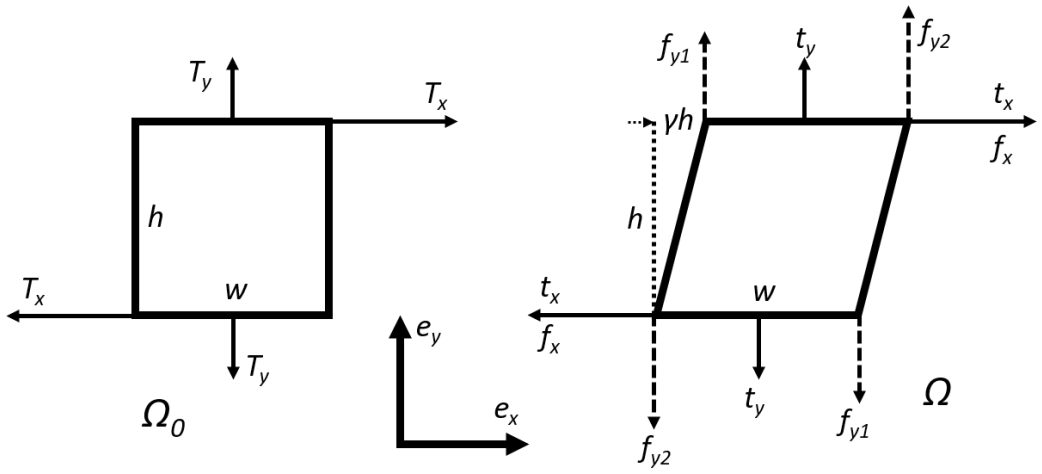

Figure 2.1: Simple shear deformation on a membrane of width w, height h, and thickness d, caused by an applied force f_x. t_x and t_y are tractions applied in the deformed configuration Ω that associate with the pseudo tractions T_x and T_y in the reference configuration Ω_0. γ is the shear strain produced here.

Freed [19] describes the proper way to populate the Kirchoff stress tensor in a rectilinear simple shear experiment on an isotropic material. We consider the experiment depicted in

Figure 2.1. The Kirchoff stress tensor is then given by

$$[s] = \begin{bmatrix} s_{11} & T_x & 0 \\ T_x & T_y & 0 \\ 0 & 0 & 0 \end{bmatrix} \tag{2.1}$$

where the $T_x = f_x / wd$ and $T_y = (f_{y1} + f_{y2}) / wd$ are the tractions imposed on the surface with initial area wd. In the case of a hyperelastic material, $s_{11} = T_y + \gamma T_x$. Internal tractions are carried by the gripping surfaces, with T_{xin} and T_{yin} acting on material surfaces oriented along the x-direction. T_{xin} cannot be resolved from boundary conditions, while $T_{yin} = (f_{y1} - f_{y2}) / wd$

In order to properly populate the Kirchoff stress tensor for use in constitutive modeling, the forces applied on the clamps f_{y1} and f_{y2} have to be measured as well. Here, a novel apparatus that can apply simple shear on soft membranes is described, several simple shear tests performed on silicone and rat skin are discussed, and the results are analysed.

2.1 Device requirements

The following considerations were used while developing a shear testing device:

1. Device must be able to perform large shear strains
2. Device must be able to measure the f_x, f_{y1} and f_{y2} loads (Figure 2.2).
3. Device must be able to apply rectilinear simple shear without any other mode of deformation

2.2 Device description

The main components of the device are illustrated in figure. It consists of 3 sets of clamps - a relatively thin middle clamp and two transverse clamps. A 4-bar linkage is made, with the clamp attached to the transverse linear actuator with 2 links of equal lengths, ensuring that it remains parallel to the other clamps. The links pivot on rotary and thrust bearings as shown, with load cells attached to one set of these links. The LVDT rod is screwed to a carriage mounted

on a linear slide attached to the transverse clamps. The sample is clamped in a double lap shear configuration to balance the moments applied by the material on the central clamp. The central clamp is moved by a linear actuator to produce the shear deformation, with the attached load cell measuring fx. Load cells mounted on one set of the 4-bar linkage measure the reaction forces and moments applied by the material on the clamps. The LVDTs connected to the transverse clamps using linear rails and carriages provide feedback to the transverse linear actuators. As the central actuator moves and produces a shearing motion, the motion of the 4-bar linkages cause the clamps to swing in that direction and attempt to stretch the material. But the attached LVDTs measure this movement and allows the transverse linear actuators to move in accordingly, thus avoiding any stretching of the material in the transverse direction. An overhead camera attached to the central actuator captures images at regular intervals for Digital Image Correlation (DIC) analysis. A comprehensive breakdown of the parts, and engineering drawings are attached in Appendix C

2.3 Methods

In order to evaluate the repeatabilty of the experimental setup, shear tests were performed on a commercially available "engineering" material, i.e. silicone, that can be reasonably assumed to have uniform properties across multiple specimens. Following this, shear tests were also performed on rat dorsal skin, to evaluate the utility of this device with biological tissues. The biaxial testing platform has been previous described in [21], and this testing set-up was mounted on this system. During the application of the shear deformation, the linear motion of the central clamp is controlled, with the transverse clamps "following" due to the action of the 4-bar linkages. This means that a predetermined shear "strain" cannot be applied; the central clamp is moved for a fixed distance and DIC analysis is used after the test to measure the shear strain produced. For all samples, 3D printed jigs were used to position the clamps and the samples relative to one another consistently each time to get the correct gauge length of clamping.

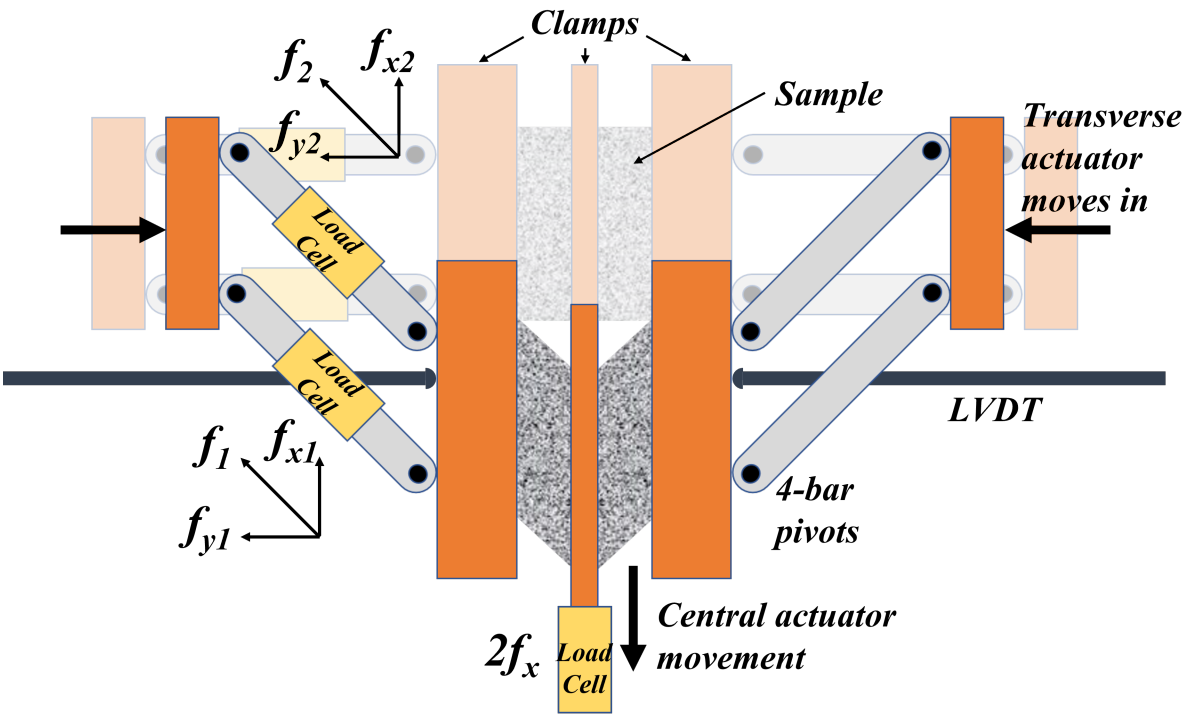

Figure 2.2: Schematic of the apparatus. f_1 and f_2 are load cell measurements which are decomposed to determine f_{y1} and f_{y2}.

2.3.1 Test protocols

2.3.1.1 Silicone

Clear silicone sheets were obtained from McMaster-Carr Supply Company, Elmhurst, IL, USA (Catalog # 86915K12), with nominal thickness measured with vernier calipers to be 0.72mm. Samples of size 44.45mm by 41.91mm were laser cut from the sheet. A speckle pattern was produced on the samples using black spray paint (Universal Premium Spray Paint, Flat Black, Rust-Oleum, IL, USA). They were then clamped and mounted on the system, with the samples being nominally 44.45mm wide and 4.445mm long between the central and transverse clamps (with an aspect ratio of 10:1). Sandpaper was glued to 3D printed clamps for better grip. A transverse prestretch was applied on all the specimens to avoid wrinkling during the shear deformation. 5 cycles of preconditioning were performed, where a prestretch of 1.3 was applied with the transverse actuators, and shear was applied simultaneously by moving the central ac-

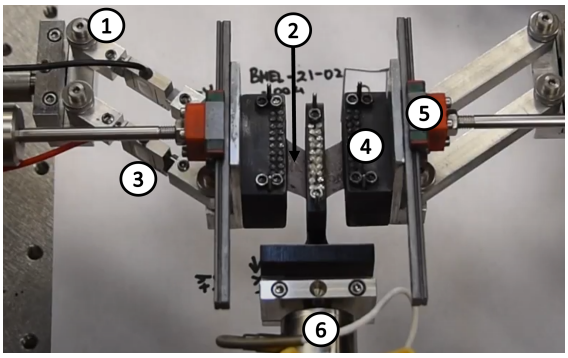

(a) Rat skin under shear

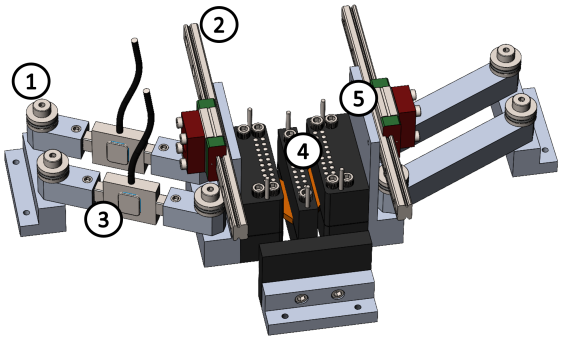

(b) 3D rendering of the jig

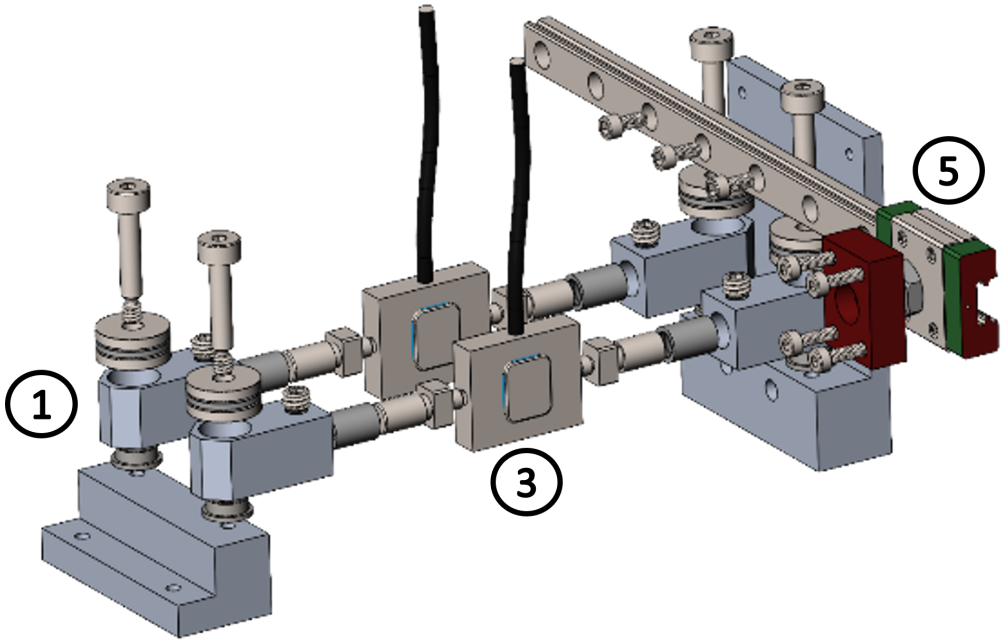

(c) Exploded 3D model of the 4 bar set-up

Figure 2.3: 1. Bearings for the pivots, 2. Sample, 3. Load cells mounted on the moment arms, 4. Clamps, 5. LVDT connected to the linear carriage mounted on the clamps, 6. Load cell for measuring f_x.

tuator 21.59mm. The loading and unloading ramp during the preconditioning were 85.0s each. Immediately following the preconditioning, first a transverse stretch of 1.3 was applied in 30.0s (1% engineering strain/s), followed by movement of the central actuator for 21.59mm in 85.0s (0.01 inches/s). 10 samples were tested in this fashion. To study the effect of the amount of prestretch, the test was repeated with 3 more samples each with prestretches of 1.25 and 1.35 (with the same rate of stretching at 1% engineering strain/s, or a duration of 25.0s and 35.0s

respectively), for a total of 16 samples. 10lb load cells (LSB210, Futek, CA, USA) were used in the central arm as well in both links. Overhead images for DIC analysis and load and grip displacement data were captured at 1Hz.

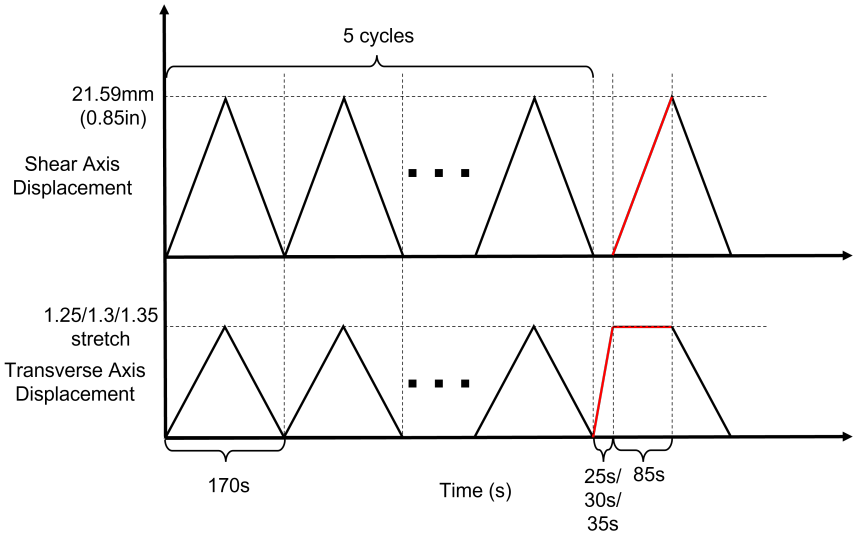

(a) Test protocol for silicone

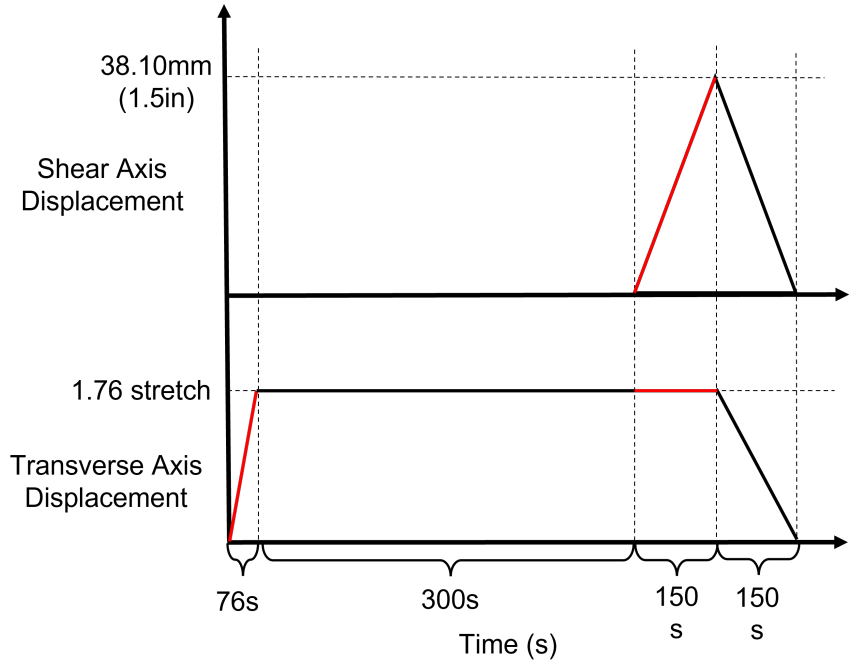

(b) Test protocol for rat skin

Figure 2.4: Red lines indicate part of data used for DIC and data analysis

2.3.1.2 Rat skin

Male Lister black hooded rats between 12 to 15 weeks old and weighing between 400g to 475g were euthanized with CO2, followed by secondary euthanasia by bilateral thoracotomy. Depilatory cream (Nair^{TM} Hair Remover) was applied using manufacturer instructions and the fur was removed from the dorsal section. The shape of the sample was drawn on the rat prior with a template laser cut from a thin sheet of PET. The dorsal skin was excised and any subcutaneous fat was removed. It was then stored in cotton gauze soaked in PBS solution and kept in ice prior to transport to testing location. A mallet and a rectangular leather punch (24.89mm by 18.85mm) were used to obtain 2 samples from the dorsal skin, one along the Cranial-Caudal and one along the Medial-Lateral directions. The skin was stretched so that the pattern drawn on the skin matched the punch prior to excision; this caused the sample size to shrink differentially along the CC and ML directions. The sample dimensions after excision were measured and then a speckle pattern was applied using black spray paint (same as with silicone from above). The sample was then clamped (with serrated needle clamps detailed in [22] and mounted to the 4-bar device in the biaxial testing system. Samples were clamped at a length of 3.94mm between the clamps, with the width varying between 15-18mm for an approximate aspect ratio of 4:1. Thickness of the samples were between 1.97 to 2.47mm. All sample dimension measurements were made optically.

A prestretch of 1.76 was applied in the transverse direction in 76.0s and held at that position for 300.0s. This was followed by application of shear by moving the central actuator 38.10mm in 150.0s (0.01 inches/s). This protocol was adopted instead of the preconditioning protocol applied on the silicone because the device was unstable under unloading conditions with the rat skin. It was also noticed that there was a significant amount of stress relaxation occurring following the prestretch, so a hold time was used to allow the loads to asymptote prior to the application of the shear deformation. 100lb load cells were used in the shear actuator (Model 31, Honeywell, NC, USA) and the 4-bar linkages (LSB210, Futek, CA, USA.

A total of 4 rats were used for the tests, and so shear tests were performed on 8 samples; 4

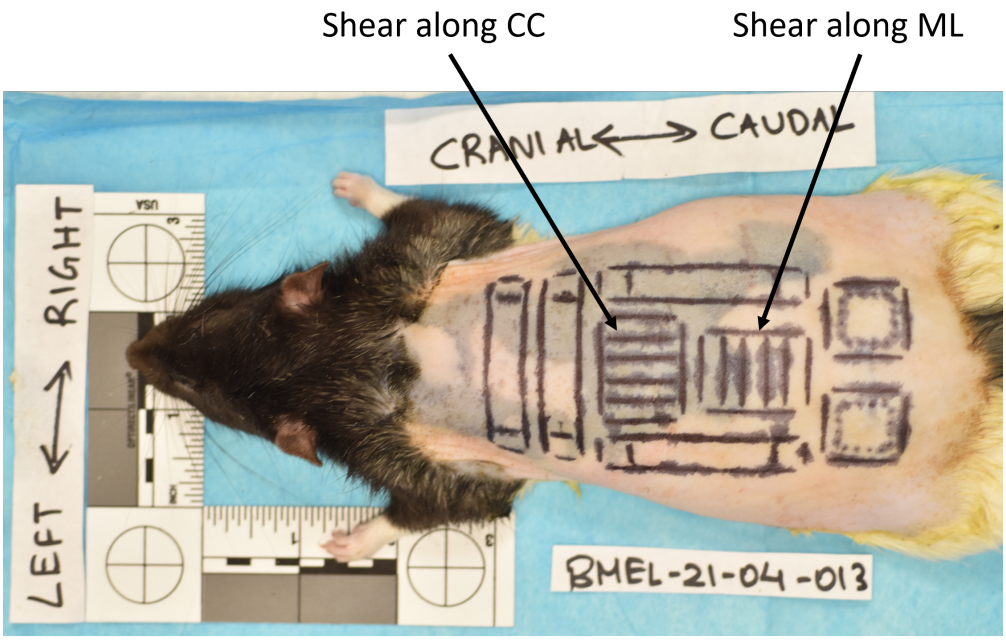

Figure 2.5: The shape of the leather punch, along with the lines for clamping the sample, drawn on the rat dorsal skin with a template

in the CC direction, 4 in the ML direction. All tests were completed within 6 hours of excision of skin from the rat. Samples were stored in PBS soaked cotton gauze and refrigerated at 4°C before warming to room temperature in a water bath for the test. All tests were conducted at room temperature without any environmental chambers. Overhead images for DIC analysis and load and grip displacement data were captured at 0.5Hz.

2.3.2 Data analysis

The Kirchoff stress $s = PF^T$ where P is the first Piola-Kirchoff stress. For all these tests, DIC analysis was performed and the Lagrangian displacement gradients were obtained. The deformation gradient was obtained by $F = \partial u/\partial X + I$ where $\partial u/\partial X$ is the displacement gradient and I is the identity tensor. For each frame, F is averaged over all the points on the surface. These average tensors are then used to transform P (which is tractions over inital areas, easily measured in experiments) to get s. For the simple shear tests, s is obtained directly from 2.1. The Green strain $E = 1/2(C - I)$, where $C = FF^T$. This was calculated at every point individually.

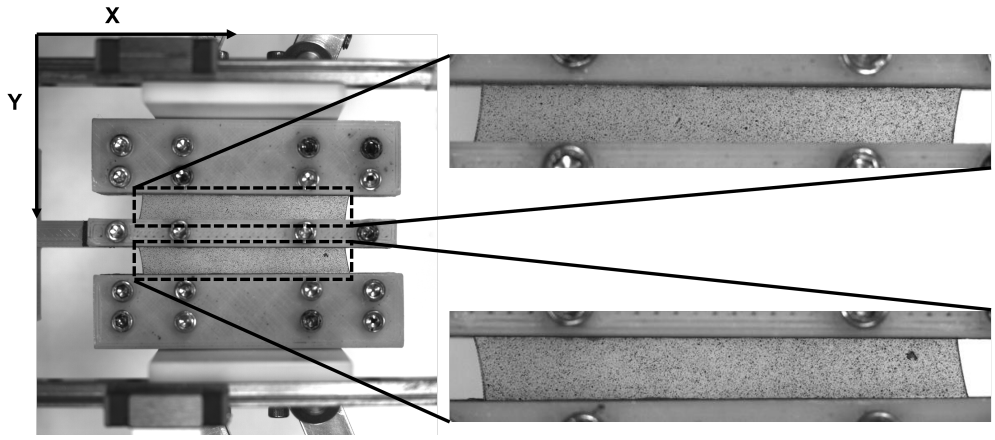

(a) Shear test on silicone

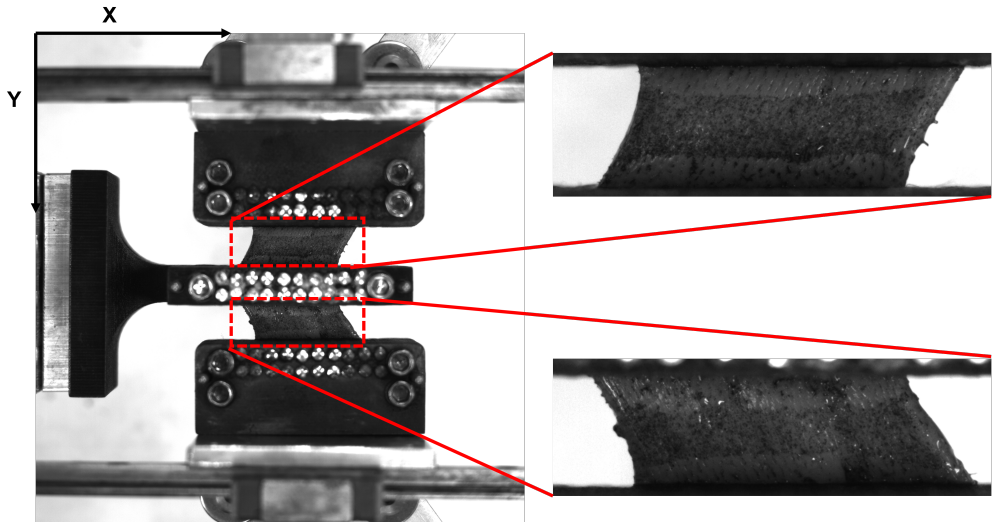

(b) Shear test on rat skin

Figure 2.6: Overhead CCD image captured during the double-lap shear experiments performed on silicone and rat skin

2.4 Results

Open source 2D DIC analysis software Ncorr [23] was used to perform DIC analysis. The C++ port offered on the website was modified to obtain the displacements and displacement gradients from Ncorr, and all further data analysis was performed with custom Python code.

2.4.1 Strain distribution and homogeneity

For the silicone samples, DIC analysis was performed on the final prestretch and shear deformation portions of the test. For the rat skin samples, images from the the first prestretch, and the the images of the shear deformation following the hold phase were used. The region of interest was the entire test region between the clamps. For each image or frame of the test, histograms were obtained to track the distributions of the Green strain components across the test area, and the mean, median and mode (defined as the histogram bin with the most number of data points) were calculated. The DIC results and the respective histogram distributions at the final frame of the test are shown in Figures 2.7 and 2.8. 'Window' refers to the difference between the 80th and 20th percentile strain values (the width of the shaded region in the histograms)

For each test, the three components of the Green strain are tracked throughout the experiment over the entire sample surface, and the mean, median, mode are tracked in Figures 2.9a and 2.9c. The boundaries of the shaded areas are the 20th and 80th percentiles of the strains, and so the shaded area represents the window inside which 60% of the data points lie in each frame. In Figures 2.9b and 2.9d, the data is restricted to only the shearing portion of the test and the strain components are all offset by their values at the beginning of the shear phase, allowing the tracking of these values during the shear phase only. Also, only the mean value and percentiles are shown in these figures for clarity, and those values are themselves averages of the values obtained in the top and bottom portions of the double lap shear test.

Figures 2.7, 2.8, and 2.9 provide a complete and comprehensive picture of the deformation of the material through the test period. A very high level of homogeneity was achieved for silicone, as evidenced by the very small 'window' values for E_{xy} (the shaded regions around the mean). A level of homogeneity was achieved for rat skin as well. In both cases, during the prestretch phase XX and YY components of the strain change, with Y being the stretching direction. During this period, the shear strain remains very close to 0. Following this, during the shear phase, the XX and YY components remain relatively stable while the shear value increases

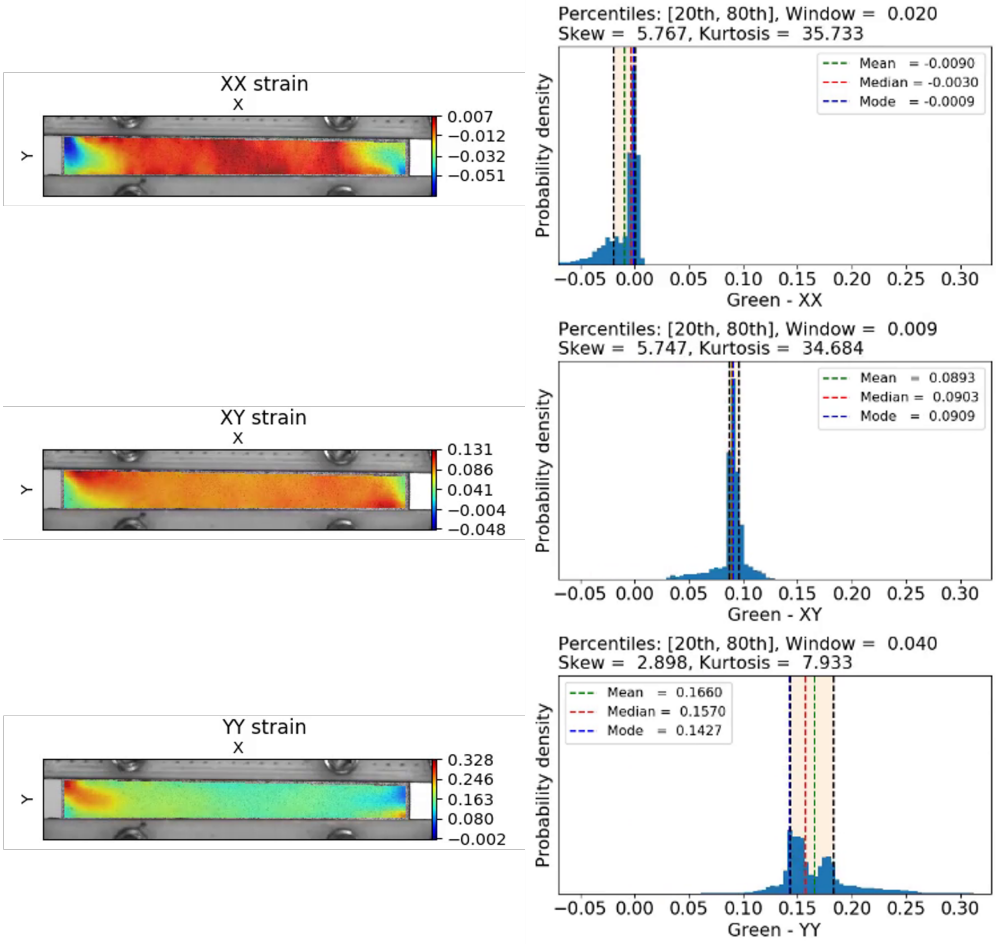

Figure 2.7: DIC analysis showing the the components of the Green strain (E_{xx}, E_{xy}, E_{yy}) throughout the test area in the final frame of the shear test on a silicone sample. The histograms of the distribution on these strains are shown on the right

linearly, demonstrating that the shear deformation is achieved in the absence of other modes of deformation. For rat skin, at larger strains the non-linearty of the strain measure becomes clear for the XX and YY components. Additionally, the 'window' is quite narrow for the shear component for both materials, while the other components seem more spread out. The smaller aspect ratio of the rat skin (4:1) sample could be the reason for the significant shrinking of the sample in the XX direction, compared to the silicone sample which had a much larger aspect ratio (10:1). The strain components are noisy due to the constant adjustments made by the biaxial system during the shearing phase to prevent stretching the material in the transverse (Y) direc-

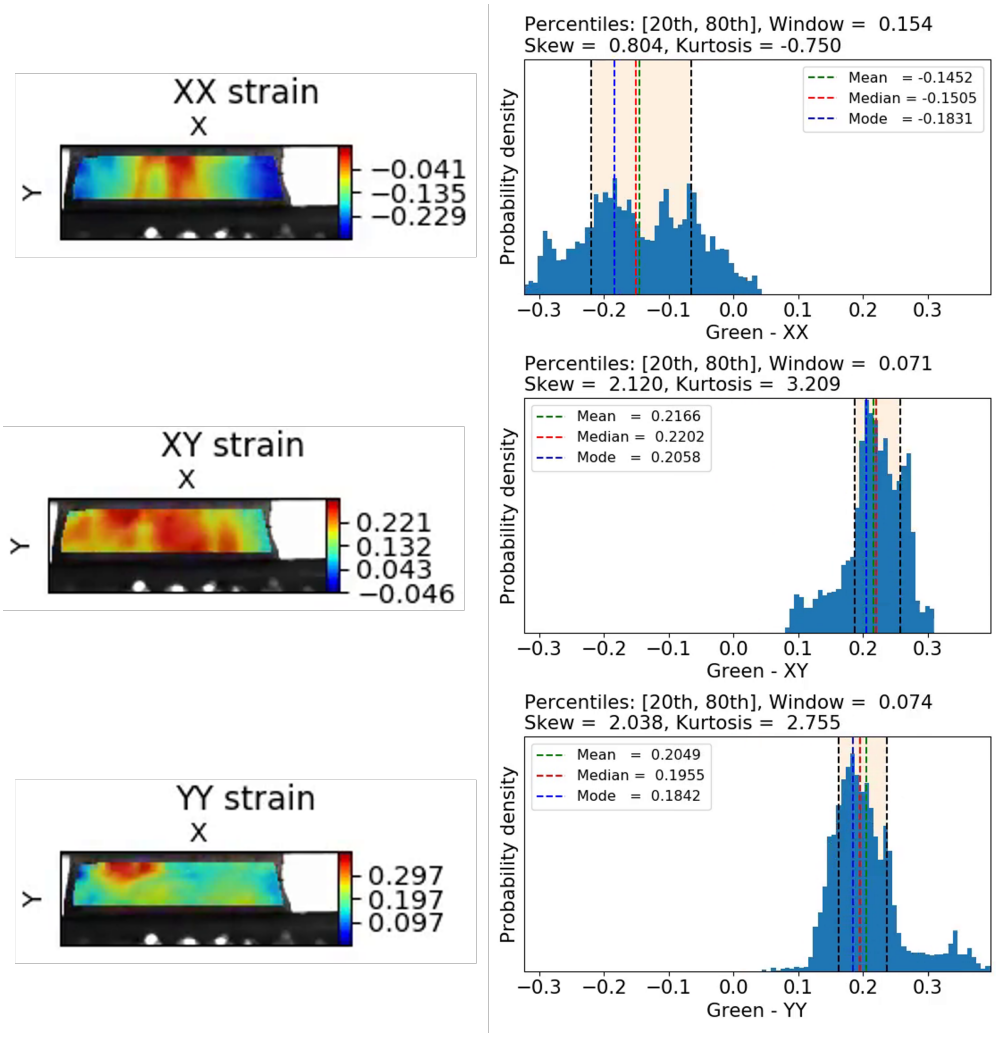

Figure 2.8: DIC analysis showing the the components of the Green strain (E_{xx}, E_{xy}, E_{yy}) throughout the test area in the final frame of the shear test on a rat skin sample. The histograms of the distribution on these strains are shown on the right.

tion. Despite this, the general trend of the development of these strains during the test period is consistent. Moving forward, the mean strain value for each frame (the solid lines in Figure 2.9) will be used for all data analysis.

The strains over time for all the samples tested RE shown in Figure 2.10. For both rat skin and silicone, offsetting the strain values at the beginning of the shear phase shows that the shear strain is produced relatively in isolation, with the other two components remaining close to 0. The development of the 3 strain components through the shear phase of the test is very

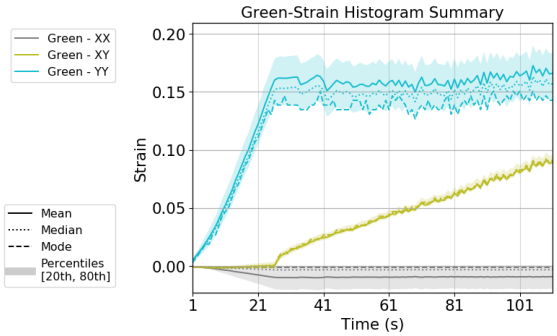

(a) Components of the Green strain throughout the test period for a silicone sample

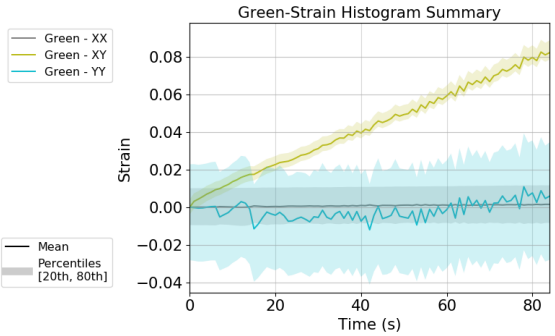

(b) Offset mean values of Green strain for the silicone sample

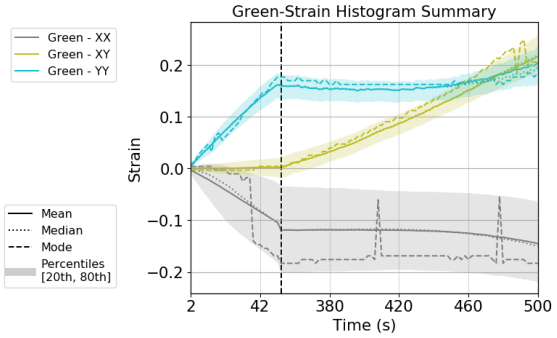

(c) Components of the Green strain throughout the test period for a rat skin sample. Vertical dashed line represents the hold phase of the test, which was omitted from the DIC analysis

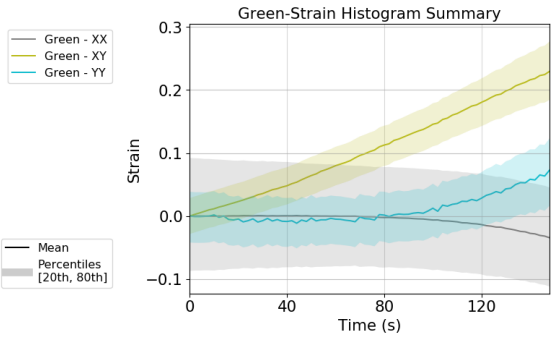

(d) Offset mean values of Green strain test for the rat skin sample

Figure 2.9: E_{xx}, E_{xy}, E_{yy} components of Green strain during the course of the shear test. The E_{yy} increases during the prestretch phase while E_{xx} shrinks, after which they remain relatively constant while E_{xy} increases during the shearing phase. In the figures on the right, the strain components are offset by their values at the end of the prestretch phase. The shaded areas represent the 20th to 80th percentiles of the strain distribution at each frame through the test.

consistent for both materials. For both materials, there is some inconsistency in the amount of prestretch applied, despite the same displacement of the actuator. But this does not seem to affect the development of shear over the test significantly.

For silicone, it can be seen that the higher prestretch tended to produce a slightly larger shear for the same applied displacement of the actuator. Additionally, for silicone the E_{yy} lines from Figure 2.10a suggest that a higher prestretch produced a larger strain in that direction. The dashed, dotted, and solid lines in Figures 2.10b and 2.10a represent the 3 different levels of

prestretch applied.

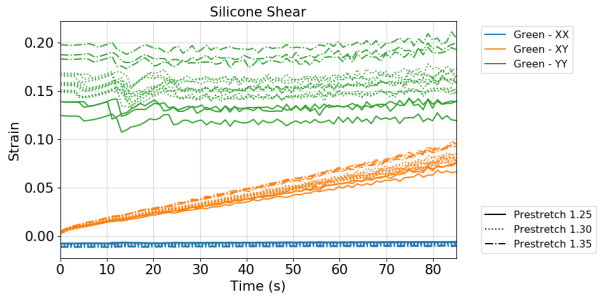

(a) Green strain components for silicone samples

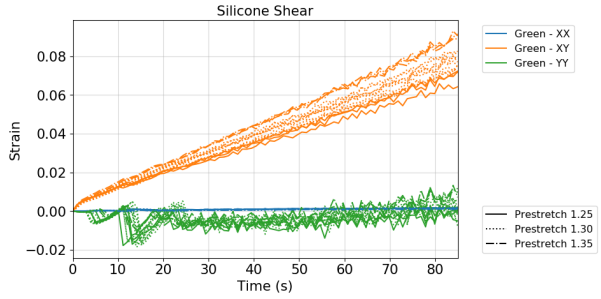

(b) Offset by their values at the beginning of the shear phase

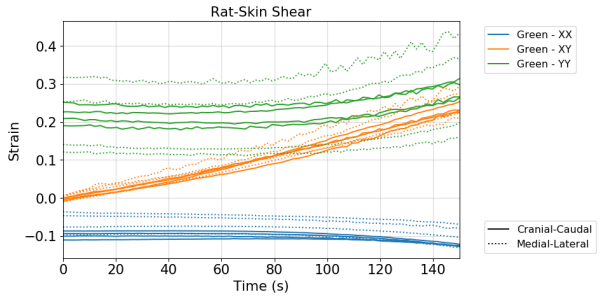

(c) Green strain components for rat skin samples

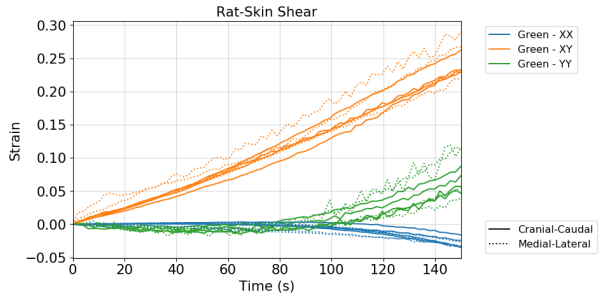

(d) Offset by their values at the beginning of the shear phase

Figure 2.10: E_{xx}, E_{xy}, E_{yy} components of Green strain during the course of the shear deformation. The XX and YY components of the strain increase during the prestretch phase, after which they remain relatively constant while the XY component increases during the shearing phase.On the right column, the strain components are offset by their values at the end of the prestretch phase, and the average strains and percentiles between the top and bottom half of the double lap shear test are shown.

In order to statistically assess the homogeneity of the strain over the test surface, a so-called 'Normalized Inhomogeneity' value is defined as

$$Uniformity\ of\ E_{comp} = \frac{Variation\ Range\ of\ E_{comp}}{max(\overline{E_{xy}})}, E_{comp} \in E_{xx}, E_{xy}, E_{yy} \tag{2.2}$$

where

$$Variation\ Range\ of\ E_{comp} = 80^{th} - 20^{th}\ percentile\ of\ E_{comp} \tag{2.3}$$

where $\overline{E_{xy}}$ is the mean shear strain over the entire test surface. This is essentially looking at how wide the shaded areas are in Figure 2.9, normalized by the the maximum shear value obtained in the test. The normalized inhomogeneity of the strain fields were calculated for the three components for all the tests, and the mean values and the standard deviations for the final frame in each test are shown in Table 2.1. Additionally, the mean and standard deviation of $max(\overline{E_x})$ and the Variation Ranges for each material (over all the tests) is shown for context.

Material	**max($\overline{E_{xy}}$)**	E_{comp}	**Variation Range**	**Noramlized Inhomogeneity**
Silicone (n = 16)	0.081 ± 0.008	E_{xx}	0.019 ± 0.003	0.240 ± 0.016
		E_{xy}	0.010 ± 0.002	0.120 ± 0.021
		E_{yy}	0.057 ± 0.005	0.712 ± 0.074
Rat skin (n = 8)	0.242 ± 0.028	E_{xx}	0.166 ± 0.031	0.694 ± 0.156
		E_{xy}	0.101 ± 0.024	0.417 ± 0.055
		E_{yy}	0.145 ± 0.057	0.584 ± 0.163

Table 2.1: Normalized Inhomogeneity of the Green strain components in the simple shear test. All values are mean ± standard deviation.

For both materials, the shear strain appears to be quite uniformly distributed over the test surface.

2.4.2 Moments and stresses

Having looked at the strains produced by the jig and their consistency, the loads measured are now analysed. One of the main requirements of this novel shear jig was to capture the moment loads applied by the sample on the clamps during rectilinear simple shear. f_1, f_2 and $2f_x$ are obtained directly from the load cells (Figure 2.2). With θ being the angle between the X direction and the direction of f_1 and f_2, the horizontal components f_{y1} and f_{y1} are calculated as

follows

$$\begin{aligned} f_x &= f_{x1} + f_{x2} \\ &= f_1 cos\theta + f_2 cos\theta \\ cos\,\theta &= \frac{f_x}{f_{x1} + f_{x2}} \\ \theta &= cos^{-1}\left(\frac{f_x}{f_{x1} + f_{x2}}\right) \end{aligned} \tag{2.4}$$

and so then

$$\begin{aligned} f_{y1} &= f_1 sin\theta, \\ f_{y2} &= f_2 sin\theta \end{aligned} \tag{2.5}$$

f_{y1} and f_{y2} are thus obtained from the data, and they are plotted against E_{xy} in Figure 2.11

Both f_{y1} and f_{y2} start under some tension (due to the prestretch), and as the shear strain increases, f_{y1} decreases while f_{y2} increases, demonstrating clearly that a tension is applied on the far end of the sample and a compression at the near end, effectively applying a moment across the sample in order to maintain its configuration during the rectilinear shear test. For silicone, this pattern is very consistent and repeatable and produces quite linear curves. For rat skin, inspite of the sample transverse actuator displacement applied in each case, the transverse loads on the moment arms are not at all consistent. No clear difference is seen between the Cranial-Caudal and Medial-Lateral directions. The loads also progress quite non-linearly, with f_{y1} dipping below 0 N on all the tests.

To get the stress-strain curves for the shear deformation, f_x (Figure 2.2) is obtained from the load cell and used to calculate the shear stress. The XY component of the Kirchoff stress, or T_x (Eq 2.1) was calculated and plotted against E_{xy}.

The stress-strain curves for silicone appear highly linear and repeatable, with very tight confidence intervals. For rat skin, the stress strain curve is non-linear with the typical j-curve appearance. The two Medial-Lateral rat-skin samples with the low stiffness were excluded from

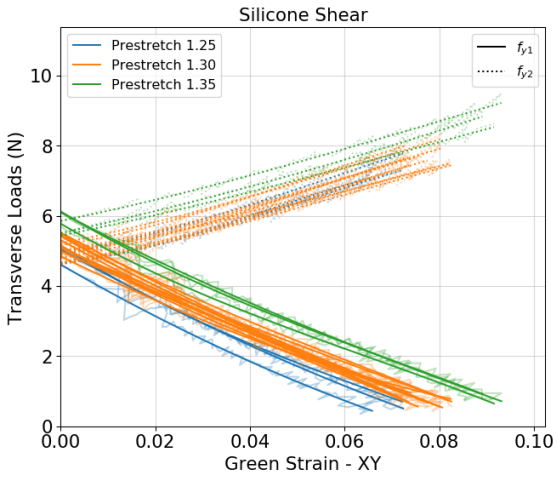

(a) Moment loads for silicone

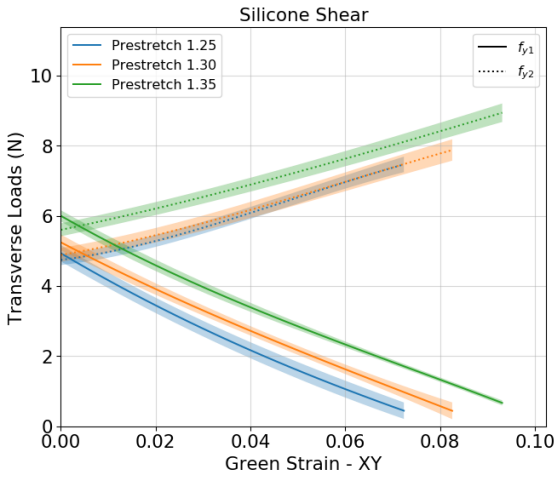

(b) Mean and standard deviation for silicone

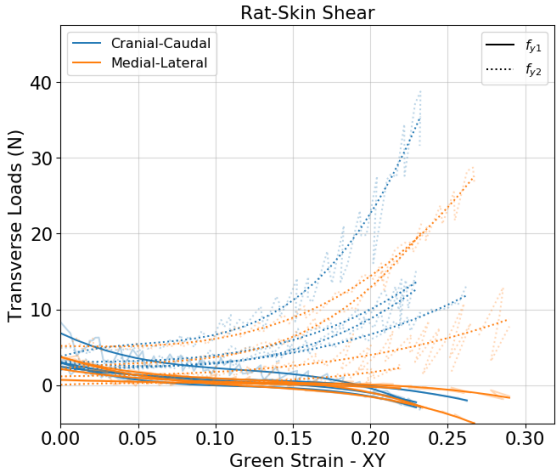

(c) Moment loads for rat skin. Translucent lines represent actual data, while the darker lines represent the filtered and smoothed curve

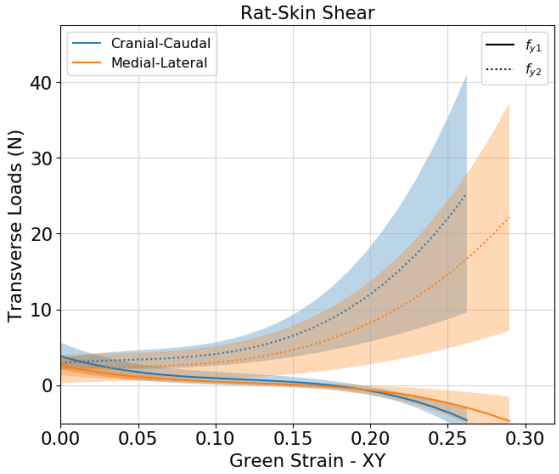

(d) Mean and standard deviation for rat skin

Figure 2.11: f_{y1} and f_{y2} loads plotted against E_{xy}. As the shear strain increases, f_{y1} reduces and f_{y2} increases, showing a net moment applied on the material.

the mean and confidence interval calculations.

2.5 Discussion

The novel shear apparatus shows promise for applying homogeneous simple shear deformations on soft membranes. The strain distribution is particularly homogeneous for silicone membranes, which can be seen in the DIC images and histograms of the end of the shear test (Figure 2.7). Tracking the evolution of the strain distribution across the entire test was also

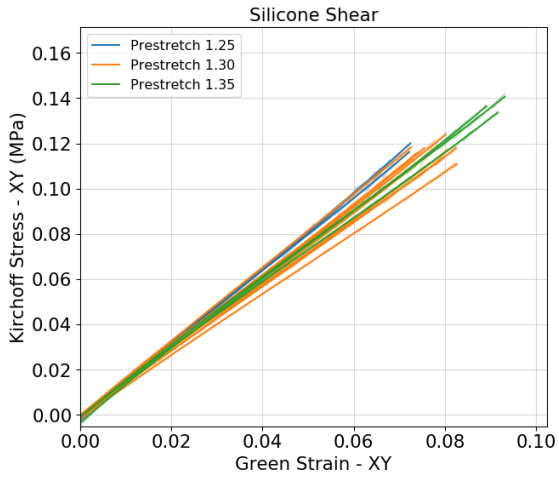

(a) Test data for all 16 silicone samples

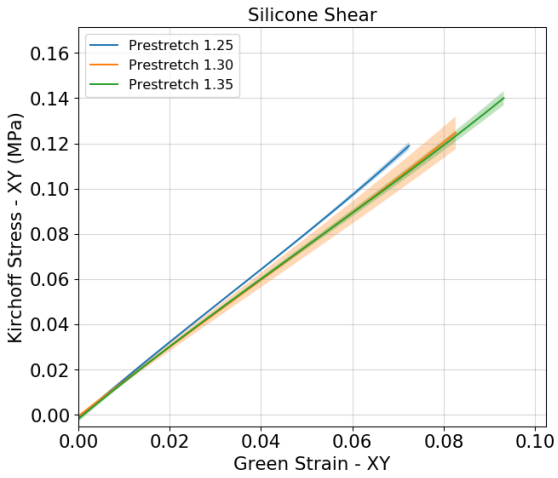

(b) Mean and standard deviation for the 3 different prestretches applied

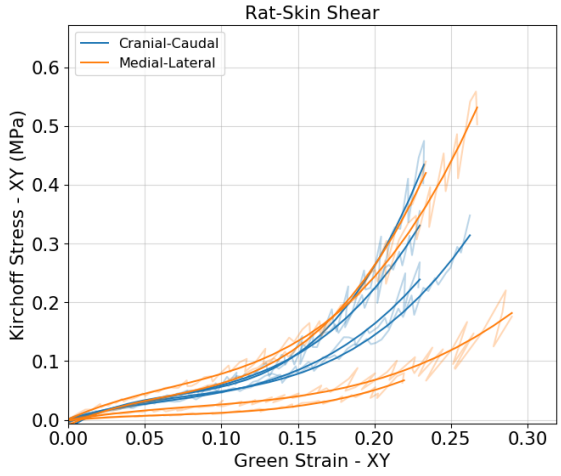

(c) Test data for all 8 rat skin samples. Translucent lines represent actual data, while the darker lines represent the filtered and smoothed curve

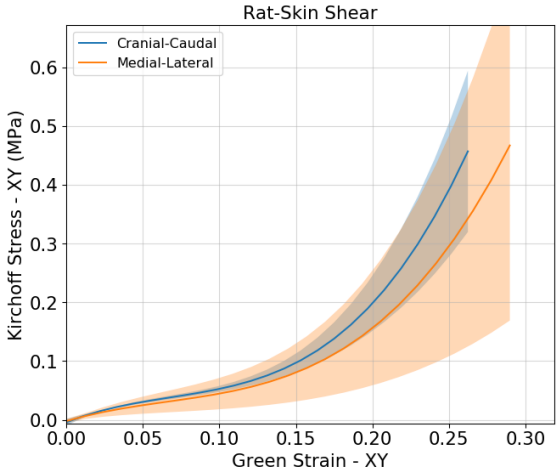

(d) Mean and standard deviation for the 2 different physiological directions

Figure 2.12: E_{xy} vs s_{xy} for the shear experiments

illuminating and provided a very clear picture of the deformation in the membrane (Figure 2.9.The novel apparatus is capable of applying shear very consistently and in isolation from other modes of deformation, as can be seen in Figure 2.10. The measure of homogeneity introduced, 'Uniformity' also gave a picture of the distribution of strain over the entire test surface.

For silicone, the amount of prestretch applied (in the range experimentally tested here) did

not seem to affect the stress-strain characteristics qualitatively. The variability in the rat skin data makes it hard to glean any such information about the effect of prestretch on the shear behaviour of rat skin.

The 4-bar mechanism allowed for the measurement of the moment applied by the material during rectilinear simple shear, which to the best of the author's knowledge has never been achieved. They show clearly a moment that increases with the increase in shear. This information has been missing from current modeling efforts and should be incorporated to better represent reality. The shear stress-strain curves are also obtained, but discussion of material parameters is reserved for later chapters.

The loads on the moment arms also provide a very interesting picture into the onset of wrinkling on the membrane. By definition, 2D membranes cannot support any compressive loads, and so must buckle or wrinkle in response. In practice, this can be applied to thin soft membranes that this apparatus is meant for. f_{y1} and f_{y2} can be used to calculate some parameter that can predict the onset of wrinkling, where perhaps a compressive load in either of the load cells indicates such an event. This can then be incorporated into experimental design to ensure that any data obtained does not include loads from wrinkling. The total transverse traction T_2 can also be tracked here, while in a typical set-up, a load cell placed in that axis will experience off-axis loads that might damage it and corrupt the data. A load cell capable of measuring loads as well as moments may be used, but the data obtained will be not as granular, and the additional expense of these load cells may be prohibitve.

The object of using silicone was to investigate the experimental error introduced by the apparatus. Assuming that the different samples of silicone are all essentially the same material, the differences in the measured values between different tests can be construed as a representation of experimental error. All the tests performed on silicone show that this error is quite small across a variety of different measures, and provides support to the statement that this apparatus is capable of performing consistent, repeatable, rectilinear quasi static simple shear on soft membranes.

The deformation gradient F was assumed to be of the form (with the state of the material after prestretch, just prior to the shearing motion, considered the reference configuration)

$$F = \begin{bmatrix} 1 & \gamma \\ 0 & 1 \end{bmatrix} \tag{2.6}$$

where γ is the applied shear, in order for the Kirchoff stress to be filled as described in Eq 2.1. This assumption is checked by looking at the deformation gradient from the DIC analysis. The components of the deformation gradient are calculated for every point of the surface, and then average. Once this is done, the average F from all the tests is averaged again, and present as $F_{ij} \pm$ standard deviation, where F_{ij} are the components of F.

$$F_{silicone} = \begin{bmatrix} 1.0013 \pm 0.0002 & 0.1656 \pm 0.0160 \\ -0.0073 \pm 0.0007 & 0.9878 \pm 0.0025 \end{bmatrix}$$

$$F_{ratskin} = \begin{bmatrix} 0.9650 \pm 0.0080 & 0.5695 \pm 0.0160 \\ -0.0073 \pm 0.0080 & 0.9201 \pm 0.0080 \end{bmatrix}$$

2.5.1 Limitations and future work

The silicone material underwent 5 cycles of preconditioning, where the material was simultaneously stretched and sheared, before the final prestretch followed by shear.

The load data is quite jagged and noisy, because as the X actuator moved, the 4-bars swing and try to stretch the sample in Y, and this motion is adjusted for the movement of the Y actuators. This constant readjustment leads to this noisy data. This is also the reason for the quite slow rate of 0.01in (2.54mm) per second displacement rate. At higher rates, the movement is too quick and unconstrained for the system to effectively control the stretch. Therefore, high rates of shear cannot be performed. The high amount of prestretch applied was due to this issue as well. At smaller loads, the sample wrinkled quickly and the shear deformations were not at all

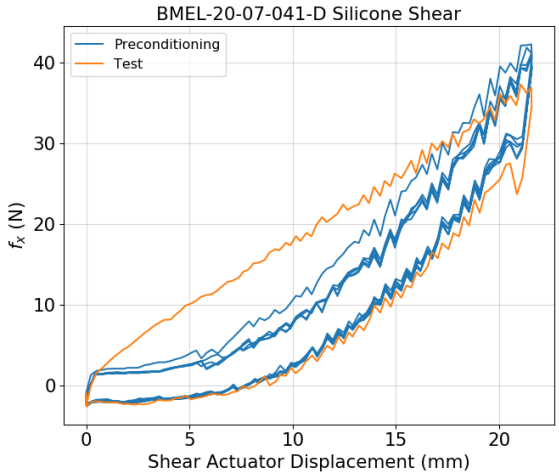

(a) X load and actuator displacement for silicone, during preconditioning and test

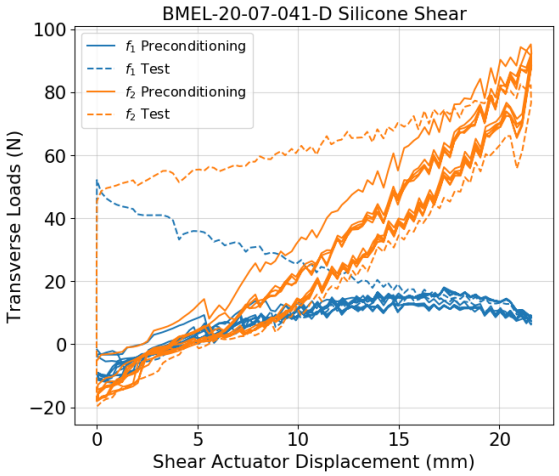

(b) Loads on the 4-bar arms during the preconditioning and test portions for silicone

Figure 2.13: f_x, f_1, and f_2 loads during the test on a silicone sample

repeatable.

Despite this issue, the preconditioning curves are quite repeatable and consistent, both within a sample and across all the samples, for silicone. For rat skin however, perhaps because of a very low shear modulus, cyclic movements could not be performed repeatably by the apparatus. The unloading ramp tended to buckle the membrane completely, and subsequent cycles no longer had a similar starting point. So preconditioning was not done for rat skin. Additonally, due to the highly viscoelastic nature of the material, it relaxed significantly upon applying the prestretch, and this convoluted the loads from the moment arms. This was why a hybrid approach of applying the prestretch, then holding until the loads stabilized before applying the shear was adopted (Figure 2.14). Despite these concessions, the data is still quite noisy and jagged for f_x, compared to silicone. All the tests on rat skin were conducted at room temperature without a water/saline bath. Submerging this device may introduce additional complications to it's use that have not be explored.

The effect of the prestretch applied to the material on the stress-strain characteristics has not been studied thoroughly. At first glance, it does not seem to affect the bahviour of silicone, while the rat skin data is too varied to make any qualitative judgements. A systematic study and

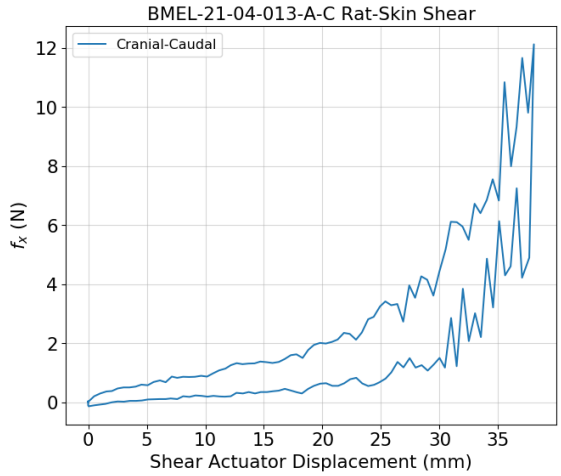

(a) X load and actuator displacement for rat skin

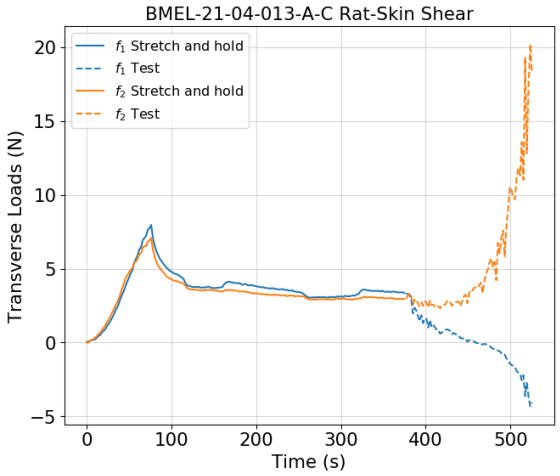

(b) Loads on the 4-bar arms for rat skin, plotted against time

Figure 2.14: f_x, f_1, and f_2 loads during the test on a rat skin sample. Figure 2.14b shows the relaxation of the loads on Y axis after prestretch prior to the application of shear

subsequent statistical analysis is required to investigate this.

Finally, the device is quite complex and requires a high level of fabrication accuracy and experimental expertise to utilise properly. This can be reduced by using strain gauges mounted directly on the 4-bar linkages instead of using a separate load cell, which will restrict the non-axis movements on the apparatus as well as simplifying assembly and use, and provide better load data.

2.6 Conclusion

A novel apparatus to perform rectilinear simple shear deformation on soft membranes was developed. simple shear deformation was applied on 16 silicone membranes and 8 rat skin samples, the boundary loads were measured as defined in [19], and statistical analysis was performed on the uniformity of deformation. It was shown that this apparatus is capable of applying simple shear deformation consistently and repeatably on an engineering material, silicone. Several methods of analysing the homogeneity of strain field developed were discussed and the capability of this apparatus in producing a uniform strain field distribution has been quantified.

This set of analysis performed with data obtained from DIC analysis, which has been gaining a significant popularity in recent years, to quantify the homogeneity of strain fields are potentially useful in other contexts of mechanical testing as well. The transverse loads and moments applied at the boundary in simple shear experiments have been measured, to the best of the author's knowledge, for the first time. This data might provide significant improvement to existing finite element simulation methods by providing crucial pieces of missing boundary conditions, as well have implications for the study of wrinkling and it's onset during the shearing of soft membranes.

3.1 Background

Freed et al[16] have proposed a framework for planar analysis of biological tissues, where the material response is described using conjugate stress/strain pairs for three distinct modes of deformation: dilation, squeeze, and shear (Figure 3.1). These modes are a natural consequence of decomposing the deformation gradient using the QR decomposition proposed by Srinivasa [15] (See A.2).

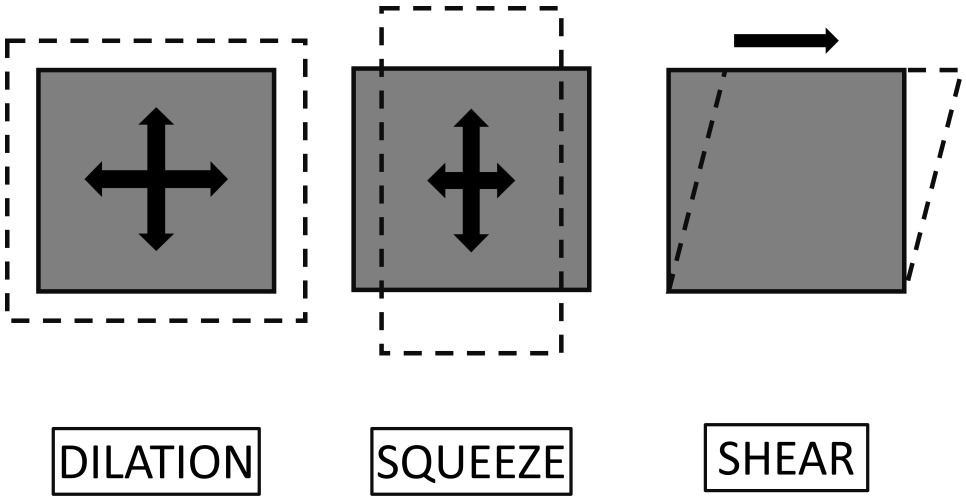

Figure 3.1: The 3 modes of deformation for a planar material. Dilation is represented by a uniform area change, squeeze is represented by shape change from a square to a rectangle without an area change, and shear is represented as show here, again without a change in area

By performing the decomposition in this way, the stress power can be additively decomposed using the three conjugate stress/strain pairs. (Appendices A and B have more details on using this framework in nonlinear elasticity).

$$dW = \pi d\delta + \sigma d\varepsilon + \tau d\gamma \tag{3.1}$$

where the conjugate stress/strain pairs $\{\pi,\delta\}$, $\{\sigma,\varepsilon\}$, and $\{\tau,\gamma\}$ describe uniform dilation, squeeze, and shear respectively. The values for these scalars are obtained from the Kirchoff stress tensor using the encoding algorithm put forth in [16]. In order to use this framework, ideally three separate experiments would be performed, where the material is deformed in each of the modes (dilation, squeeze, and shear) while the other two modes are fixed. In this chapter, tests deforming silicone membranes in these three modes will be described, and the data from DIC analysis performed on these membranes will be analysed. Dilation data will be obtained from equibiaxial tests, squeeze data from uniaxial tests, and shear data from simple shear tests.

In theory it is possible to apply dilation and shear deformations in isolation to study material response to these modes. However, squeeze is not so simple. Squeeze in 2D can be thought of as the changing of a square to a rectangle without a change in area. When materials are stretched in one direction, they shrink in the other two directions (identically if it is a isotropic material) due to Poisson's effect (barring atypical auxetic materials with a negative Poisson's ratio). In order to produce squeeze in 2D, stretches of λ and $1/\lambda$ have to be achieved. But in reality, a 3D material contracts in 2 directions when stretched in one. A uniaxial test on an isotropic material, with stretch λ in the test direction, produces contractions of $1/\sqrt{\lambda}$ in the other two directions, which is larger than $1/\lambda$. Therefore to deform in squeeze only, a compressive load has to be applied in the transverse direction to compliment the contraction due to the Poisson's effect. This cannot be achieved since, by definition, thin 2D membranes cannot support compression and so will buckle. Uniaxial extension is thus a combination of dilation and squeeze. The squeeze response can be extracted from this test, with the assumption that the dilation response is decoupled from the squeeze response.

3.2 Methods

3.2.1 Test protocols

Clear silicone sheets were obtained from McMaster-Carr Supply Company, Elmhurst, IL, USA (Catalog # 86915K12), with nominal thickness measured with vernier calipers to be 0.72mm

(same as the silicone mentioned in Chapter 2). Uniaxial and equibiaxial tension tests were performed, along with simple shear. The samples were laser cut from the sheet using a CO_2 laser cutter. A speckle pattern was produced on all the samples using black spray paint (Universal Premium Spray Paint, Flat Black, Rust-Oleum, IL, USA) for DIC analysis. All tests were performed on the system previously described in [21] under displacement control.

3.2.1.1 Equibiaxial tension

Equibiaxial tension tests were performed with sutures. In order to allow for in-plane shear and prevent unwanted constraints on the material, the suture set up was based on the work of Sacks et al [24]. 3D printed fixtures with roller bearings were used to complete the set-up shown in Figure 3.2. Suture lines pass around poles and pierce the sample in 2 adjacent locations. 2 of these per side for 4 sides involved 16 sutures and 8 suture lines. The suture lines pass around poles mounted on a platform pivoting on a bearing, and the whole thing is connected to the linear actuator. This setup allows the 4 points per side to equalize the load between the 4 suture lines. The sutures used in this case were office staple pins, and suture lines were braided fishing lines. A 3D printed platform with holes in the suture locations was used to accurately place the sutures at the same location each time. This set-up was developed and fabricated by one of the author's colleagues.

For the test, 10 samples were tested in equibiaxial tension. Samples were of size 20.32mm x 20.32mm. 4 sutures were placed on each side 3.05mm apart, with the enclosed square having sides of 15.24mm x 15.24mm. After the speckle pattern was placed, the sample was mounted on the system and loaded to 0.22N on each axis to make the suture lines taut. 9 cycles of preconditioning were performed, with ramp load and unload to an amplitude of stretch of 1.49 (on a gauge length of 15.24mm), with each ramp occuring in 49.0s (or a rate of 1% engineering strain per second). Immediately following the 9 cycles, the same ramp load was performed again and this loading ramp was used for all DIC and data analysis. Data and images were recorded at 1Hz.

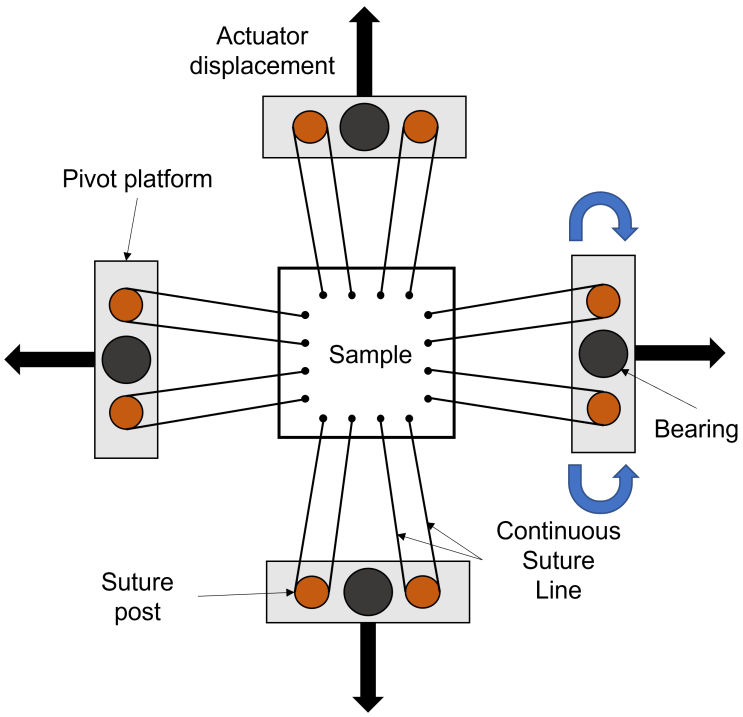

Figure 3.2: Suture set up for equibiaxial testing

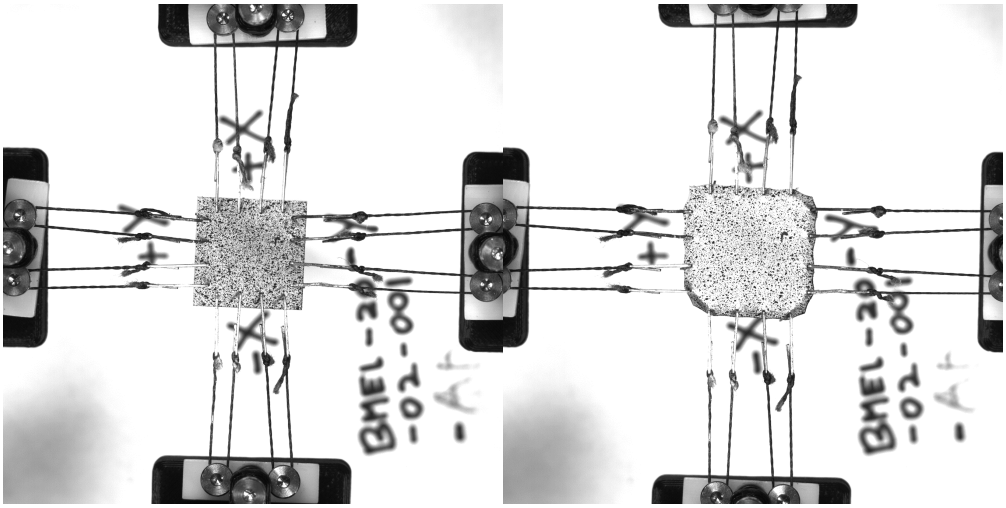

Figure 3.3: Initial and final images of the final loading ramp for equibiaxial test of silicone

3.2.1.2 *Uniaxial tension*

Uniaxial tension tests were performed on 10 silicone samples. 3D printed clamps (previously described in [22]) were used along with a 3D printed alignment jig to clamp the uniaxial silicone specimens. Samples were of length 69.85mm and 12.7mm in width. They were clamped at a gauge length of 50.8mm, spray painted with the speckle pattern and mounted on the system. 9 cycles of preconditioning were performed, with ramp load and unload to an amplitude of stretch of 1.74(on a gauge length of 50.8mm), with each ramp occuring in 74.0s (or a rate of 1% engineering strain per second). Immediately following the 9 cycles, the same ramp load was performed again and this loading ramp was used for all DIC and data analysis. Data and images were recorded at 0.5Hz.

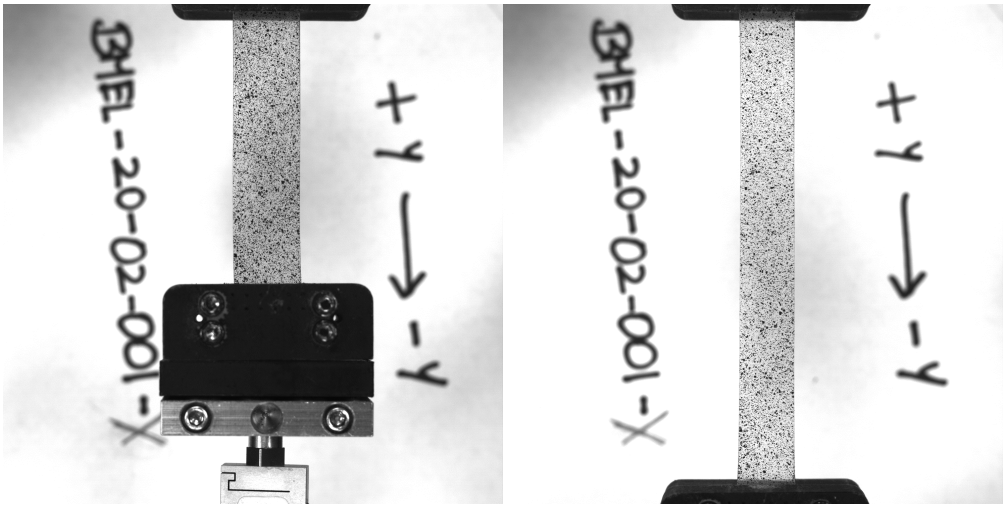

Figure 3.4: Initial and final images of the final loading ramp for uniaxial test of silicone

3.2.1.3 *Simple shear*

The methods used for testing of silicone in shear are already described in 2.3.1.1 but is copied here for convenience. Samples of size 44.45mm by 41.91mm were laser cut from the sheet. A speckle pattern was produced on the samples using black spray paint (Universal Pre-

mium Spray Paint, Flat Black, Rust-Oleum, IL, USA). They were then clamped and mounted on the system, with the samples being nominally 44.45mm wide and 4.445mm long between the central and transverse clamps (with an aspect ratio of 10:1). Sandpaper was glued to 3D printed clamps for better grip. A transverse prestretch was applied on all the specimens to avoid wrinkling during the shear deformation.

5 cycles of preconditioning were performed, where a prestretch of 1.3 was applied with the transverse actuators, and shear was applied simultaneously by moving the central actuator 21.59mm. The loading and unloading ramp during the preconditioning were 85.0s each. Immediately following the preconditioning, first a transverse stretch of 1.3 was applied in 30.0s (1% engineering strain/s), followed by movement of the central actuator for 21.59mm in 85.0s (0.01 inches/s). 10 samples were tested in this fashion. To study the effect of the amount of prestretch, the test was repeated with 3 more samples each with prestretches of 1.25 and 1.35 (with the same rate of stretching at 1% engineering strain/s, or a duration of 25.0s and 35.0s respectively), for a total of 16 samples. 10lb load cells (LSB210, Futek, CA, USA) were used in the central arm as well in both links. Overhead images for DIC analysis and load and grip displacement data were captured at 1Hz.

3.2.2 Data analysis

DIC was performed on the entire test region for all the tests. The encoding algorithm from [16] is used to calculate the conjugate strain values for the three modes dilation, squeeze, and shear, over the entire test area for all the tests. As detailed in Chapter 2, histograms were plotted depicting the distribution of the strain field data points in each frame. Using this, the mean, median, mode, and 20th and 80th percentile of the data points were tracked over the entire test period to get a sense of the strain field and the homogeneity. Consistency of the applied strain was tracked for all the samples, and the normalized inhomogeneity of the strain distribution was quantified similar to Eq 2.2. Here, instead of Green strain, the conjugate strain values were

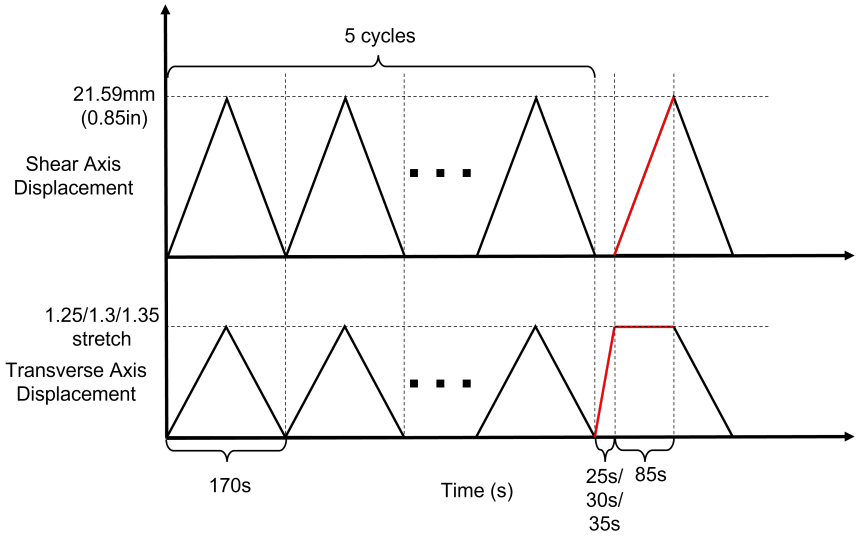

Figure 3.5: Test protocol for simple shear test on silicone. Red lines indicate part of data used for DIC and data analysis

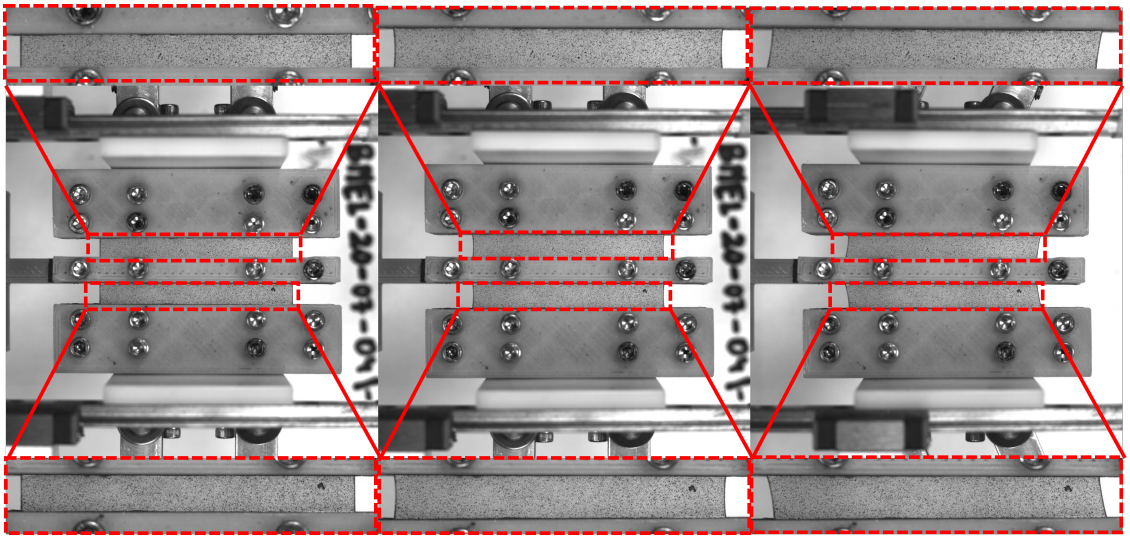

Figure 3.6: Initial (left), after prestretch (middle) and final (right) images of the final test ramp for shear test of silicone

used.

$$Uniformity\,of\,strain = \frac{Variation\,Range\,of\,strain}{max(\overline{'Test-type'\,strain})}, strain \in dilation,\, squeeze,\, shear \tag{3.2}$$

where

$$Variation\ Range\ of\ strain = 80^{th} - 20^{th}\ percentile\ of\ strain \tag{3.3}$$

Finally, the conjugate stress-strain pairs were plotted for each test. For all tests, in the final ramp, the reference image and data point was chosen based on the time at which the loads crossed a small, arbitrary critical threshold. This was done to remove any images with the material under slack that will convolute the DIC analysis.

The encoding algorithm from [16] is used to calculate the conjugates stresses and strains from the DIC analysis.

The conjugate stresses are calculated as

$$\begin{aligned} \pi &:= \tilde{S_{11}} + \tilde{S_{22}}, \\ \sigma &:= \tilde{S_{11}} - \tilde{S_{22}}, \\ \tau &:= \frac{a}{b}\tilde{S_{12}}, \end{aligned} \tag{3.4}$$

and the conjugate strains are

$$\begin{aligned} \delta &:= ln\sqrt{ab}, \\ \varepsilon &:= ln\sqrt{a/b}, \\ \gamma & \end{aligned} \tag{3.5}$$

$\tilde{S}$ or material stress, is defined as $\tilde{S} := Q^T sQ$, where Q is the rotation matrix obtained from a QR decomposition of the deformation gradient F, and s is the Kirchoff stress. $s = PF^T$ where P is the first Piola-Kirchoff stress.

For all these tests, DIC analysis is performed and the Lagrangian displacement gradients are obtained. The deformation gradient is obtained by $F = \partial u/\partial X + I$ where $\partial u/\partial X$ is the displacement gradient and I is the identity tensor. This is then used to calculate $\mathscr{U}$ and Q as described in the Appendix section of [16]. For each frame, F and Q are averaged over all the points on the surface. These average tensors are then used to transform P (which is tractions over inital ar-

eas, easily measured in experiments) and s as described earlier to get the conjugate stress strain pairs for the uniaxial and biaxial tests. For the simple shear tests, s is obtained directly from 2.1.

The 95% confidence interval calculations were made by resampling the curves with cubic-spline smoothing, and then the interval was calculated using a t-distribution

3.3 Results

3.3.1 Equibiaxial tests (Dilation)

Figure 3.7 shows the histogram and strain distribution at the end of the equibiaxial test on a silicone sample. The distribution is very tightly packed around the mean value for all three modes, showing a very uniform distribution of strain. The shaded region in the histogram represents 60% of the data points over the entire surface, or the 'window'. It can be seen that the homogeneous region of strain extends almost all the way up to the sutures. Additionally, in this equibiaxial test, both squeeze and shear strains remain close to 0 while only the dilation strain is active, demonstrating that this test is appropriate for studying the response of materials in dilation alone.

Figure 3.8a shows the the mean, median, mode, values of the 3 modes of deformation during the course of an equibiaxial test. The shaded regions represent the 20th to 80th percentile windows. The distribution is quite tight over the entire course of the test for all three modes, especially dilation, the mode of consideration for this test. The shear strain distribution seems to spread out at larger strains, but is still centered around 0 showing that the material is not being sheared in any particular direction. This could be from the regions near the sutures (which are also part of the DIC analysis) as the suture hole deforms at larger strains. The squeeze strains also remain centered around 0 for the entire duration of the test, with a much tighter distribution.

Figure 3.8b shows the two stretches a and b, obtained from the Laplace stretch $\mathscr{U}$. The distribution is quite tight and the stretches in the two directions are very close to each other, demonstrating that equibiaxial deformation is achieved.

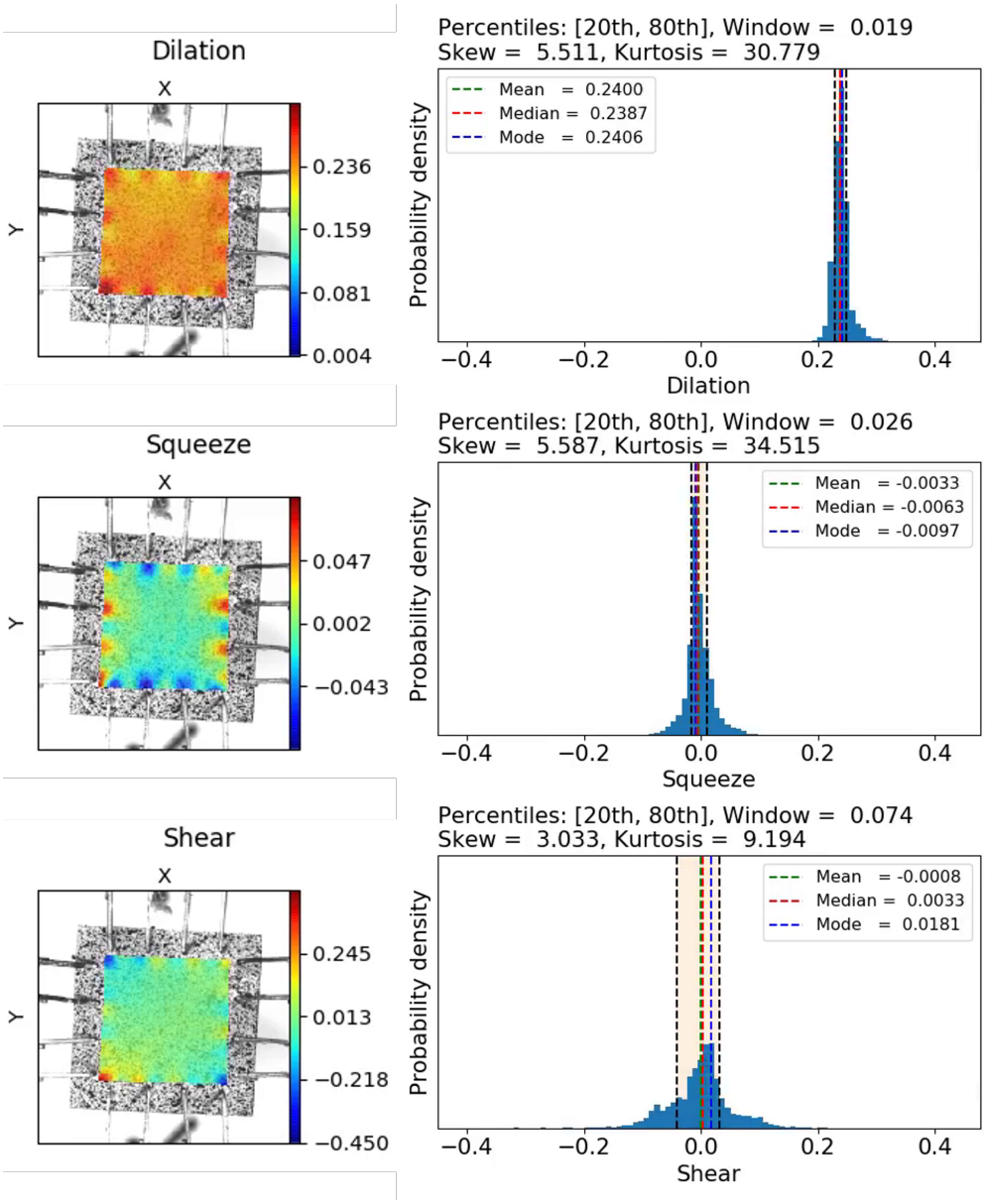

Figure 3.7: DIC analysis showing the distribution of the conjugate strain fields over the test region at the end of the equibiaxial test. Histograms show the shape of the distribution for these strains

Figure 3.9 shows the mean values (over the test surface) of the strain modes through the equibiaxial test for all 10 samples tested. The results are quite consistent and repeatable over all the samples, with both shear and squeeze strains centered around 0 while the dilation strain increased linearly over time.

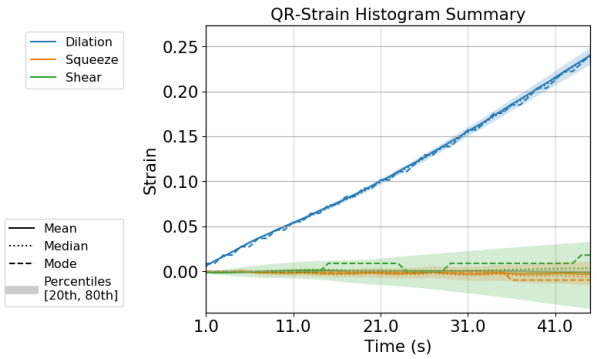

(a) The three modes of deformation over the test period for an equibiaxial test

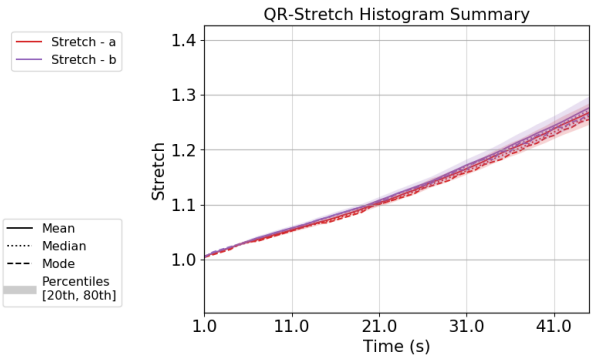

(b) The stretches in the two directions (a - X direction, b - Y direction) for an equibiaxial test

Figure 3.8: The summary of the strains and stretches obtained through the QR decomposition of the deformation gradient F for an equibiaxial test. Shaded regions represent the 20th to 80th percentile of the data points

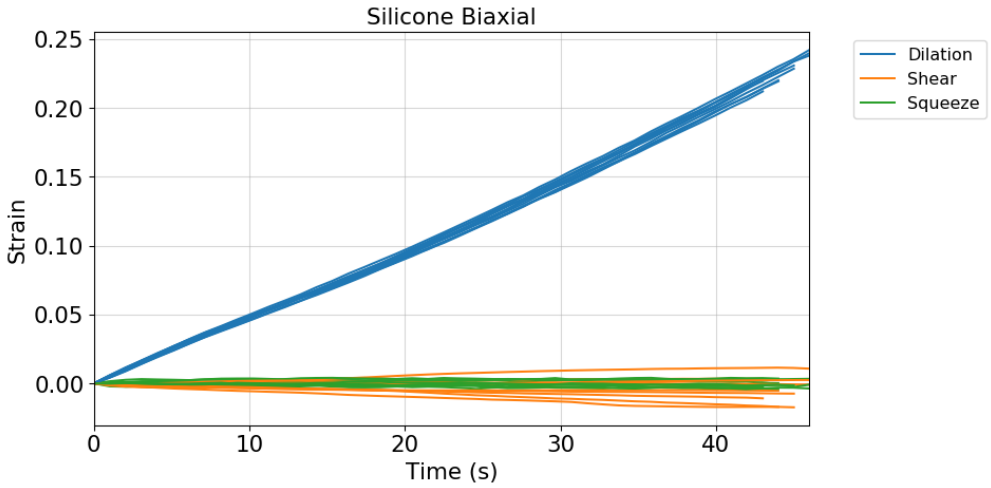

Figure 3.9: The three modes of deformation over the test period for the equibiaxial test for all the samples

Using the encoding algorithm described in the Methods section, the dilation stress was calculated as well (Figure 3.10a). A consistent curve shape is seen for all the samples, with the data spreading out slightly at higher strains. For completeness, the load vs stretch data for all the samples in the two directions is show in Figure 3.11a and standard deviations of the load stretch data is also shown (Figure 3.11b). Load values are obtained directly from the load cells,

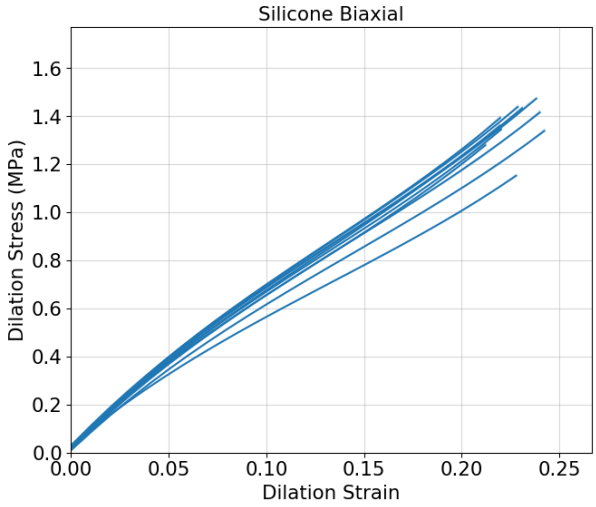

(a) The dilation conjugate stress-strain pair for all the 10 equibiaxial tests

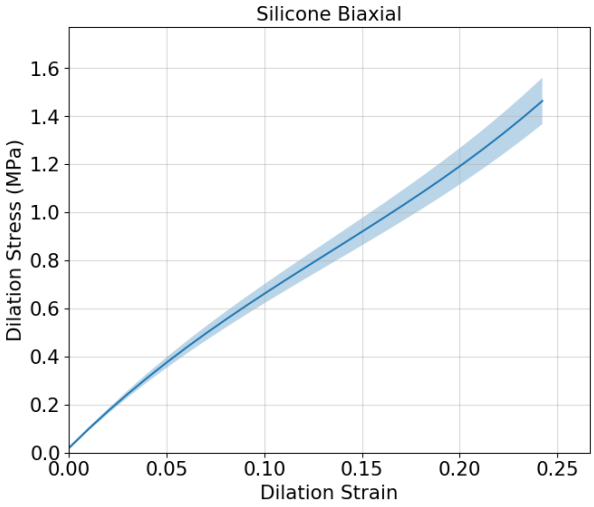

(b) Mean and standard deviation for the dilation curves for the equibiaxial tests

and the stretch values are obtained from DIC analysis (as shown in Figure 3.8b). They show that the material has consistent, isotropic behavior in the current test conditions.

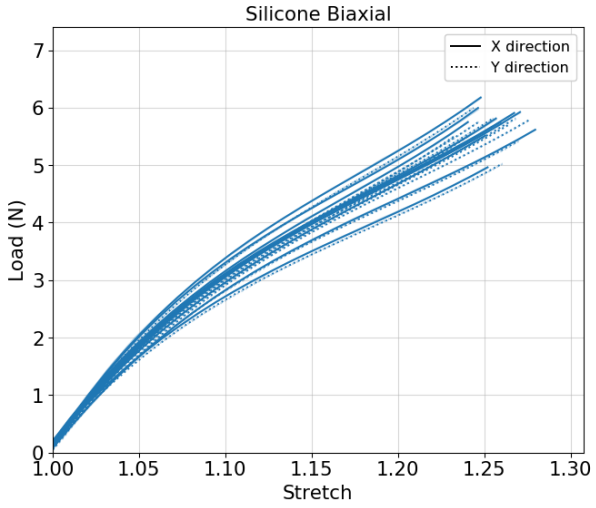

(a) Load vs Stretch for all the equibiaxial tests

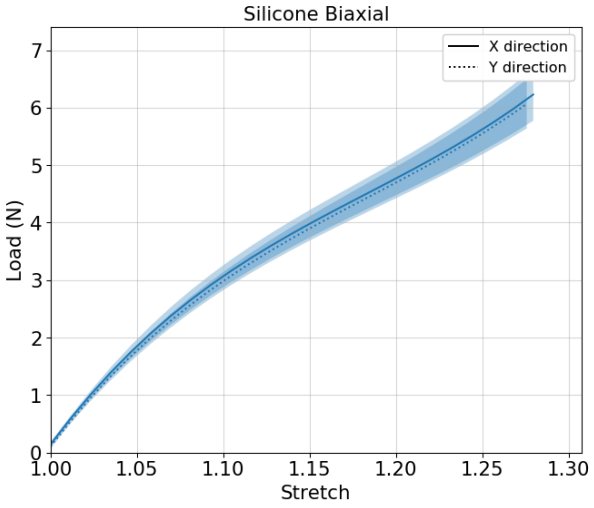

(b) Mean and standard deviation for the Load-Stretch curves in the X and Y directions for the equibiaxial tests

Figure 3.11: Load vs Stretch plots show consistent isotropic material response of silicone in equibiaxial deformation

3.3.2 Uniaxial tests (Squeeze)

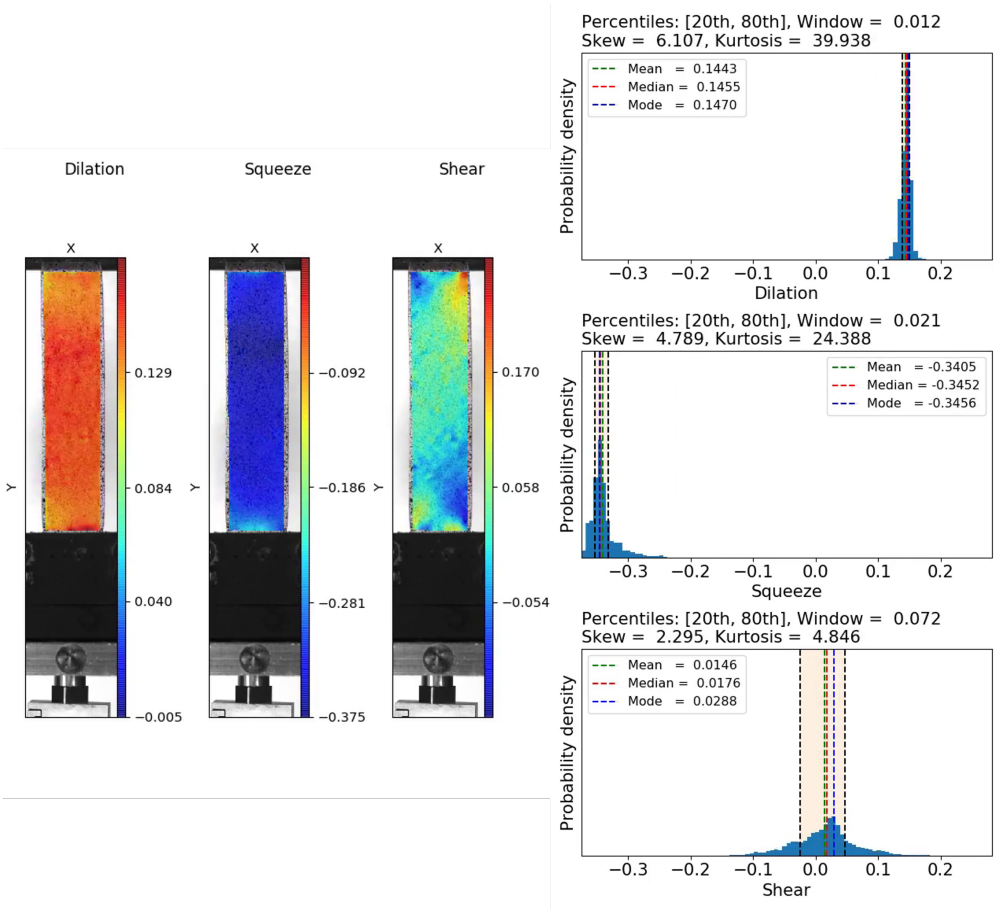

Figure 3.12: DIC analysis showing the distribution of the conjugate strain fields over the test region at the end of the uniaxial test. Histograms show the shape of the distribution for these strains

Figure 3.12 shows the histogram and strain distribution at the end of the uniaxial test on a silicone sample. The distribution is very tightly packed around the mean value for all dilation and squeeze, with a slight spread in the shear mode. It can be seen that the homogeneous region of strain extends almost all the way up to the clamps. The squeeze value is negative just because of the choice of axes, indicating that the stretch in the Y direction is larger than the contraction in the (transverse) X direction. The shear strain is centered around 0, while there is

a positive dilation and a larger negative squeeze, as was expected.

Figure 3.13a shows the the mean, median, mode, values of the 3 modes of deformation during the course of a uniaxial test. The distribution is quite tight over the entire course of the test for all three modes, especially dilation and squeeze, the modes of consideration for this test. The shear strain distribution seems to spread out at larger strains, but is still centered around 0 showing that the material is not being sheared in any particular direction.

Figure 3.13b shows the two stretches a and b, obtained from the Laplace stretch $\mathscr{U}$. The distribution is quite tight throughout the test. b is in the direction of the applied displacement (Y axis) while a is in the transverse direction, caused by Poisson's effect.

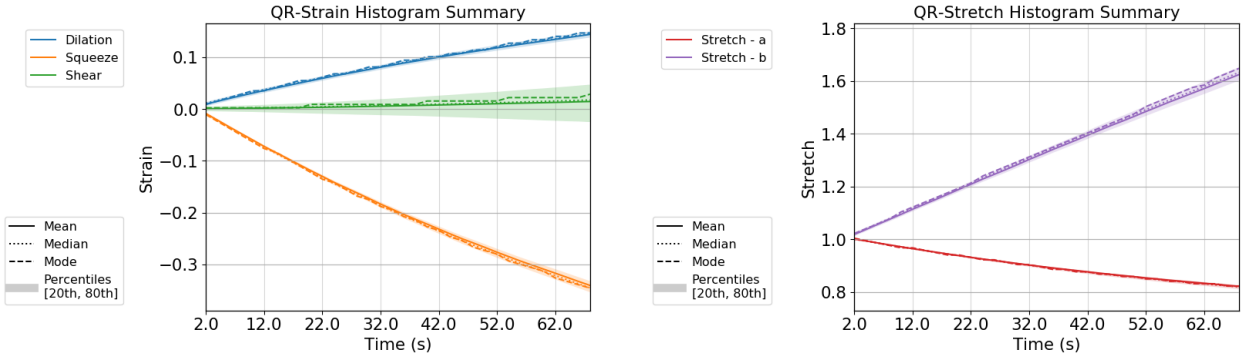

(a) The three modes of deformation over the test period for a uniaxial test

(b) The stretches in the two directions (a - X direction, b - Y direction) for a uniaxial test

Figure 3.13: The summary of the strains and stretches obtained through the QR decomposition of the deformation gradient F for a uniaxial test. Shaded regions represent the 20th to 80th percentile of the data points

Figure 3.14 shows the mean values (over the test surface) of the strain modes through the uniaxial test for all 10 samples tested. For better clarity, the squeeze strains have been multiplied by -1. Both squeeze and dilation have developed very consistently over the 10 samples tested in uniaxial tension, while there is some variation in the shear response. This is potentially from incorrect aligning of the material with the system axes during clamping, causing the material to be clamped at a slight angle, causing the shear. The results are quite consistent

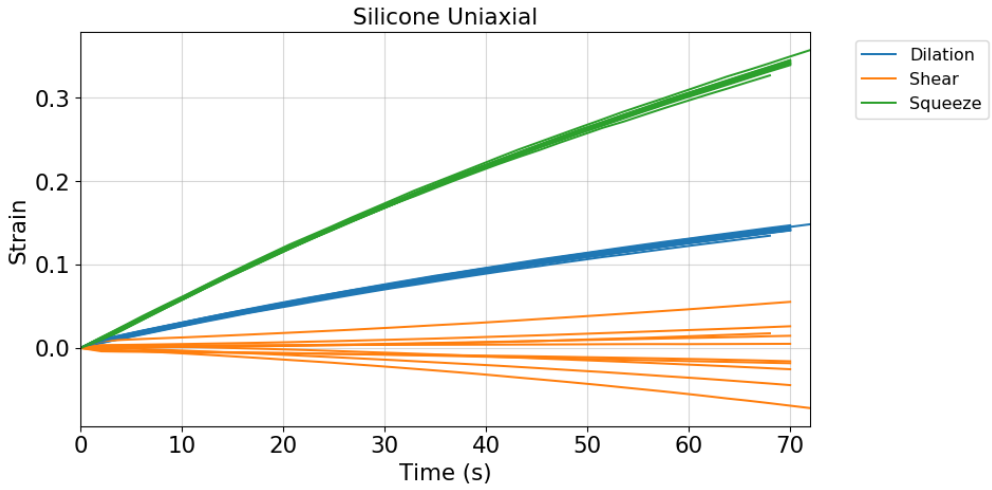

Figure 3.14: The three modes of deformation over the test period for the uniaxial test for all the samples

and repeatable over all the samples for the squeeze and dilation mode, while the shear remains centered around 0.

Using the encoding algorithm described in the Methods section, the squeeze and dilation stresses were calculated as well (Figure 3.15). Since load is applied in one direction only, the dilation stress is equal to the squeeze stress. Consistent curve shapes are seen for all the samples, with the data spreading out slightly at higher strains. Interestingly, the shape of the dilation curve is quite similar to the squeeze curve (in these plots with different X axis scales).

For completeness, the load vs stretch data for all the samples is shown in Figure 3.16a and mean and standard deviation of the load stretch data is also shown (Figure 3.16b). Load values are obtained directly from the load cells, and the stretch values are obtained from DIC analysis (as shown in Figure 3.13b).

3.3.3 Simple shear (Shear)

The simple shear experiment on silicone was already described in Chapter 2 and a thorough analysis of the Green strain and Kirchoff stress was done. Here, the same dataset is used to instead calculate the conjugate stress strain pairs.

Figure 3.17 shows the histogram and strain distribution at the end of the simple shear test

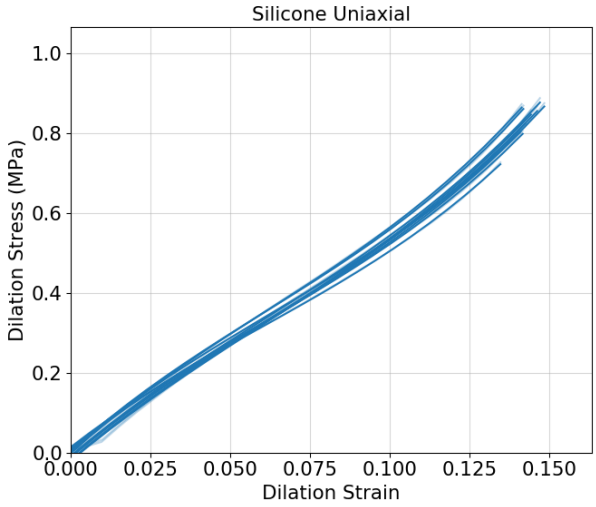

(a) The dilation conjugate stress-strain pair for all the 10 uniaxial tests

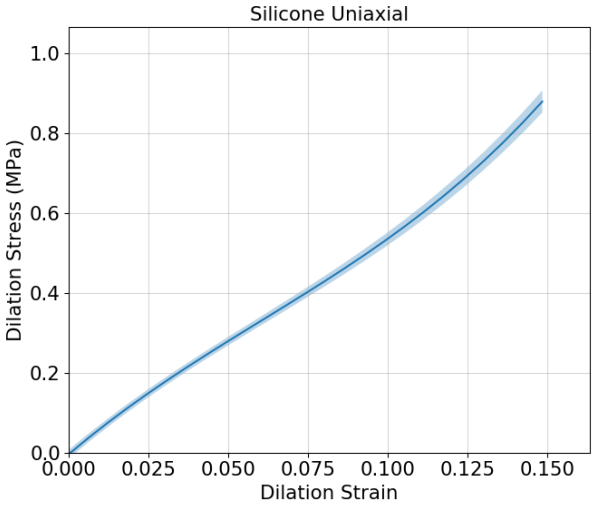

(b) The mean and standard deviation of the dilation conjugate stress-strain pair for all the 10 uniaxial tests

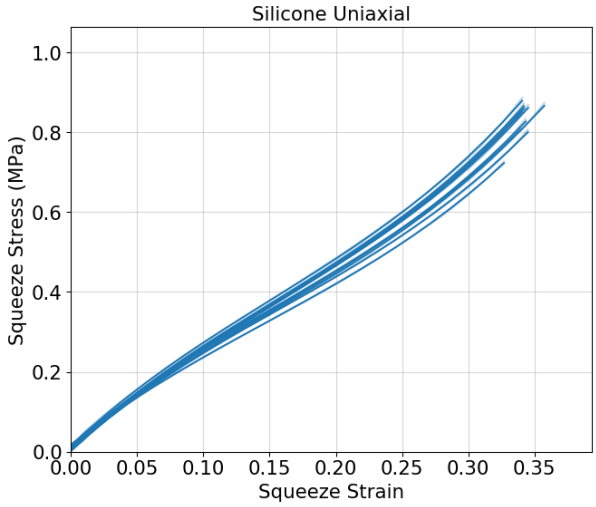

(c) The squeeze conjugate stress-strain pair for all the 10 uniaxial tests

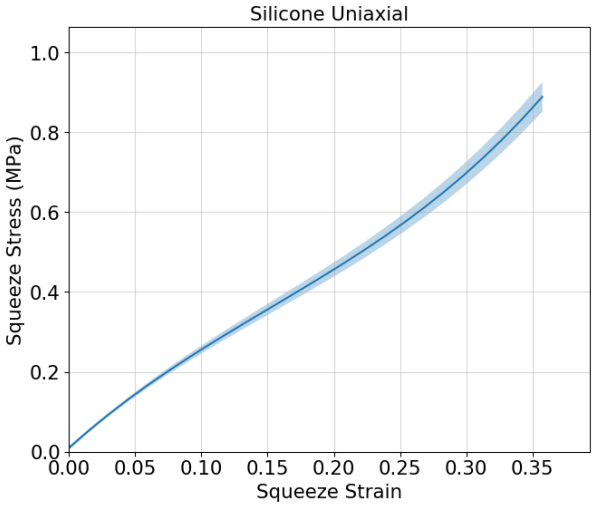

(d) The mean and standard deviation of the squeeze conjugate stress-strain pair for all the 10 uniaxial tests

Figure 3.15: Dilation and squeeze responses of the silicone material under uniaxial tension. Note that the X axis scales are different between the two plots

on a silicone sample. The distribution is very tightly packed around the mean value for all three modes, with a slight spread in the squeeze mode. It can be seen that the homogeneous region of strain extends almost all the way up to the clamps. The dilation and squeeze deformations are from the prestretch phase, while the shear is from the shearing phase, as is clear from 3.18a.

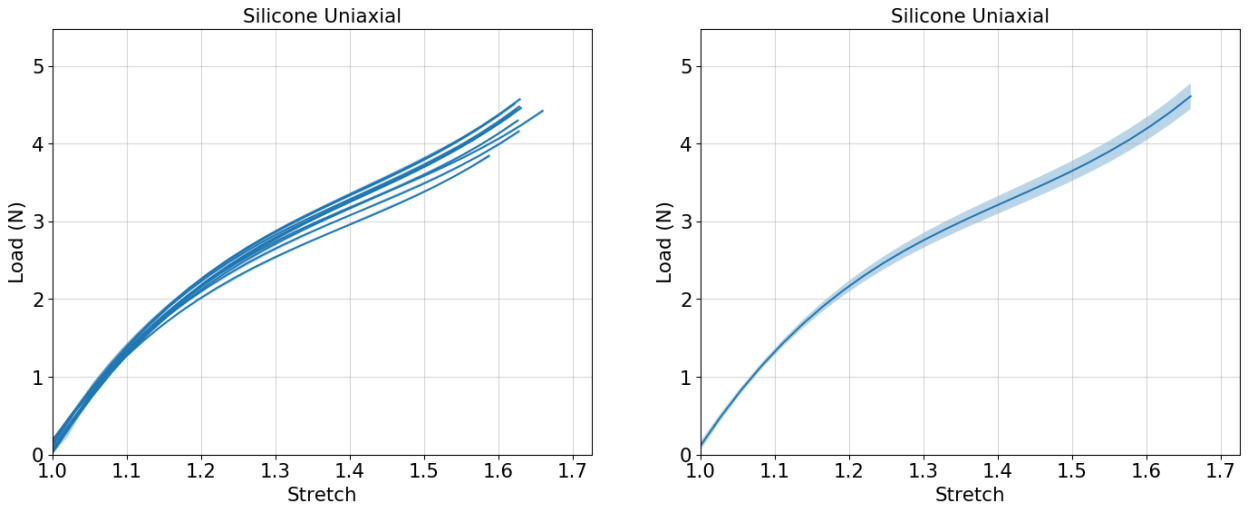

(a) Load vs Stretch for all the uniaxial tests

(b) Mean and deviation for the Load-Stretch curves for the uniaxial tests

Figure 3.16: Load vs Stretch plots show high degree of consistency between the samples for the uniaxial tests

Figure 3.18a shows the the mean, median, mode, values of the 3 modes of deformation during the course of a simple shear test. The distribution is quite tight over the entire course of the test for all three modes, especially shear, the mode of consideration for this test. The dilation and squeeze deformations increase during prestretch, while the shear remains close to 0. After that, the shear increases linearly while the dilation and squeeze remain constant. This is especially clear in Figure 3.18b, where the strain values are offset by their values at the beginning of the shear phase (these are also the average values of the strains from the top and bottom halves of the double lap shear test).

Figure 3.18c shows the two stretches a and b, obtained from the Laplace stretch $\mathscr{U}$. The distribution is quite tight throughout the test. b is in the direction of the applied displacement (Y axis) while a is in the transverse direction, caused by Poisson's effect. Again, b increases during the prestretch phase, while a seems to have an almost imperceptible contraction. They both remain constant during the shearing phase.

Figure 3.19 shows the mean values (over the test surface) of the strain modes through the

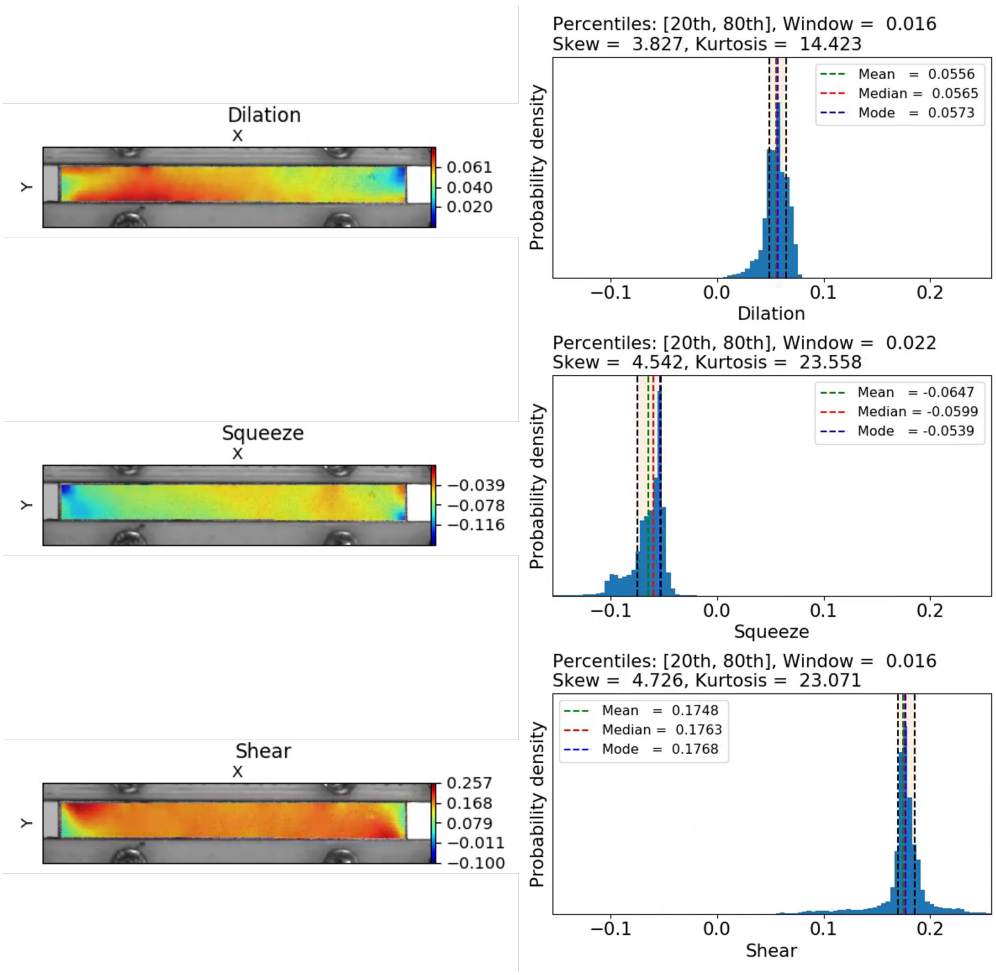

Figure 3.17: DIC analysis showing the distribution of the conjugate strain fields over the test region at the end of the simple shear test. Histograms show the shape of the distribution for these strains

shearing phase of the simple shear test for all 16 samples tested. Both squeeze and dilation are quite constant over the shear phase, (clear from Figure 3.19b).The different prestretch values produce different (but consistent) amount of dilation and squeeze, but in all cases they remain constant during the shearing phase. The higher prestretch also seems to produce a slight larger shear for the same actuator displacement.

Using the encoding algorithm described in the Methods section, the shear stresses were calculated as well (Figure 3.20a). Note that the stretches a and b were offset by their values at the beginning of the shear phase. Consistent curve shapes are seen for all the samples, with the

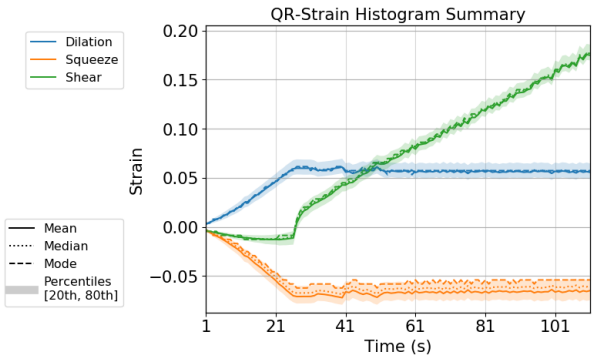

(a) The three modes of deformation over the test period for a simple shear test

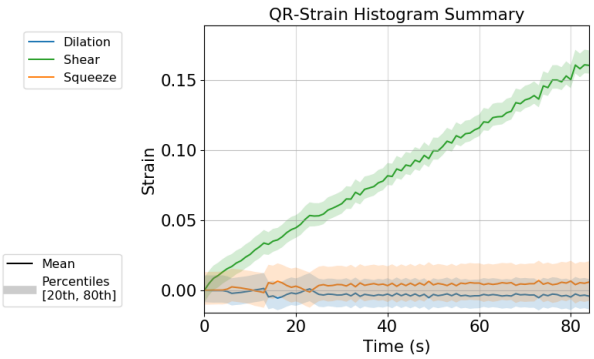

(b) The three modes of deformation over the test period for a simple shear test, offset by their values at the beginning of the shear phase

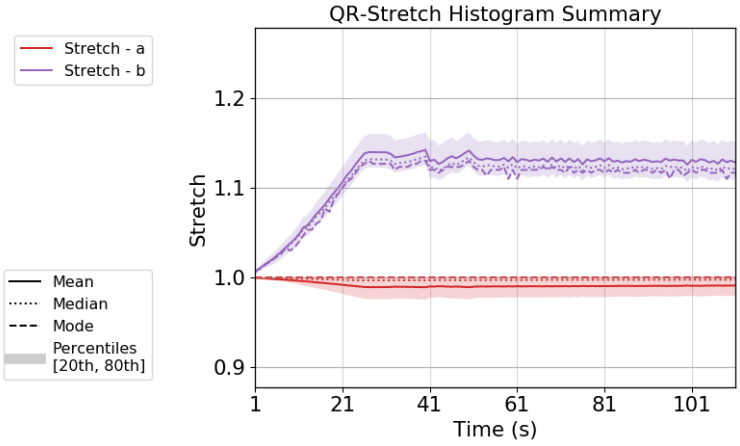

(c) The stretches in the two directions (a - X direction, b - Y direction) for a simple shear test

Figure 3.18: The summary of the strains and stretches obtained through the QR decomposition of the deformation gradient F for a simple shear test. Shaded regions represent the 20th to 80th percentile of the data points

data spreading out slightly at higher strains. From this plot, no obvious difference is notable between the three different prestretches applied.

For completeness, the load vs shear strain (γ) data for all the samples is shown in Figure 3.21a. and the standard deviations of the load stretch data is also shown (Figure 3.21b). Load values are obtained directly from the load cells, and the shear strain values are obtained from DIC analysis.

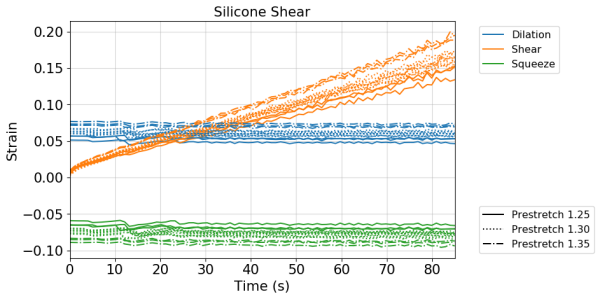

(a) The three modes of deformation in the simple shear test for all the samples

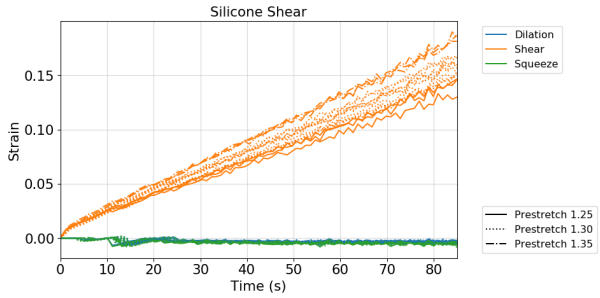

(b) The three modes of deformation in the simple shear test for all the samples, offset by their values at the beginning of the shear phase

Figure 3.19: The three different prestretches applied are denoted by the three different line types. Only the data points after the beginning of the shear phase are shown here

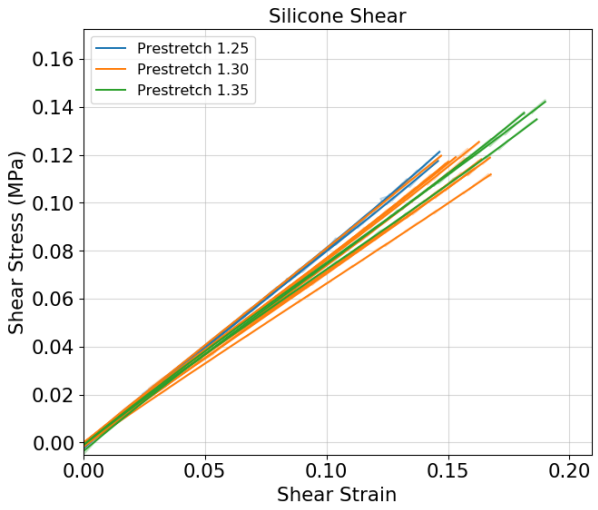

(a) The shear conjugate stress-strain pair

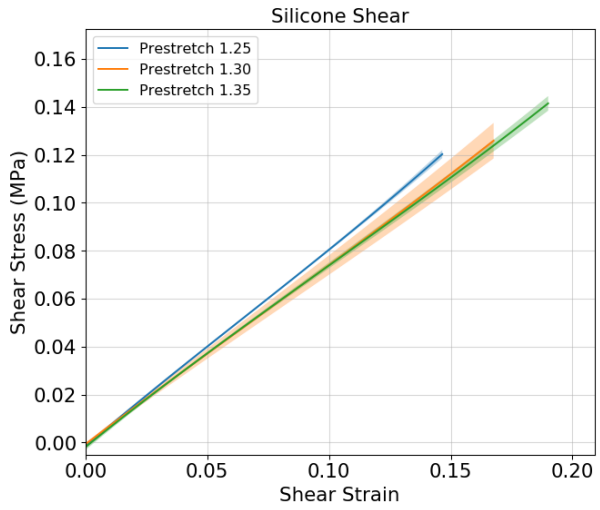

(b) The mean and standard deviation of the shear stress-strain pair

Figure 3.20: Shear stress-strain plots show high degree of consistency between the samples for the 16 simple shear tests

3.3.4 95% Confidence Interval curves for the conjugate pairs

The 95% confidence interval curves for the conjugate stress-strains pairs of dilation, squeeze, and shear are shown in Figures 3.23, 3.22, and 3.24. They all show excellent consistency and repeatability over a significant number of tests.

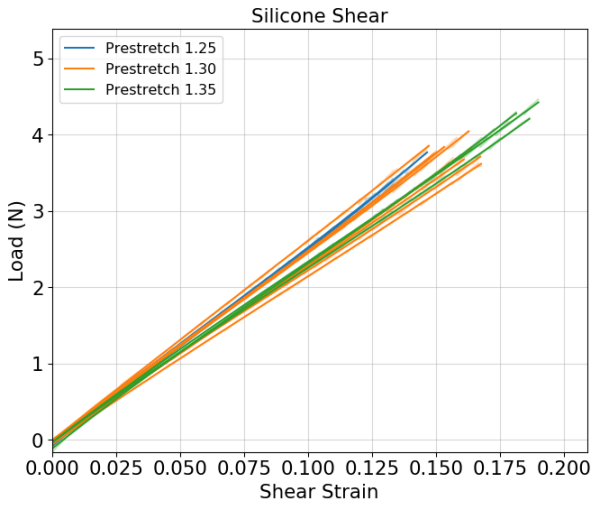

(a) Load vs Shear for all the simple shear tests

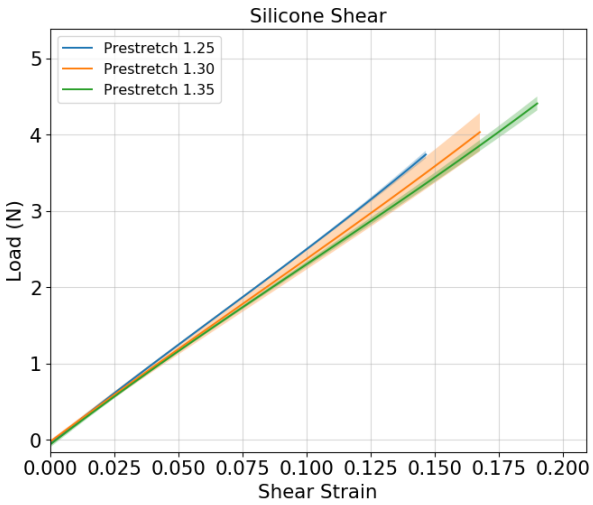

(b) Mean and standard deviation for the Load-Shear curves for the simple shear tests

Figure 3.21: Load vs Stretch plots show high degree of consistency between the samples for the simple shear tests

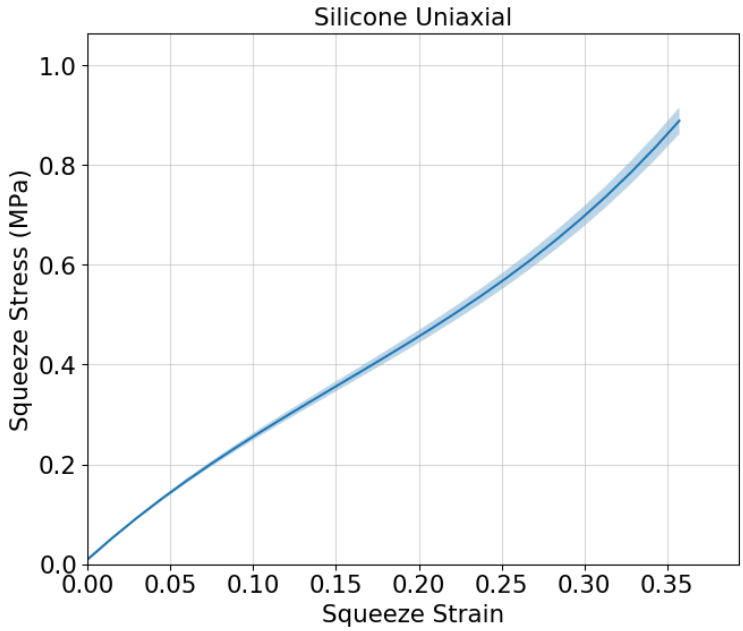

Figure 3.22: The 95% confidence interval curve of squeeze conjugate stress-strain pair from the 10 uniaxial tests

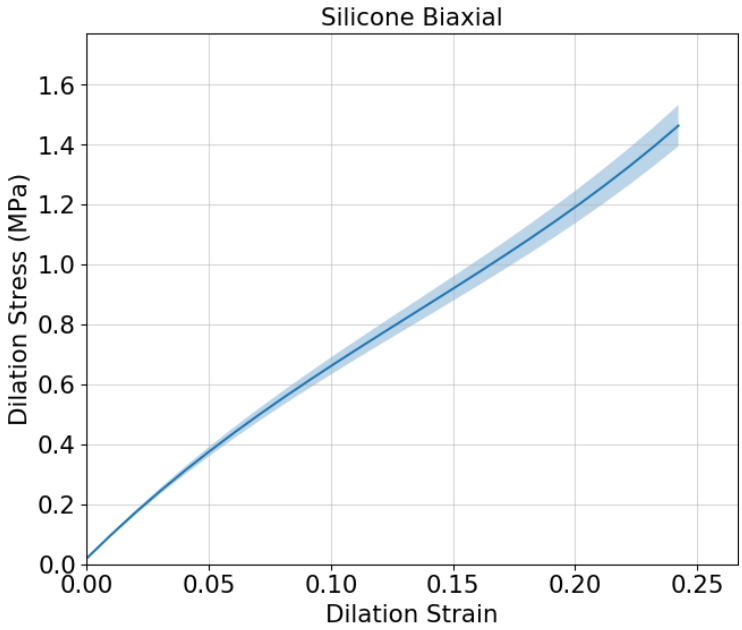

Figure 3.23: The 95% confidence interval curve of dilation conjugate stress-strain pair from the 10 equibiaxial tests

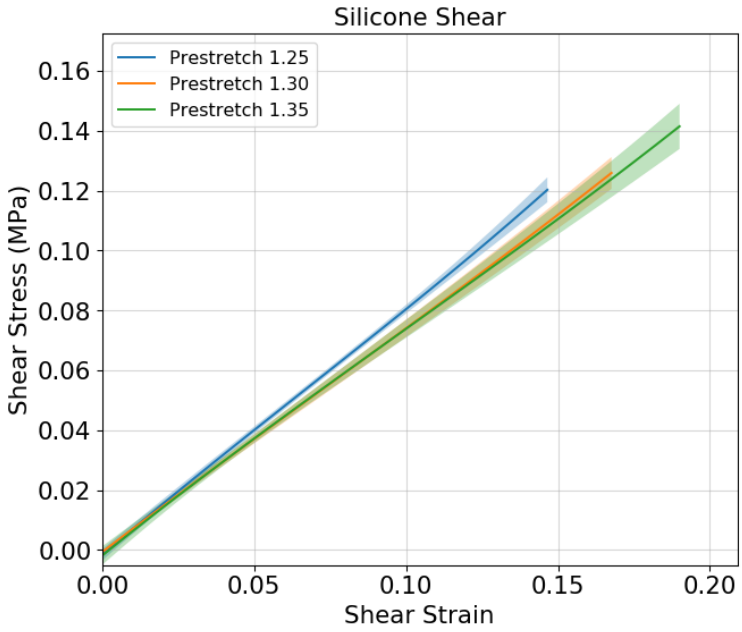

Figure 3.24: The 95% confidence interval curve of shear conjugate stress-strain pair from the 16 simple shear tests (n=3 for 1.25 and 1.35 prestreches, and n = 10 for 1.3 prestretch)

The dilation and squeeze curves appear similar in shape, with an initial softening followed by a stiffening at higher strains. The shear curve appears quite linear over the test range, with a slight hint of softening.

3.3.5 Inhomogeneity of strain field distribution

The normalized inhomogeneity of the strain fields were calculated for the three modes for all the tests, and the mean values and the standard deviations for the final frame in each test are shown in Table 3.1. Additionally, the mean and standard deviation of $max(\overline{'Test-type'\ strain})$ and the Variation Ranges for each test type (over all the tests) is shown for context.

Test type	**max('Test-type' strain)**	**Strain**	**Variation Range**	**Normalized Inhomogeneity**
Equibiaxial extension (n = 10)	(Dilation) 0.228 ± 0.010	Dilation	0.019 ± 0.005	0.085 ± 0.023
		Squeeze	0.028 ± 0.004	0.121 ± 0.015
		Shear	0.076 ± 0.010	0.332 ± 0.040
Uniaxial extension (n = 10)	(Squeeze) 0.342 ± 0.007	Dilation	0.013 ± 0.004	0.039 ± 0.012
		Squeeze	0.027 ± 0.010	0.078 ± 0.029
		Shear	0.077 ± 0.032	0.225 ± 0.093
Simple Shear (n = 10)	(Shear) 0.165 ± 0.016	Dilation	0.020 ± 0.002	0.121 ± 0.014
		Squeeze	0.024 ± 0.002	0.149 ± 0.012
		Shear	0.019 ± 0.002	0.118 ± 0.018

Table 3.1: Normalized inhomogeneity of the strain modes at the final frame of the tests. All values are mean ± standard deviation

All three tests show good homogeneity in their respective strain mode of interest. 60% of the data points, on average, were within 0.12 of the maximum strain for that test.

3.4 Discussion

The three modes of deformation were quite intuitive to understand and easy to extract from the DIC data. The Laplace stretch $\mathscr{U}$ has components a, b, and γ, which were all quite easy to understand, had physical significance in the experimental frame, and were all easy to control

during experiments. Assuming that the silicone material has uniform properties across all the samples, the 95% confidence interval curves of the conjugate pairs (Figures 3.23, 3.22, and 3.24) show great consistency over multiple tests, and suggest that the experimental error introduced by the testing apparatus and experimental system is minimal. This experimental setup and test protocols may then be used to study more complicated materials, like biological tissues, with confidence that the bulk of any variability seen in the data come from the variability in material properties rather than experimental error.

In the equibiaxial and simple shear tests, the dilation ans shear modes (respectively) were activated in isolation to the other modes, as evidenced by the DIC results. In the uniaxial test, both the squeeze and dilation modes are activated. In Figure 3.25, the 95% CI curves of the dilation stress-strain pair from the uniaxial and equibiaxial test are shown together. If these two modes were in fact decoupled, as posited by the theory, the dilation response obtained from any number of arbitrary deformations should all be the same. However, it can be seen that there is infact some difference in apparent material response to the dilation mode, as extracted from these two tests. This could be because the theory is rooted in 2D, and does not consider the effects of the third dimension. These measures obtained are only on the surface of the material and do not provide a complete picture of its behavior. However, the curves are in reasonable proximity to each other, and are of a reasonably similar shape. The membrane is quite thin (0.72mm) compared to the next largest dimension (12.7mm), and so the errors arising from the deformation of the 3rd dimension (the thickness) is minimal in this case. This is then promising for the use of this mode of kinetic and kinematic decomposition for thin membranes.

The shear and squeeze modes are assumed to be decoupled, by this is not necessarily the case (B). Ideally, experiments would be performed where the squeeze mode is studied under different levels of constant shear, and vice-versa. The former is quite difficult to do, but in this work the effect of different constant squeeze levels on the shear behavior can be studied. In the range that this was tested in here (1.25 to 1.35 stretch), qualitatively there is no significant difference between the shear responses, suggesting that it is decoupled from the squeeze mode.

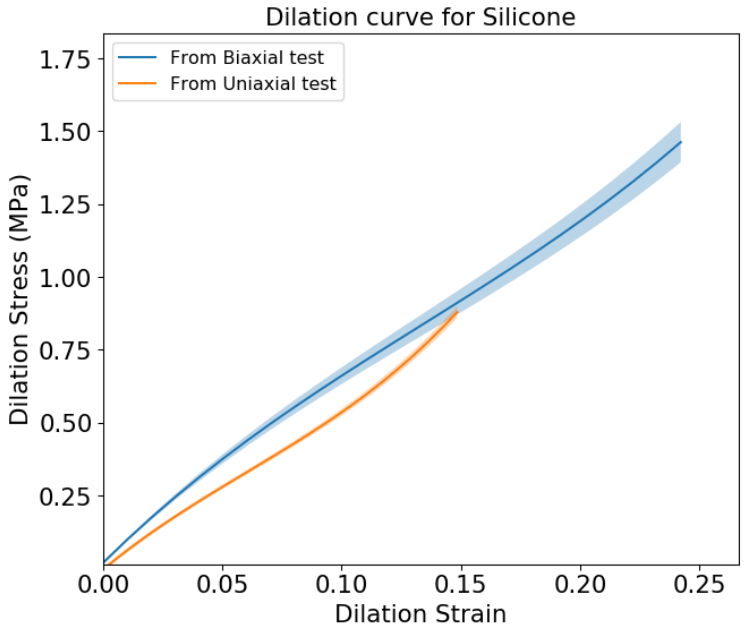

Figure 3.25: The 95% confidence interval curves for the dilation conjugate stress-strain pair from the 10 uniaxial and equibiaxial tests.

However, at higher or lower squeeze values, this may not be the case.

3.4.1 Limitations and future work

While a comprehensive suite of tests have been completed on this silicone material, no attempt has been made to obtain material parameters through the use of the conjugate pairs. This theoretical framework should lend itself to any number of implicit and explicit elastic material models that may fit the data obtained. Silicone rubber has been extensively studied in the past and its behaviour is well characterized using other frameworks. While this framework has been demonstrated to have great utility to experimentalists by providing intuitive and physically observable measurement parameters, it is yet to be seen if this is on par with or superior to the traditional models (like those based on invariant theory). The use of this framework for studying biological tissues is discussed in detail in Chapter 4.

The viscoelastic properties of the material have not discussed here. Stress relaxation tests were conducted in both the uniaxial and equibiaxial tests, but these results have not been incor-

porated into the material response at this time. As discussed in detail in Chapter 2, in the simple shear experiment the moment loads applied by the material are measured over the course of the test. These have not been studied here in conjuction with their shear characteristics.

While the modes have all been studied individually, no attempt has been made to apply all three modes simultaneously and verify that the material responses are predicted by the results from these tests. A finite element analysis with the correct boundary conditions, using this theoretical framework to predict material behavior, and an appropriate constitutive model will provide a lot of support for use and wide adoption of this framework for mechanical characterization.

3.5 Conclusion

A novel theoretical framework where deformation gradient F is decomposed with the QR technique instead of the traditional polar decomposition was discussed. Three modes of deformation arise naturally from this type of decomposition, and a framework for constitutive modeling using the conjugate stress-strain pairs arising from this decomposition (dilation, squeeze, and shear) was given. Tests were conducted on a thin engineering soft material, silicone, to obtain the material response to these three modes. 10 equibiaxial, 10 uniaxial, and 16 simple shear tests were conducted. The 95% confidence interval curves for the conjugate stress-strains pairs of dilation, squeeze, and shear were obtained from the equibiaxial, uniaxial, and simple shear experiments respectively. This framework shows promise in its utility for studying the mechanical characteristics of thin membranes and biological tissues, while providing greater intuition and understanding to the experimenter.

4.1 Background

4.1.1 Freed-Rajagopal model for 1D biological fibers

Freed and Rajagopal developed a novel implicit model for 1D biological fibers[18]. They model the material as elastic, with the strain being the combination of a Hookean fiber and a strain-limiting fiber (analogous to a slack string). This is similar to what is hypothesised for biological fibers. Most tissues are primarily made of elastin and collagen, with the collagen being in a wavy "crimped" state at rest. When the material is deformed, initially the majority of the response is from the elastin while the uncrimping collagen does not contribute signficantly (Toe region in Figure 4.1). The heel region occurs as the deformation continues, where the collagen fibers begin to straighten out and share the load-bearing. Finally, the linear region is where the load-bearing is primarily due to the taut collagen fibers. This model tries to capture this behaviour in a physically intuitive way. The mechanical behavior of soft tissues is modeled using three parameters: a initial stiffness (E^E due to the elastin), a terminal stiffness (E^C due to the collagen), and a transitional strain ($\beta = 1/\varepsilon_{crimpmax}$ in Figure 4.1).

The strain response to a applied stress is given by

$$\varepsilon = \frac{1}{\beta}\left(1 - \frac{1}{(1+(\beta-1)\sigma/E^E)^{\beta/(\beta-1)}}\right) + \frac{\sigma}{E^C} \tag{4.1}$$

where ε is the strain induced in the material by a stress σ, and E^E, E^C, and β are explained in Figure 4.1. The model is derived from first principles of thermodynamics, and is therefore different from purely empirical efforts to capture the same parameters from the curve[25].

It has also been shown that this model performs better than the Fung and the Holzapfel-Gasser-Ogden 1D models in terms of parameter sensitivity and capturing behavior at lower strains[26]. These parameters are physically intuitive, can be extracted graphically, and provide intuitive design targets for tissue engineers trying to mimic the mechanical behavior.

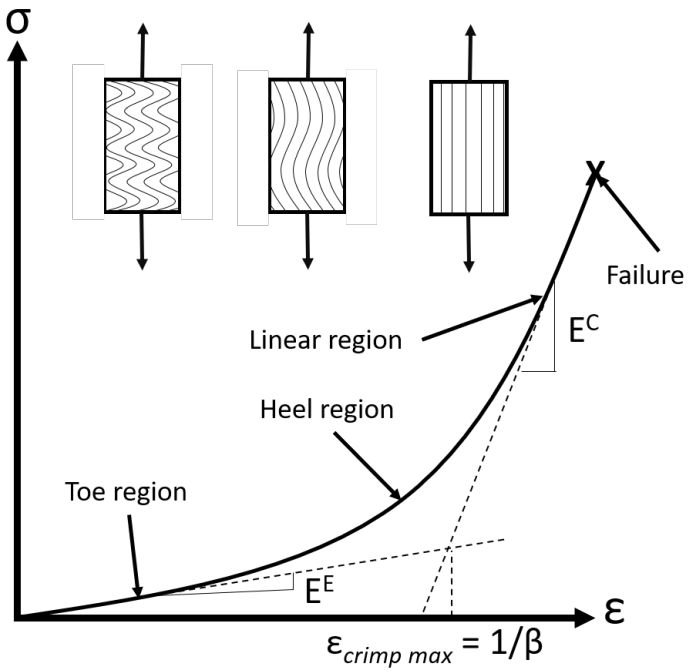

Figure 4.1: Typical stress-strain curve for a biological tissue, re-purposed from [18].

4.1.2 Extension to planar membranes

Freed et al have also extended this theory to planar tissues [16]. Using the QR decomposition of the deformation gradient F, a stress-strain curve is obtained for each conjugate stress/strain pair from each mode of deformation (Section 3). Similar to the 1D fiber model, 3 parameters are then used for each curve, thus resulting in a 9 parameter model to describe the material mechanically. The dilatoric response is given by

$$\delta = \frac{\langle \pi \rangle}{4K^C} + \frac{1}{\beta^d}\left(1 - \frac{1}{1 + (\beta^d - 1)\langle \pi \rangle / 4K^E)^{\beta^d/(\beta^d - 1)}}\right), \beta^d > 1, \tag{4.2}$$

the squeeze response is given by

$$\varepsilon = \frac{\sigma}{2M^C} + \frac{sgn(\sigma)}{\beta^q}\left(1 - \frac{1}{1 + (\beta^q - 1)|\sigma| / 2M^E)^{\beta^q/(\beta^q - 1)}}\right), \beta^q > 1, \tag{4.3}$$

and the shear response is given by

$$\gamma = \frac{\tau}{G^C} + \frac{sgn(\tau)}{\beta^s}\left(1 - \frac{1}{1 + (\beta^s - 1)|\tau|/G^E)^{\beta^s/(\beta^s-1)}}\right), \beta^s > 1, \tag{4.4}$$

where the moduli K^C, M^C, G^C are the terminal stiffnesses, moduli K^E, M^E, G^E are the initial stiffnesses, and $\beta^d, \beta^q, \beta^s$ are the reciprocal measures of the transitional strains in dilation, squeeze, and shear modes respectively (where the conjugate stress/strain pairs $\{\pi, \delta\}$, $\{\sigma, \varepsilon\}$, and $\{\tau, \gamma\}$ describe uniform dilation, squeeze, and shear respectively).

Here, the responses to all three modes are assumed to be decoupled. A model where the dilation is decoupled, but the squeeze and shear responses are coupled has been developed as well (Personal communication with Dr. Freed, refer Appendix A).

4.1.3 Motivation

In Chapter 3, the use of the novel theoretical framework to analyse the mechanical response of an engineering material, silicone, was discussed and a method to obtain these conjugate stress-strain pairs experimentally was validated. To further this work and make it relevant in the context of biological tissues, this method will now to applied to a set of biological tissues. Specifically, rat skin will be used as the biological tissue of interest. Skin can be reasonably approximated to have a 2D response field, in that typically the loading and deformation it experiences is over its surface. The skin is harvested from rats to improve the ease of obtaining the material, thus allowing for large sample numbers, because of the lack of special permissions or equipment need to handle these tissues.

4.2 Methods

4.2.1 Sample preparation

For the tests performed here, all the samples were obtained from 4 male Lister black hooded rats between 12 to 15 weeks old and weighing between 400g to 475g. Depilatory cream (Nair^{TM} Hair Remover) was applied using manufacturer instructions and the fur was removed from the

dorsal section. From each rat, samples for 2 simple shear tests, 2 equibiaxial tests, and 4 uniaxial tests were obtained. On a given testing day, one rat was euthanized with CO2, followed by secondary euthanasia by bilateral thoracotomy. Then all of the samples listed above were harvested and tested on the same day within 12 hours of euthanasia. This was repeated with 4 rats in total.

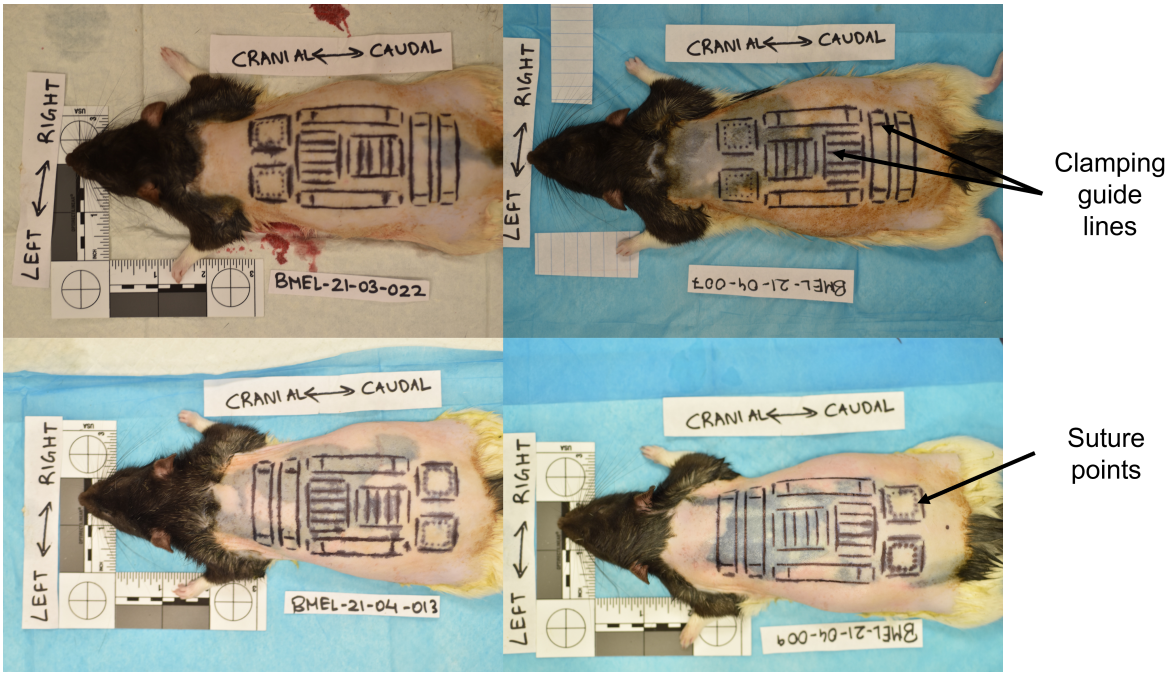

Figure 4.2: The sample shapes drawn on dorsal skin of the 4 rats. The location of the sample types are switched between rats. Square patterns are for the equibiaxial tension tests, long skinny rectangular samples for the uniaxial tension tests, and the other rectangular samples are for the simple shear test.

Figure 4.2 shows the 4 rats used in the study. The pattern was made by laser cutting a thin film of PET with holes at the required locations. The shapes were exactly the same size as the punches used for the different tests. The square samples had holes for marking the suture locations, while the uniaxial and simple shear samples had horizontal lines across the sample marking the clamping location at the chosen gauge length. The template was contoured around the shape of the rat's back and the markings were made with black sharpie.

Following this, the dorsal skin was excised and any subcutaneous fat was removed. It was then stored in cotton gauze soaked in PBS solution and kept in ice prior to transport to testing location. A mallet and alloy steel leather punches of the appropriate size for each test were used to obtain the samples from the dorsal skin. The skin typically contracted after excision, so it was stretched so that the pattern drawn on the skin matched the shape of the punch and then the sample was punched out. The sample dimensions after punching out were measured optically by placing them next to calibrated scales. The samples were between 1.9mm to 3mm in thickness. The speckle pattern for DIC analysis was applied using black spray paint (Universal Premium Spray Paint, Flat Black,Rust-Oleum, IL, USA). 100lb load cells (Model 31, Honeywell, NC, USA and LSB210, Futek, CA, USA) were used for all load load measurements. Samples were stored in PBS soaked cotton gauze and refrigerated at 4°C before warming to room temperature in a water bath for the test. All tests were conducted at room temperature without any environmental chambers in the biaxial system described previously [21]. For the uniaxial tension and simple shear tests, serrated clamps with needles were used (described in [22]). For all the tests, in the final loading ramp of the test, an arbitrary small load was used to determine when the sample was under tension, and this was used as the starting point for the DIC analysis. All tests were done with displacement control.

4.2.1.1 Equibiaxial tension

Equibiaxial tension tests were performed with sutures. As discussed in Chapter 3, in order to allow in-plane shearing, the suture set up was based on the work of Sacks et al [24]. However it was decided that the 3D printed set-up used for silicone may not withstand the higher loads from testing rat skin. Therefore a more robust system with bearings, pulleys, and machined aluminium blocks was used. Figure 4.3 shows the design of the system. Each pivot black rotated on a rotary bearing to allow for load distribution. Each suture line (braided fishing line) was tied to two sutures (fishhooks) and attached to the sample. This line was passed around a ball bearing pulley to reduce the friction working against the equalization of the load over the 4 points on each side.

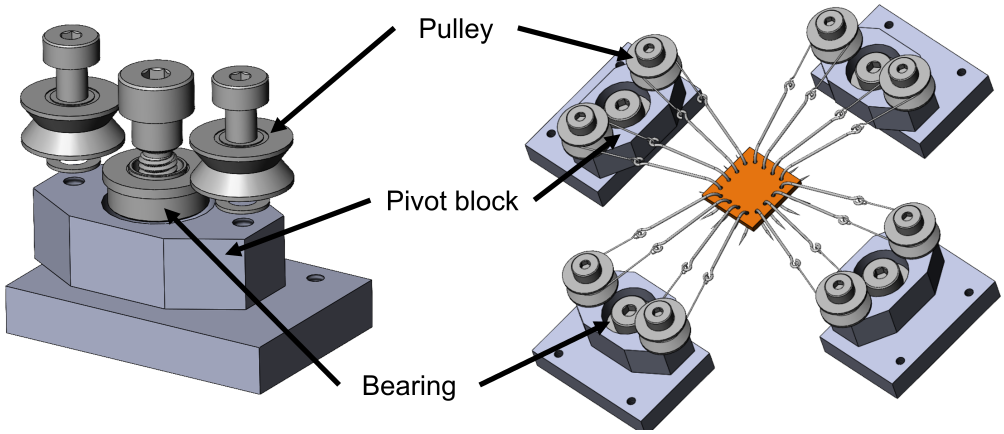

(a) 3D rendering of the pivot block used in the equibiaxial tests

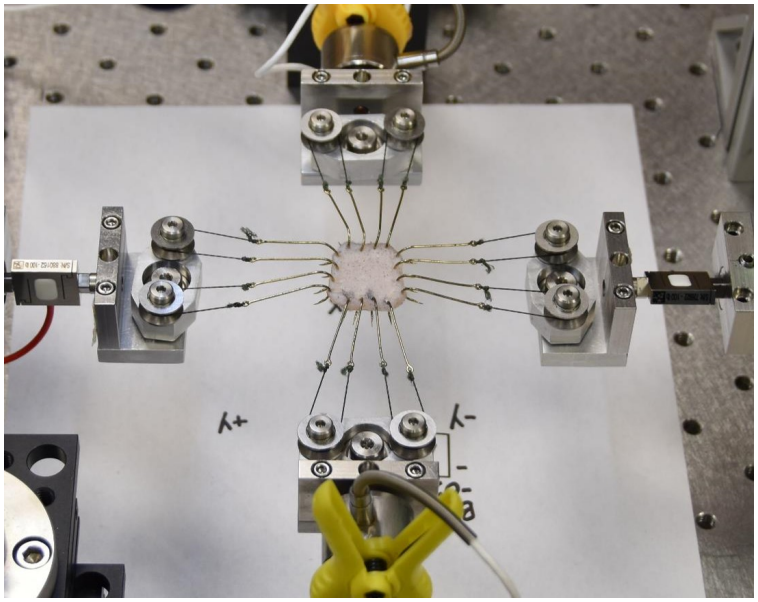

(b) The set-up in use with the biaxial system on a rat skin sample

Figure 4.3: The suture set-up used for equibiaxial tension tests on rat skin

A total of 8 samples were tested in equibiaxial tension, 2 each from 4 rats. Figure 4.2 shows how of the 8, 4 were harvested from near the shoulder of the rat, while 4 were closer to the tail. Figure 4.2 also shows the locations of the sutures as well. For these tests, the size of the punch used to get the sample, and so the shape of the pattern drawn on the rat, was 18.27mm x 18.27mm. 4 points were marked for sutures on each side, with 3.05mm between adjacent suture points. The suture points made a square shape of size 12.7mm x 12.7mm between them. For

each pair of samples harvested per rat, for one sample, the excised skin was stretched to match the size of the punch prior to punching. For this sample, the sutures were placed at the locations marked on the skin. For the other sample, the skin was allows to relax before punching, i.e there was no effort made to use the drawn pattern. The sutures were placed without the use of the pattern dots as well. This was done in an effort to see if the process of maintaining *in-vivo* configurations prior to testing had an effect on the perceived material properties. In order to place the sutures accurately, evenly spaced, and consistently for all the samples, a specially made 3D printing alignment tool was used (Figure 4.4.

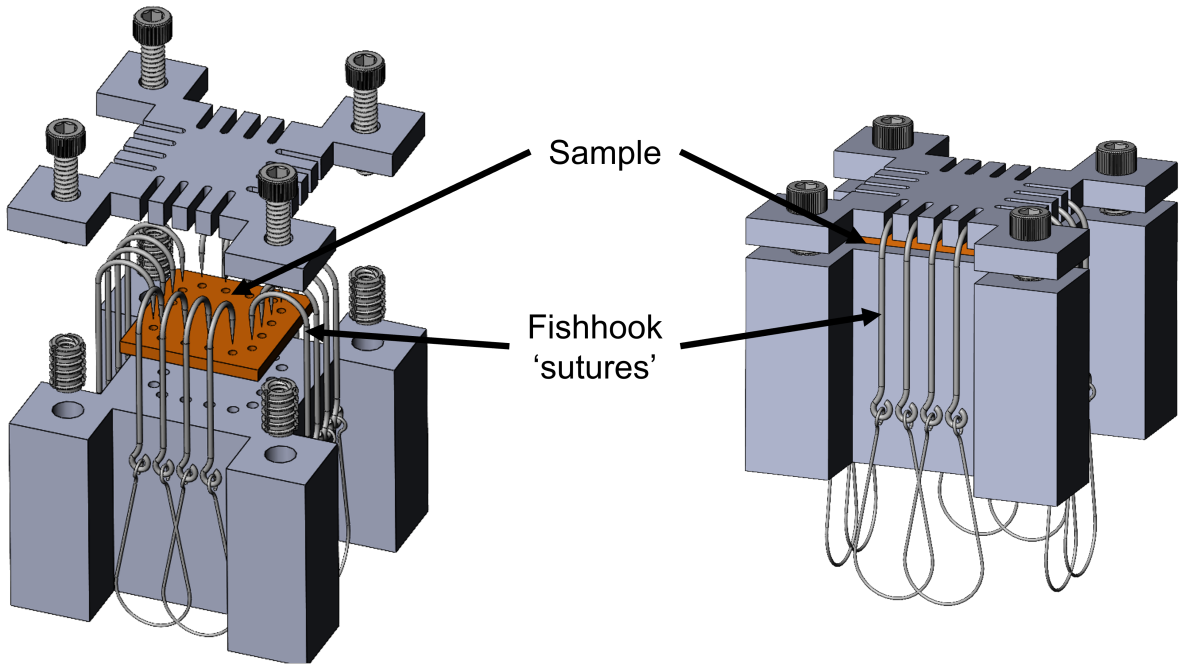

Figure 4.4: 3D rendering of the suture placement jig. The sample is gently held in place by tightening the screws, and the fishhooks are placed with the help of the guides on the top plate and pierce through the holes in the bottom piece.

Once the sutures were placed, the sample was spray painted and mounted on the testing system with a small amount of slack on the lines. 7 cycles of preconditioning were performed, with ramp load and unload to an amplitude of stretch of 1.5 (on a gauge length of 12.7mm), with each ramp occuring in 50.0s (or a rate of 1% engineering strain per second). Immediately

following the 7 cycles, the same ramp loading was performed again and this loading ramp was used for all DIC and data analysis. Data and images were recorded at 1Hz.

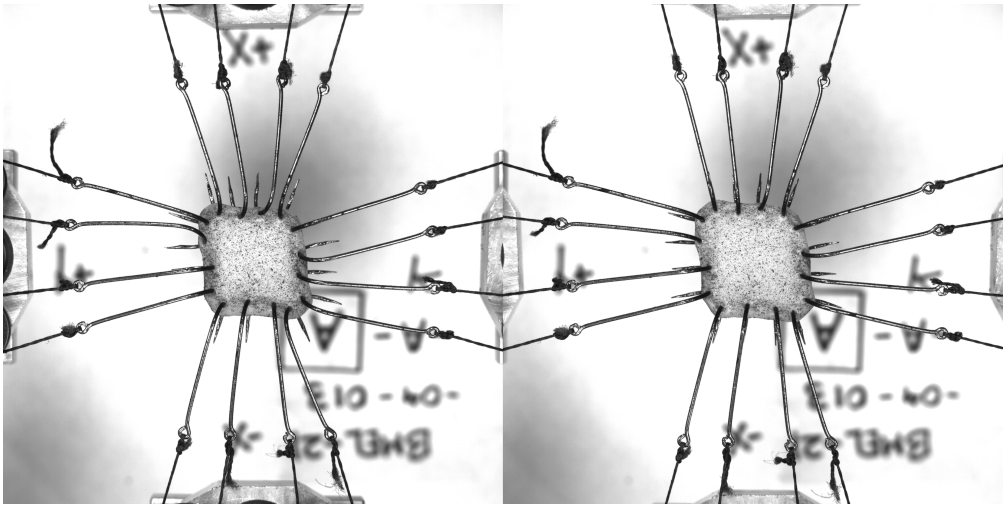

Figure 4.5: Initial (left) and final (right) images of the final loading ramp for equibiaxial test of rat skin

4.2.1.2 Uniaxial tension

From each rat, 2 uniaxial samples each along the Cranial-Caudal (CC) direction and 2 along the Medial-Lateral (ML) direction were obtained. Of the 4 rats, in 2 of them the ML samples were from the shoulder region while in the other two they were from near the tail region. Once the skin was excised from the rat, the punch used to get the samples was of size 49.962mm x 7.620mm. After the samples were punched out, they were all clamped at a gauge length of 33.02mm through the use of a 3D printed alignment jig. The horizontal lines drawn on the rat at this length were used and the clamp was placed at that location. After that they were spray painted and mounted on the system without any additional stretching.

For CC samples, 7 cycles of ramp load and unload preconditioning was applied to an amplitude of 1.8 stretch on a gauge length of 33.02mm in 80 seconds (or a rate of 1% engineering strain per second). Immediately following the 7 cycles, the same ramp loading was performed

again and this loading ramp was used for all DIC and data analysis. Data and images were recorded at 0.5Hz.

For CC samples, 7 cycles of ramp load and unload preconditioning was applied to an amplitude of 1.5 stretch on a gauge length of 33.02mm in 50 seconds (or a rate of 1% engineering strain per second). Immediately following the 7 cycles, the same ramp loading was performed again and this loading ramp was used for all DIC and data analysis. Data and images were recorded at 1Hz.

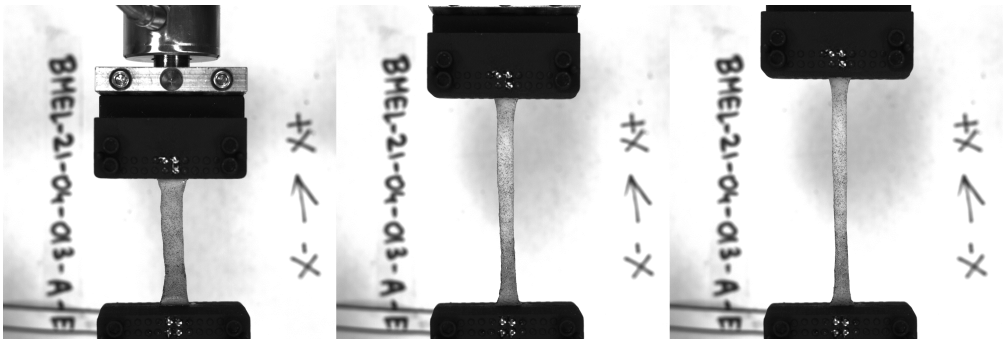

Figure 4.6: Initial (left) image at the start of the first cycle of preconditioning. The middle image shows the image used as reference for the DIC analysis, and the right image shows the sample at its fully stretched state in the final loading ramp.

It was noticed that the sample deformed considerably during the first loading cycle and never recovered it's shape during the course of the test (Figure 4.7). In order to get a more reasonable estimate of the cross-sectional area at the 'reference' configuration at the start of the DIC analysis in the final ramp, the original undeformed cross section was divided by the stretch measured with the grips on an original length of 33.02mm.

4.2.1.3 Simple shear

From each rat, one sample was obtained to apply shear in the CC direction, while the other was oriented in the ML direction. The pattern drawn on the rat was used to stretch it to the desired shape of 24.89mm by 18.85mm, which was the shape of the punch used. As previously

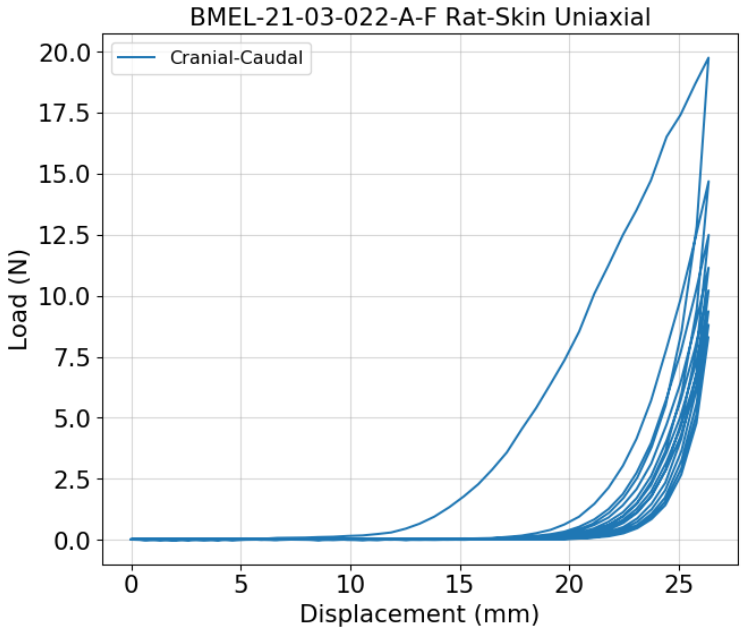

Figure 4.7: Load vs Stretch for a rat skin sample under uniaxial tension

described in Chapter 2, the samples were clamped with the help of the lines drawn on the sample as well as a 3D printed alignment jig and mounted on the novel jig. Samples were clamped at a length of 3.94mm between the clamps, with the width varying between 15-18mm for an approximate aspect ratio of 4:1. A prestretch of 1.76 was applied in the transverse direction in 76.0s and held at that position for 300.0s. This was followed by application of shear by moving the central actuator 38.10mm in 150.0s (0.01 inches/s). This protocol was adopted instead of the preconditioning protocol applied on the silicone because the device was unstable under unloading conditions with the rat skin. It was also noticed that there was a significant amount of stress relaxation occurring following the prestretch, so a hold time was used to allow the loads to asymptote prior to the application of the shear deformation (2.5.1). Overhead images for DIC analysis and load and grip displacement data were captured at 0.5Hz.

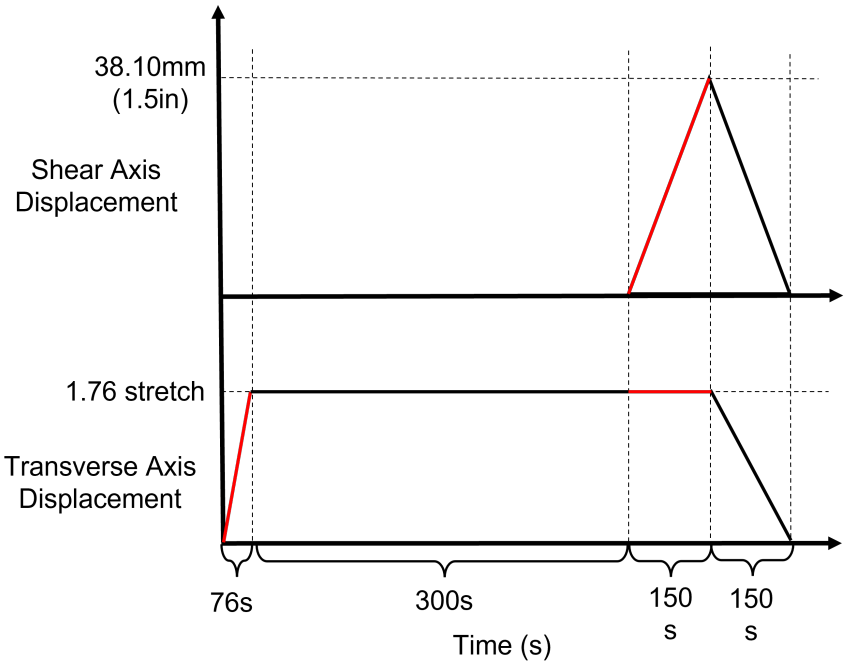

Figure 4.8: Test protocol for simple shear of rat skin

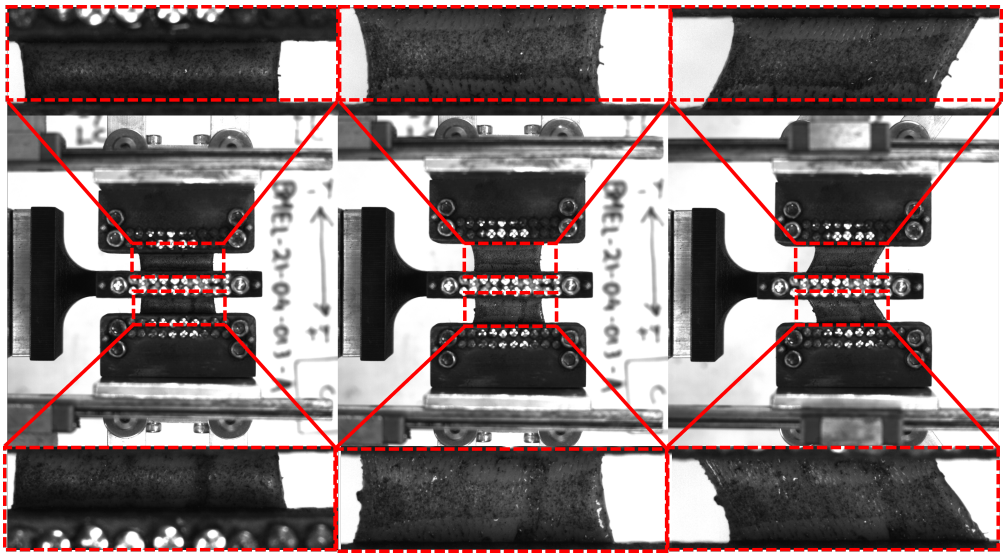

Figure 4.9: Initial (left), after prestretch (middle) and final (right) images of the final test ramp for shear test of silicone.

4.2.2 Data analysis

4.2.2.1 DIC analysis

The methods for data analysis have already been discussed in 3.2.2 and are reproduced here for convenience.

DIC was performed on the entire test region for all the tests. The encoding algorithm from [16] is used to calculate the conjugate strain values for the three modes dilation, squeeze, and shear, over the entire test area for all the tests. As detailed in Chapter 2, histograms were plotted depicting the distribution of the strain field data points in each frame. Using this, the mean, median, mode, and 20th and 80th percentile of the data points were tracked over the entire test period to get a sense of the strain field and the homogeneity. Consistency of the applied strain was tracked for all the samples, and the uniformity of the strain distribution was quantified similar to Eq 2.2. Here, instead of Green strain, the conjugate strain values were used to define Uniformity as Uniformity of strain field = (80th - 20th percentile of strain field)/max(Test-type strain), where the test-type strain is dilation for biaxial tests, squeeze for uniaxial tests, and shear for simple shear tests. Finally, the conjugate stress-strain pairs were plotted for each test. For all tests, in the final ramp, the reference image and data point was chosen based on the time at which the loads crossed a small, arbitrary critical threshold. This was done to remove any images with the material under slack that will convolute the DIC analysis.

The encoding algorithm from [16] is used to calculate the conjugates stresses and strains from the DIC analysis. The conjugate stresses are calculated as

$$\begin{aligned} \pi &:= \tilde{S_{11}} + \tilde{S_{22}}, \\ \sigma &:= \tilde{S_{11}} - \tilde{S_{22}}, \\ \tau &:= \frac{a}{b}\tilde{S_{12}}, \end{aligned} \tag{4.5}$$

and the conjugate strains are

$$\begin{aligned} \delta &:= ln\sqrt{ab}, \\ \varepsilon &:= ln\sqrt{a/b}, \\ \gamma & \end{aligned} \tag{4.6}$$

$\tilde{S}$ or material stress, is defined as $\tilde{S} := Q^T sQ$, where Q is the rotation matrix obtained from a QR decomposition of the deformation gradient F, and s is the Kirchoff stress. $s = PF^T$ where P is the first Piola-Kirchoff stress.

For all these tests, DIC analysis is performed and the Lagrangian displacement gradients are obtained. The deformation gradient is obtained by $F = \partial u/\partial X + I$ where $\partial u/\partial X$ is the displacement gradient and I is the identity tensor. This is then used to calculate $\mathscr{U}$ and Q as described in the Appendix section of [16]. For each frame, F and Q are averaged over all the points on the surface. These average tensors are then used to transform P (which is tractions over inital areas, easily measured in experiments) and s as described earlier to get the conjugate stress strain pairs for the uniaxial and biaxial tests. For the simple shear tests, s is obtained directly from 2.1.

The 95% confidence interval calculations were made by resampling the curves with cubic spline smoothing, and then the interval was calculated using a t-distribution.

4.2.2.2 Freed-Rajagopal model fit

From each equibiaxial test, the dilation stress-strain curve was taken and the Freed-Rajagopal model to fit to the data. This was done by getting the tangent slopes at the beginning and final linear portions of the curve, and calculating the transition strain by locating their intersection point (Figure 4.1). After this, the three parameters (initial stiffness, final stiffness, and transition strain) were manually adjusted to get the best fit to the data for each mode of deformation, using Eqs 4.2, 4.3 and 4.4. A Root Mean Squared Error value was calculated for each curve and normalized by the maximum strain value.

4.3 Results

4.3.1 Equibiaxial tests (Dilation)

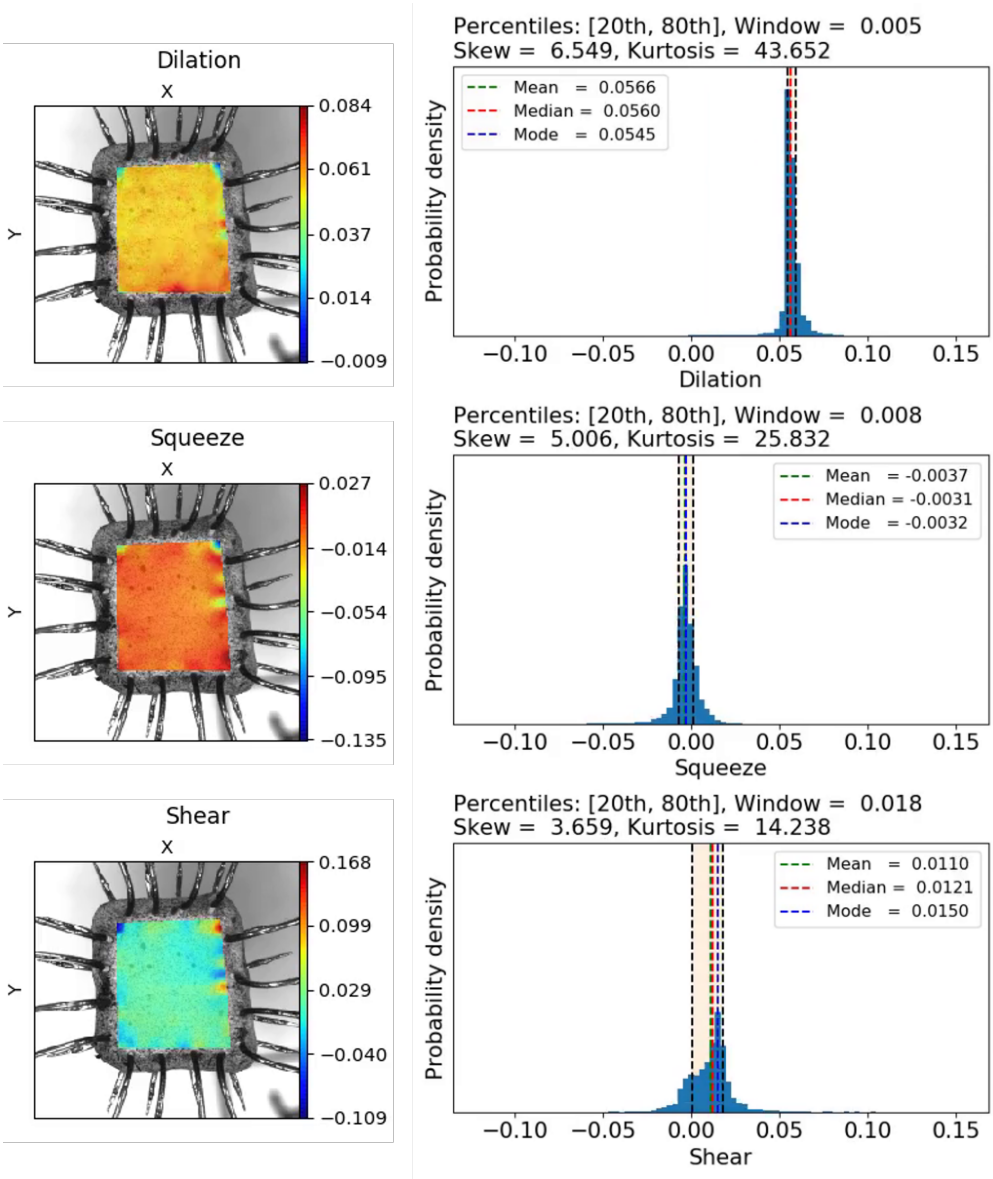

Figure 4.10: DIC analysis showing the distribution of the conjugate strain fields over the test region at the end of the equibiaxial test. Histograms show the shape of the distribution for these strains

Figure 4.10 shows the histogram and strain distribution at the end of the equibiaxial test

on a rat skin sample. The distribution is tightly packed around the mean value for all three modes, showing a very uniform distribution of strain. The shaded region in the histogram represents 60% of the data points over the entire surface, or the 'window'. It can be seen that the homogeneous region of strain extends almost all the way up to the sutures. Additionally, in this equibiaxial test, both squeeze and shear strains remain close to 0 while only the dilation strain is active, demonstrating that this test is appropriate for studying the response of materials in dilation alone.

Figure 4.11a shows the the mean, median, mode, values of the 3 modes of deformation during the course of an equibiaxial test. The shaded regions represent the 20th to 80th percentile windows. For dilation, the distribution is quite tight over the entire course of the test for dilation, the mode of consideration for this test. The shear strain distribution seems to spread out at larger strains, with the mean value increasing gradually through the experiment. The squeeze had a tight distribution as well, although it tended to increase at larger strains.

Figure 4.11b shows the two stretches a and b, obtained from the Laplace stretch $\mathscr{U}$. The distribution is quite tight and the stretches in the two directions are very close to each other, demonstrating that equibiaxial deformation is achieved. Although this was the case in this representative plot for this sample, in general it was noticed that this was not the case, and the stretches in the two directions tended to be different.

Figure 4.12 shows the mean values (over the test surface) of the strain modes through the equibiaxial test for all 8 samples tested. The shear strain curves are spread out, but appear to be centered around 0 strain. There seems to be a slight amount of squeeze in most samples as well. The dilation strain is reasonably consistent across the samples.

Using the encoding algorithm described in the Methods section, the dilation stress was calculated as well (Figure 4.13a). The typical J-curve is seen here for the samples, with a low stiffness region to begin with that stiffens at higher strains. Figure 4.13b shows a seeming difference in properties between the samples harvested near the tail vs the shoulder regions of the rat.

The Freed-Rajagopal model was fit to all these curves graphically as described in section

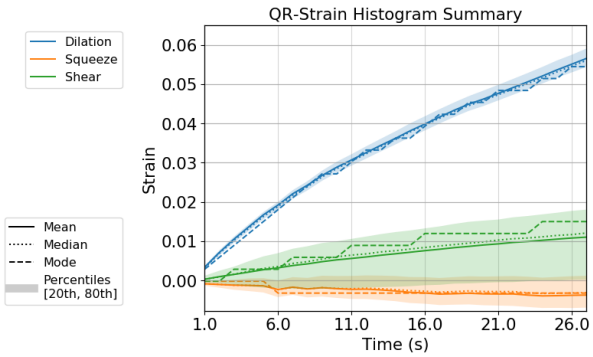

(a) The three modes of deformation over the test period for an equibiaxial test

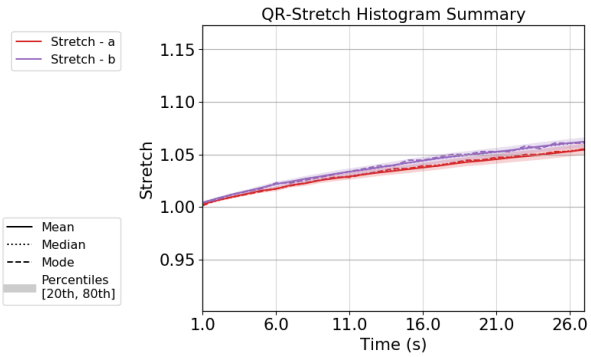

(b) The stretches in the two directions (a - X direction, b - Y direction) for an equibiaxial test

Figure 4.11: The summary of the strains and stretches obtained through the QR decomposition of the deformation gradient F for an equibiaxial test. Shaded regions represent the 20th to 80th percentile of the data points

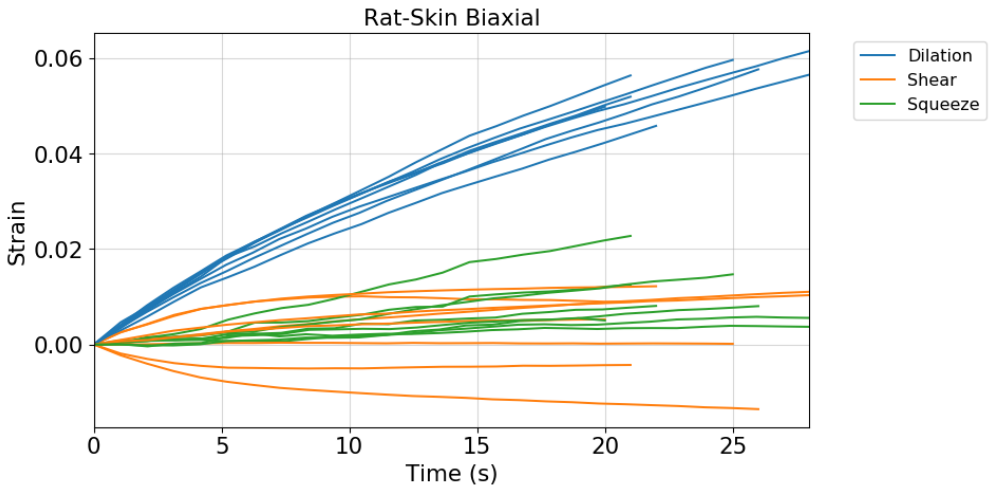

Figure 4.12: The three modes of deformation over the test period for the equibiaxial test for all the samples

4.2.2.2. An example plot from one the tests is shown in Figure 4.14. The model curve shows excellent fit with the test data, with a normalized root mean squared error (NRMSE) of 0.0153. The red dotted line shows the initial tangent slope, the blue dotted line shows the final tangent slope and the green dotted line shows the transition strain. $E^E = 4K^E$, $E^C = 4K^C$, and $1/\beta = 1/\beta^d$ for K^E, K^C and β^d defined in Eq 4.2.

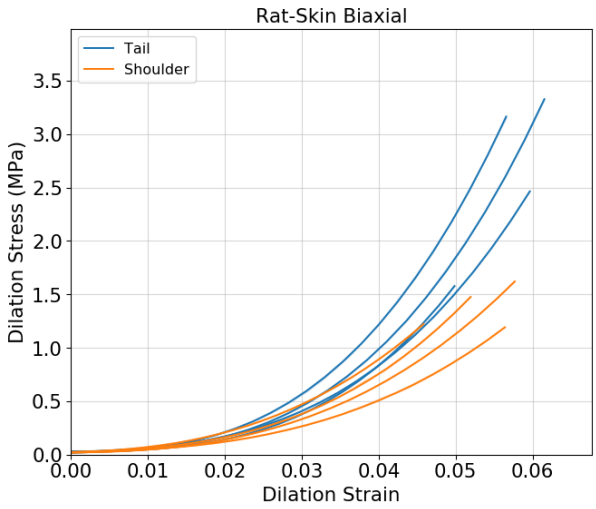

(a) Dilation conjugate stress strain pair from the equibiaxial tests

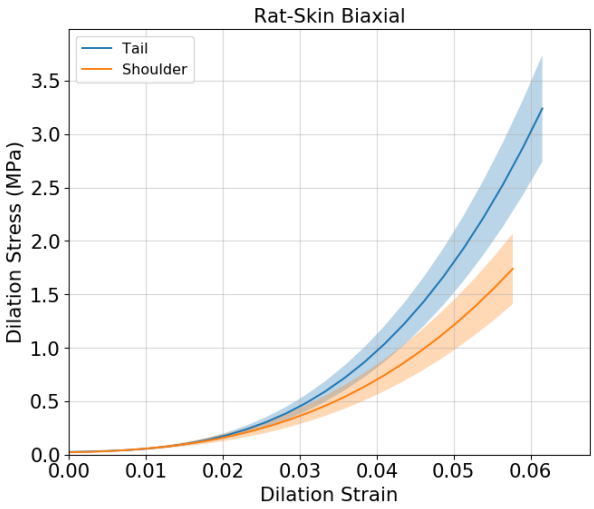

(b) Mean and standard deviations of the dilation curves from the equibiaxial tests

Figure 4.13: The dilation conjugate stress-strain pair for all 8 equibiaxial tests, grouped by whether they were harvested from near the shoulder (Top) or the tail (Bottom)

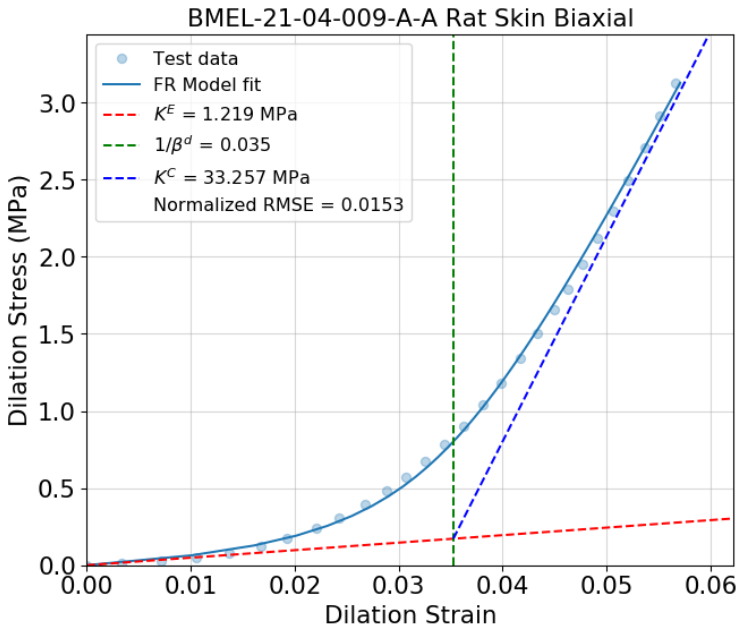

Figure 4.14: The Freed-Rajagopal model used to fit the dilation stress-strain conjugate obtained from an equibiaxial test

The three parameters were thus fit for all the samples tested and the results are shown in Table 4.1.

Test group	**Count**	K^E **(Mpa)**	$\mathbf{1/\beta^d}$	K^C **(MPa)**	**NRMSE**
All samples	8	0.898 ± 0.175	0.0337 ± 0.0028	20.586 ± 6.615	0.0135 ± 0.0020
Shoulder region	4	0.827 ± 0.248	0.0323 ± 0.0062	14.289 ± 2.813	0.0121 ± 0.0045
Tail region	4	0.968 ± 0.405	0.0351 ± 0.0038	26.784 ± 10.129	0.0148 ± 0.0017

Table 4.1: The mean low-stress modulus K^E, terminating modulus K^C, and transition strain $1/\beta^d$ for dilation obtained from the equibiaxial tests on rat skin, and their 95% confidence intervals

For completeness, the load vs stretch data for all the samples in the two directions is shown in Figure 3.11. Load values are obtained directly from the load cells, and the stretch values are obtained from DIC analysis (as shown in Figure 4.11b). The loads seem to be consistently higher in the Medial-Lateral direction.

4.3.2 Uniaxial tests (Squeeze)

Figure 4.16 shows the histogram and strain distribution at the end of the uniaxial test on a rat skin sample. The squeeze and dilation distributions looks reasonably uniform, with a little bit of spread in the shear response. It can be seen that the homogeneous region of strain extends almost all the way up to the clamps. The squeeze value is negative just because of the choice of axes, indicating that the stretch in the Y direction is larger than the contraction in the (transverse) X direction. The shear strain is centered around 0 indicating that the material did not tend to shear in a particular direction. As expected the squeeze is the largest mode of deformation. Interestingly however, the dilation is negative.

Figure 3.13a shows the the mean, median, mode, values of the 3 modes of deformation during the course of a uniaxial test. The distribution is reasonably tight over the entire course of the test for dilation and squeeze, while the shear strain distribution seems to spread out at larger

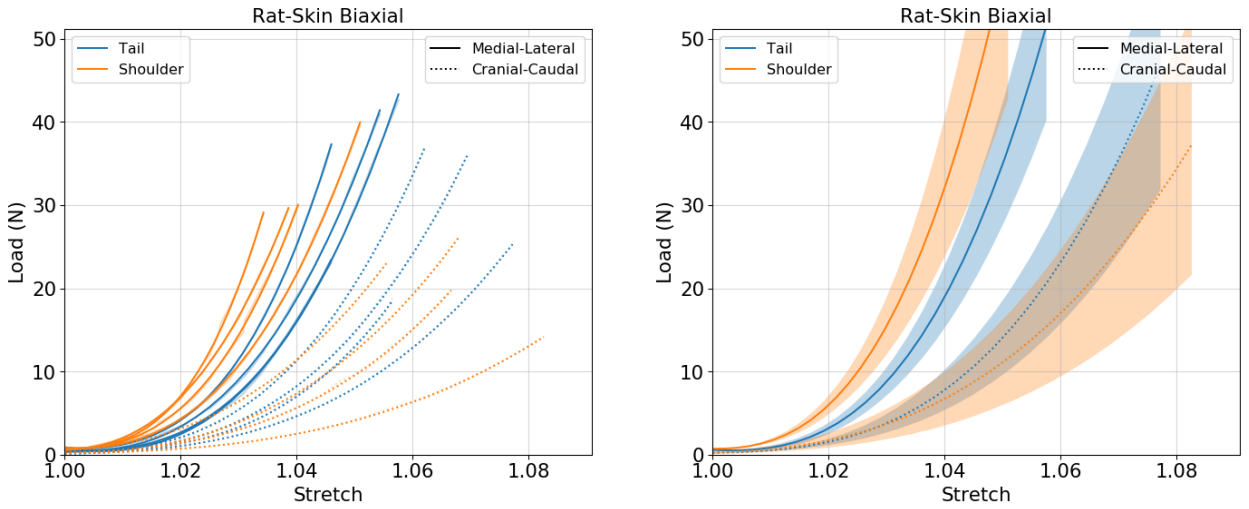

(a) Load vs Stretch for all the equibiaxial tests

(b) Mean and standard deviations of the load vs stretch curves from the equibiaxial tests

Figure 4.15: Load vs Stretch for all the equibiaxial tests, grouped by whether they were harvested from near the shoulder or the tail

strains.

Figure 3.13b shows the two stretches a and b, obtained from the Laplace stretch $\mathscr{U}$. The distribution is quite tight throughout the test. b is in the direction of the applied displacement (Y axis) while a is in the transverse direction, caused by Poisson's effect. Here also, counter-intuitively the transverse contraction seems larger that the stretch applied in the test direction.

Figure 4.18 shows the mean values (over the test surface) of the strain modes through the uniaxial test for all 16 samples tested. For better clarity, the squeeze strains have been multiplied by -1. The results are quite spread out over the entire plot area. There is a general trend for the dilation to be negative, the shear to be close to 0, and the squeeze to increase linearly for all the samples.

The negative dilation value is seen in all of the uniaxial tests. Theoretically, this implies that there has been an areal contraction, but since it is a membrane and is not under any compressive forces, this is not possible. From Figure 4.17b, it is seen that the contraction in the transverse axis a grows faster than the applied stretch in the test axis b. Rather than assuming

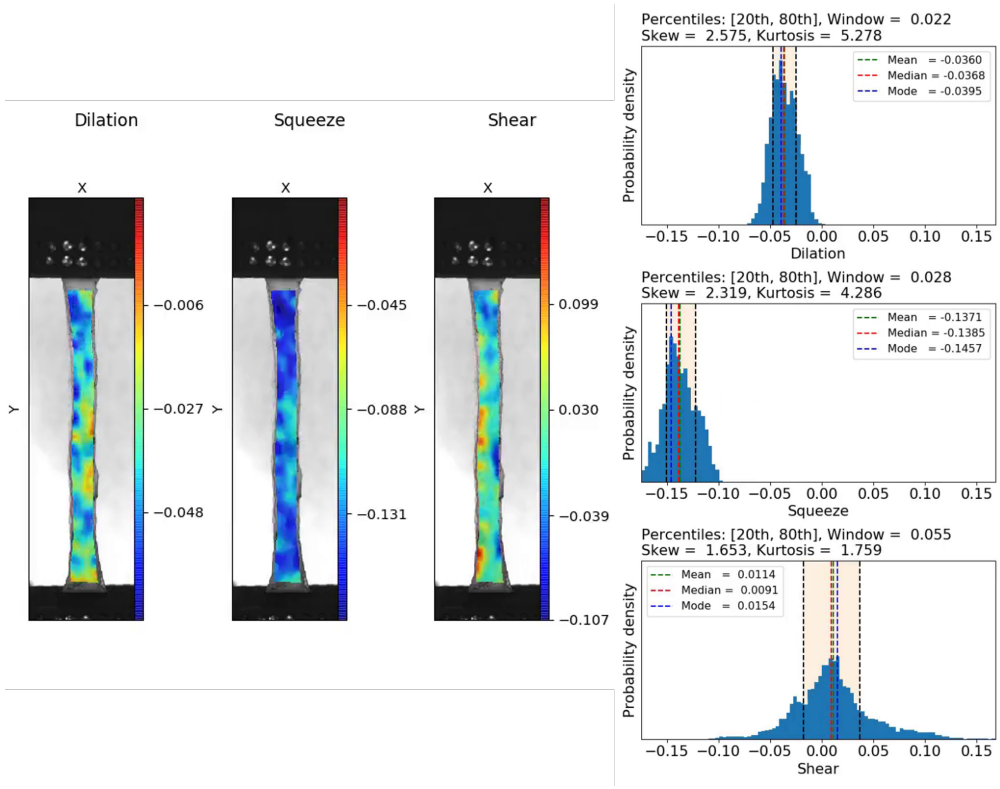

Figure 4.16: DIC analysis showing the distribution of the conjugate strain fields over the test region at the end of the uniaxial test. Histograms show the shape of the distribution for these strains

this is some atypical behaviour of the material, the most likely explanation is that the surface of the material is curling at the application of stretch. The 2D DIC analyis done here cannot different between contraction and an out of plane bending, and is thus interpreted as a 'super contraction'. The stretch a is then likely convoluted as a result of experimental shortcoming.

Using the encoding algorithm described in the Methods section, the squeeze stresses were calculated (Figure 4.19). The curves are quite spread apart, although the ML curves seem to have lower terminal moduli in general. The 95% confidence interval curves suggest the same, but no statistical analysis was done to verify if this was significant.

The Freed-Rajagopal model was fit to all these curves graphically as described in section 4.2.2.2. An example plot from two of these tests, one from each direction, is shown in Figure 4.20. The model curve shows excellent fit with the test data, with a normalized root mean

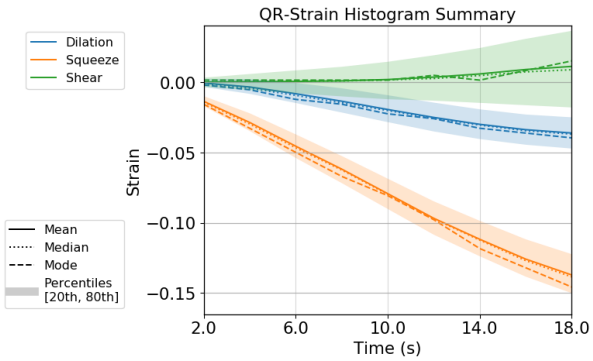

(a) The three modes of deformation over the test period for a uniaxial test

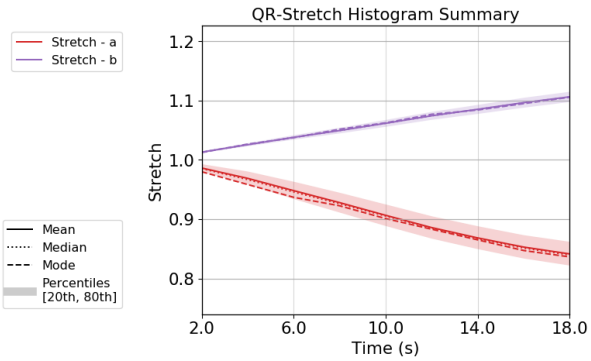

(b) The stretches in the two directions (a - X direction, b - Y direction) for a uniaxial test

Figure 4.17: The summary of the strains and stretches obtained through the QR decomposition of the deformation gradient F for a uniaxial test. Shaded regions represent the 20th to 80th percentile of the data points

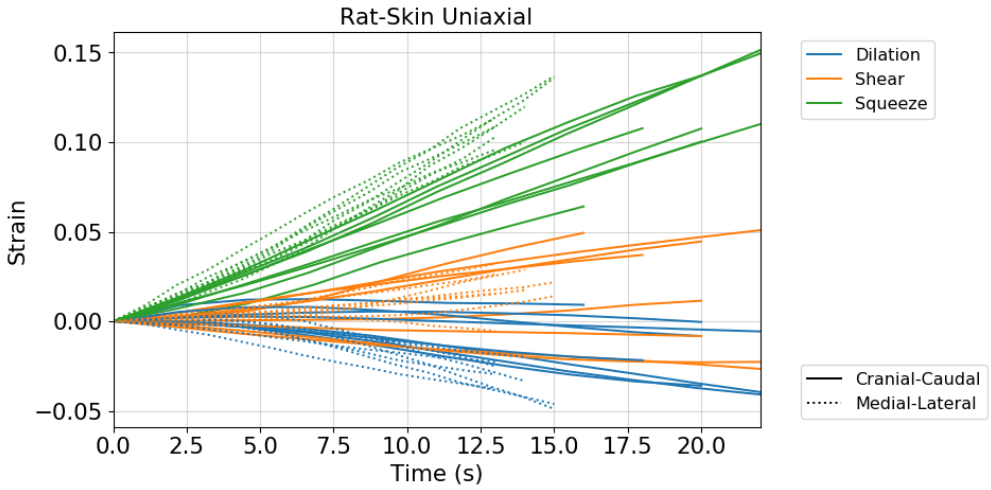

Figure 4.18: The three modes of deformation over the test period for the uniaxial test for all the samples

squared error (NRMSE) of 0.0161 and 0.0178. The two directions have similar initial stiffnesses and transition strains, but have different terminal stiffnesses. The red dotted lines show the initial tangent slope, the blue dotted line show the final tangent slopes, and the green dotted lines show the transition strains. $E^E = 2M^E$, $E^C = 2M^C$, and $1/\beta = 1/\beta^q$ for M^E, M^C and β^q defined in Eq 4.3.

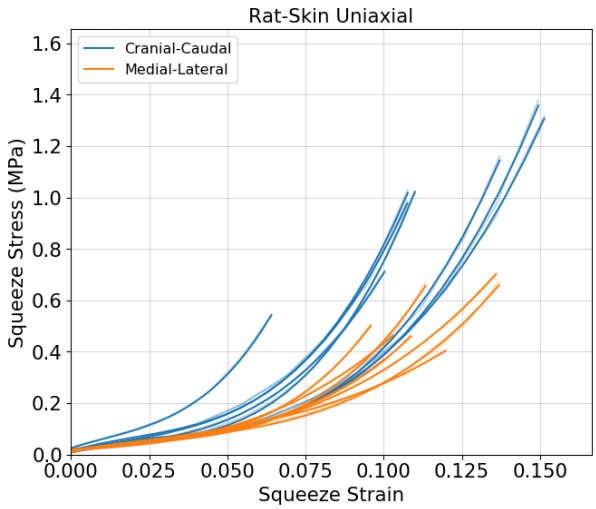

(a) The squeeze conjugate stress-strain pair for all the 16 uniaxial tests

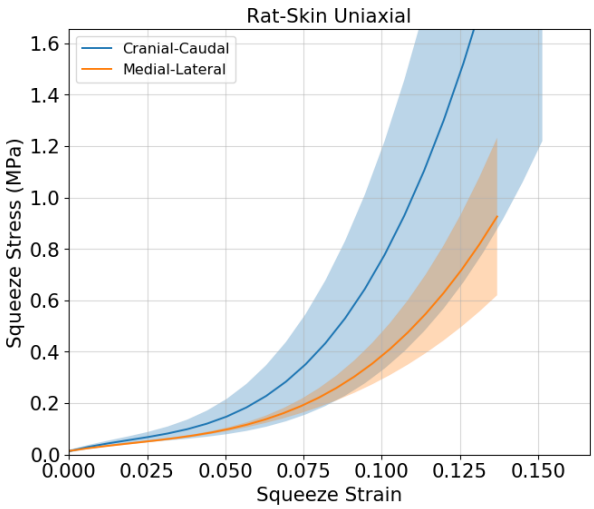

(b) Mean and standard deviations of the squeeze curves from the uniaxial tests

Figure 4.19: The squeeze conjugate stress-strain pair for all 16 uniaxial tests, grouped by their orientation *in-vivo*

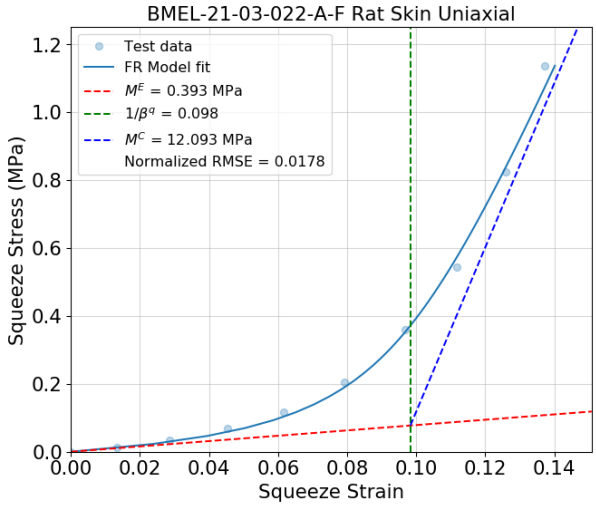

(a) FR fit in the Cranial-Caudal direction

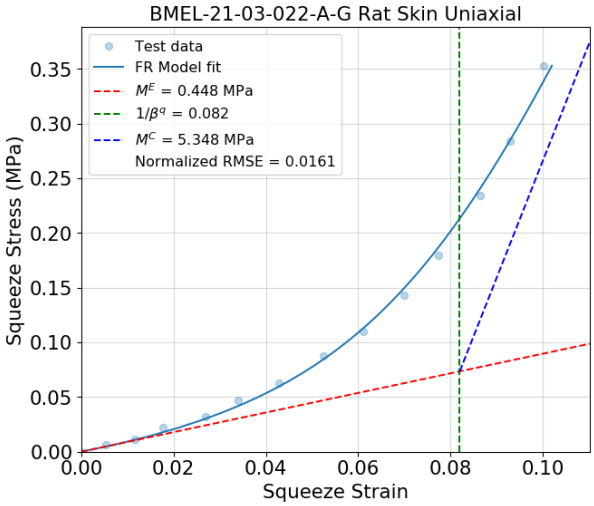

(b) FR fit in the Medial-Lateral direction

Figure 4.20: The Freed-Rajagopal model used to fit the squeeze stress-strain conjugate curves obtained from uniaxial tests on rat skin in the CC and ML directions

The three parameters were thus fit for all the samples tested and the results are shown in Table 4.2.

Test group	Count	M^E (Mpa)	$1/\beta^q$	M^C (MPa)	NRMSE
All samples	16	0.533 ± 0.097	0.0868 ± 0.0084	9.575 ± 1.649	0.0166 ± 0.0045
Cranial-Caudal	8	0.603 ± 0.196	0.0832 ± 0.0161	12.142 ± 1.161	0.0158 ± 0.0089
Medial-Lateral	8	0.463 ± 0.056	0.0903 ± 0.0094	7.009 ± 1.571	0.0174 ± 0.0054

Table 4.2: The mean low-stress modulus M^E, terminating modulus M^C, and transition strain $1/\beta^q$ for squeeze obtained from the uniaxial tests on rat skin, and their 95% confidence intervals

For completeness, the load vs stretch data for all the samples is shown in Figure 4.21a and the standard deviations of the load stretch data is also shown (Figure 4.21b). Load values are obtained directly from the load cells, and the stretch values are obtained from DIC analysis (as shown in Figure 4.17b). The ML and CC curves appear to be almost coincident here.

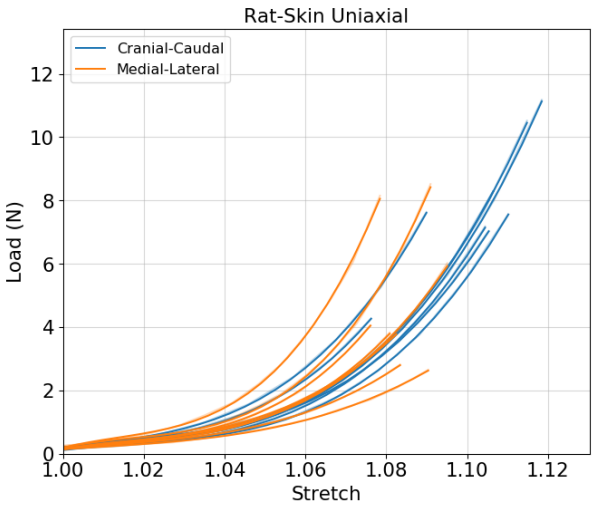

(a) Load vs Stretch for all the uniaxial tests

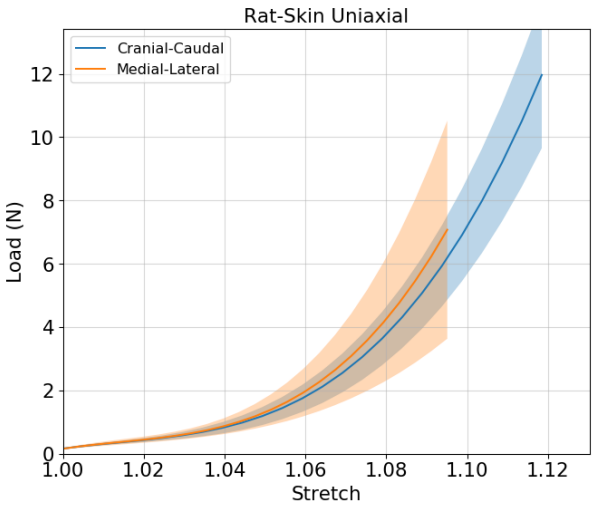

(b) Mean and standard deviations for the Load-Stretch curves for the uniaxial tests

Figure 4.21: Load vs Stretch plots show high degree of consistency between the samples for the uniaxial tests

4.3.3 Simple shear (Shear)

The simple shear experiment on rat skin was already described in Chapter 2 and a thorough analysis of the Green strain and Kirchoff stress was done. Here, the same dataset is used to

instead calculate the conjugate stress strain pairs.

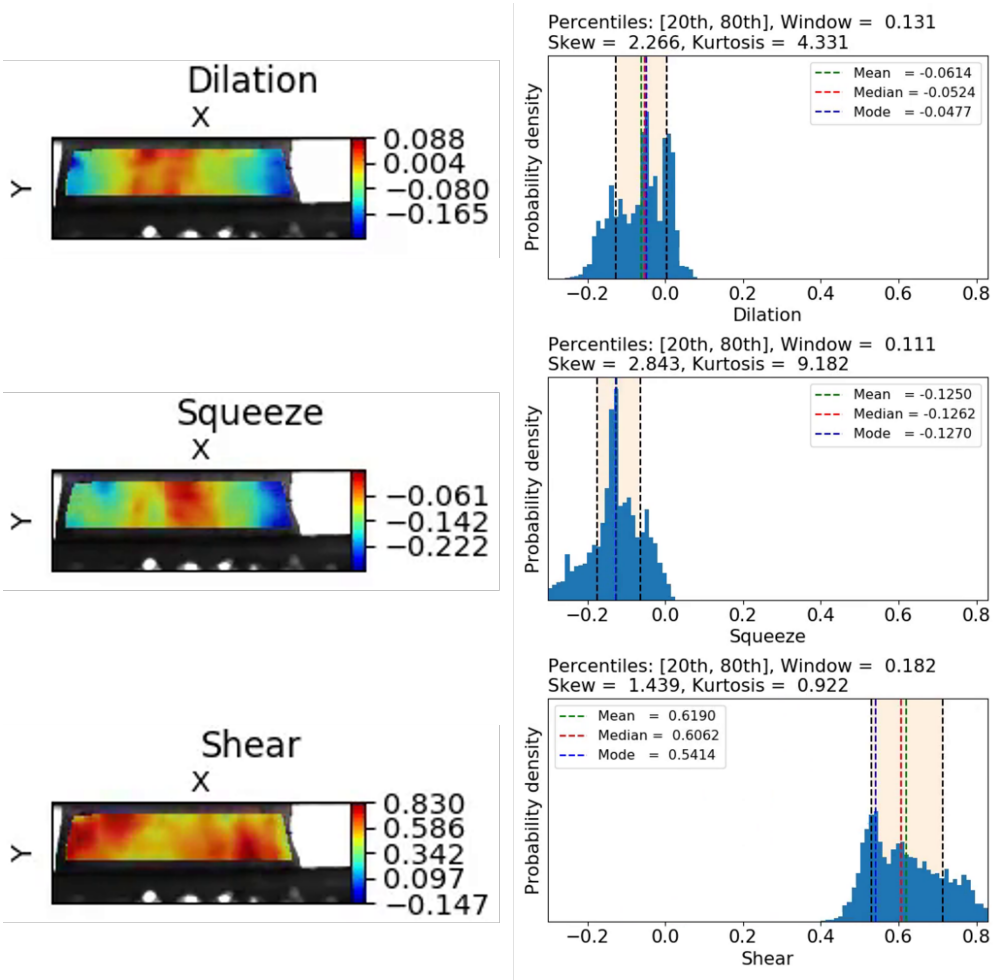

Figure 4.22: DIC analysis showing the distribution of the conjugate strain fields over the test region at the end of the simple shear test. Histograms show the shape of the distribution for these strains

Figure 4.22 shows the histogram and strain distribution at the end of the simple shear test on a silicone sample. The distribution is spread out in all three modes, but the shear and squeeze more have a unimodal appearance. The dilation and squeeze deformations are from the pre-stretch phase, while the shear is from the shearing phase (Figure 4.23a).

Figure 4.23a shows the the mean, median, mode, values of the 3 modes of deformation during the course of a simple shear test. The distribution is reasonably tight over the entire course

of the test for all three modes. The squeeze deformation increases during prestretch, while the shear and dilation remain close to 0. After that, the shear increases linearly while the dilation and squeeze remain constant, with a slight decrease in dilation at higher strains. This is especially clear in Figure 4.23b, where the strain values are offset by their values at the beginning of the shear phase (these are also the average values of the strains from the top and bottom halves of the double lap shear test). As in the uniaxial test, a negative dilation is seen here too, indicating possible out of plane deformations.

Figure 4.23c shows the two stretches a and b, obtained from the Laplace stretch $\mathscr{U}$. b is in the direction of the applied displacement during prestretch (Y axis) while a is in the transverse direction, caused by Poisson's effect. As b increases during prestretch, a decreases due to Poisson's effect. This is especially clear here compared to the silicone in Chapter 3, where a remained relatively close to 1 throughout. This is possibly because of the large aspect ratio used for silicone, compared to the rat skin test studied here. a also seems to have large distribution, indicating a heterogenous field. b decreases throughout the shearing phase, where ideally it should have remained constant throughout.

Figure 4.24 shows the mean values (over the test surface) of the strain modes through the shearing phase of the simple shear test for all 8 samples tested. Both squeeze and dilation are quite constant over the shear phase, (clear from Figure 4.24b), with dilation dipping below 0 towards the end.The slightly different amounts of dilation and squeeze are produced during the prestretch phase, but in all cases they remain constant during the shearing phase. No obvious differences are seen between the shearing in the CC vs the ML direction.

Using the encoding algorithm described in the Methods section, the shear stresses were calculated as well (Figure 4.25). Note that the stretches a and b were offset by their values at the beginning of the shear phase. The samples in general have a low moduli at lower stresses, that increases at higher stresses, although the transition is not dramatic.

The Freed-Rajagopal model was fit to all these curves graphically as described in section 4.2.2.2. An example plot from two of these tests, one from each direction, is shown in Fig-

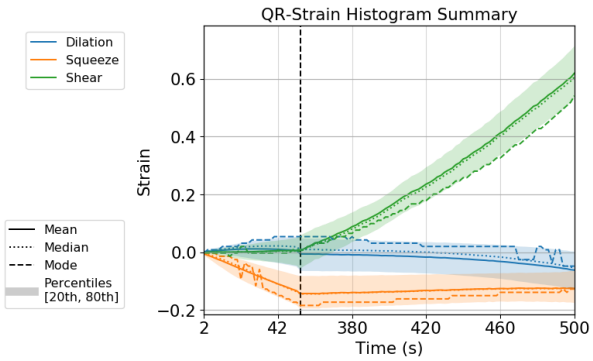

(a) The three modes of deformation over the test period for a simple shear test

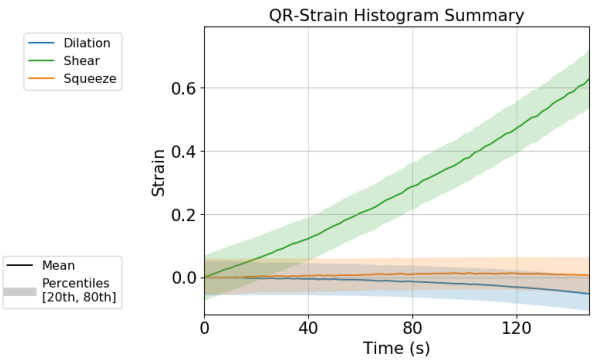

(b) The three modes of deformation over the test period for a simple shear test, offset by their values at the beginning of the shear phase

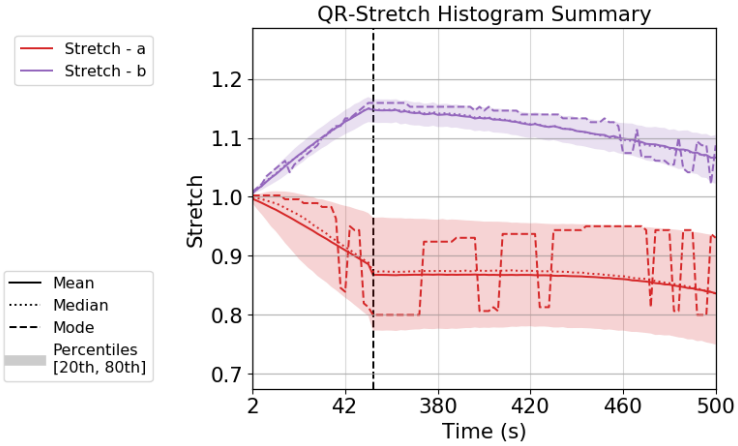

(c) The stretches in the two directions (a - X direction, b - Y direction) for a simple shear test

Figure 4.23: The summary of the strains and stretches obtained through the QR decomposition of the deformation gradient F for a simple shear test. Shaded regions represent the 20th to 80th percentile of the data points

ure 4.26. The model curve shows excellent fit with the test data, with a normalized root mean squared error (NRMSE) of 0.0467 and 0.0312. The red dotted lines show the initial tangent slope, the blue dotted line show the final tangent slopes, and the green dotted lines show the transition strains. $E^E = G^E$, $E^C = G^C$, and $1/\beta = 1/\beta^s$ for G^E, G^C and β^s defined in Eq 4.4.

The three parameters were thus fit for all the samples tested and the results are shown in Table 4.3. The range next to the values is the 95% confidence intervals using t-distribution.

For completeness, the load vs shear strain (γ) data for all the samples is shown in Figure 4.27.

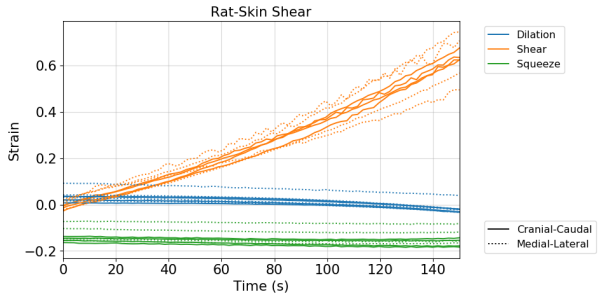

(a) The three modes of deformation in the simple shear test for all the samples

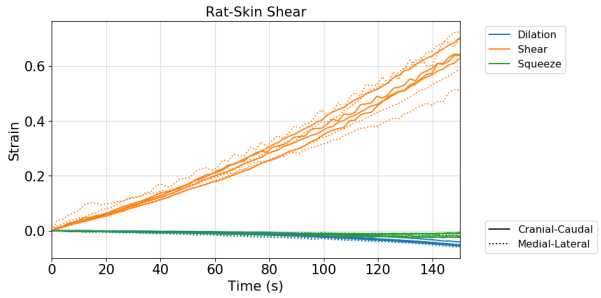

(b) The three modes of deformation in the simple shear test for all the samples, offset by their values at the beginning of the shear phase

Figure 4.24: The three different prestretches applied are denoted by the three different line types. Only the data points after the beginning of the shear phase are shown here

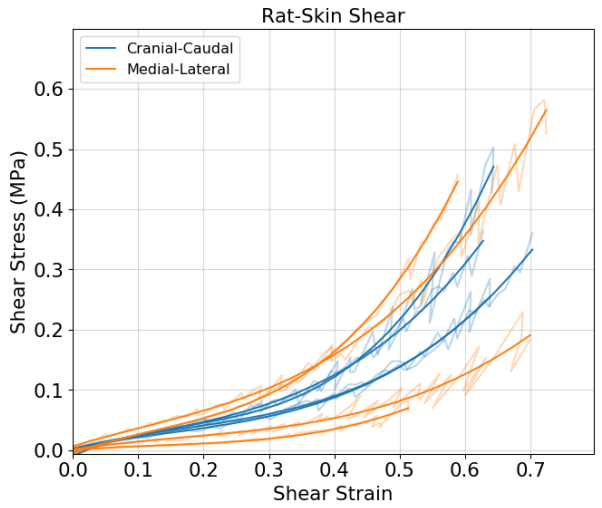

(a) The shear conjugate stress-strain pair for all the 8 simple shear tests

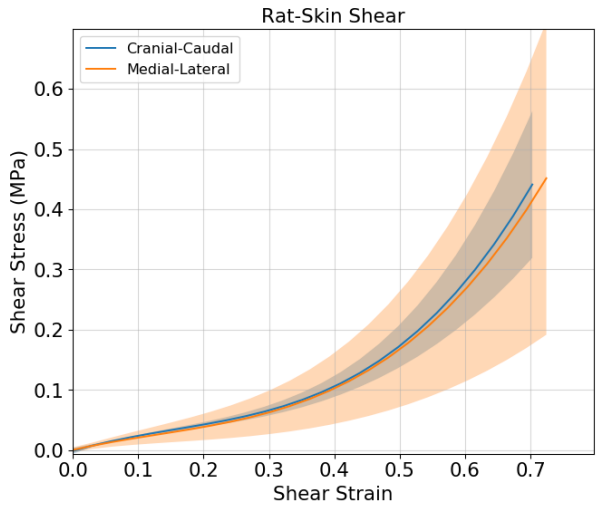

(b) The mean and standard deviations for shear conjugate stress-strain pair for the simple shear tests

Figure 4.25: The shear conjugate stress-strain pair for all the 8 simple shear tests. The translucent lines are actual test data and the solid lines are the filtered and smoothed curve.

Load values are obtained directly from the load cells, and the shear strain values are obtained from DIC analysis.

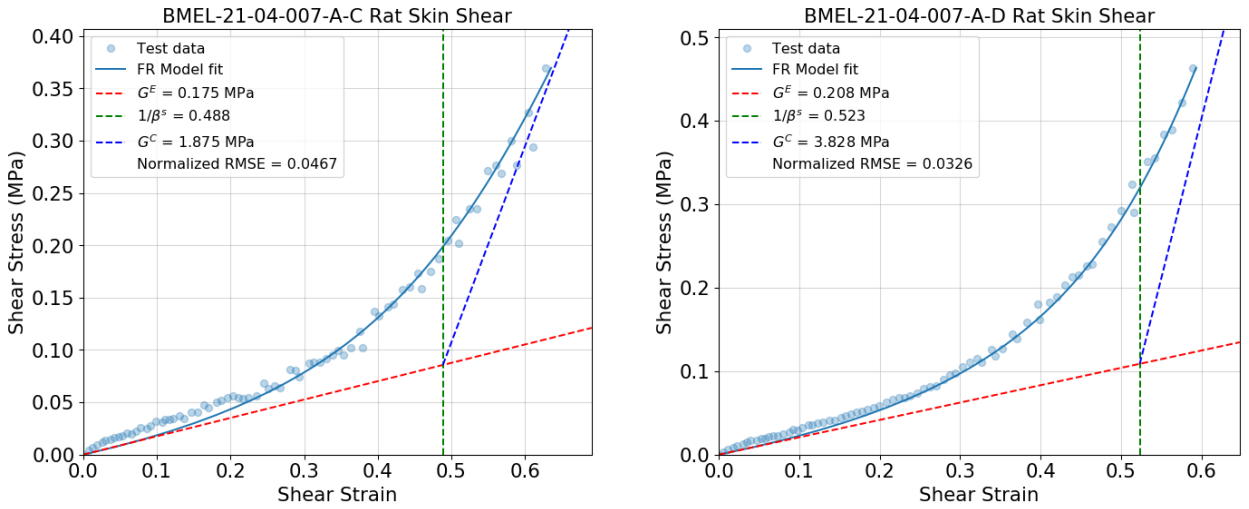

(a) FR fit in the Cranial-Caudal direction

(b) FR fit in the Medial-Lateral direction

Figure 4.26: The Freed-Rajagopal model used to fit the shear stress-strain conjugate curves obtained from simple shear tests on rat skin in the CC and ML directions

Test group	**Count**	G^E **(Mpa)**	$\mathbf{1/\beta^s}$	G^C **(MPa)**	**NRMSE**
All samples	8	0.144 ± 0.059	0.5367 ± 0.0501	2.164 ± 0.909	0.0468 ± 0.0095
Cranial-Caudal	4	0.147 ± 0.035	0.534 ± 0.0625	2.138 ± 1.103	0.0484 ± 0.0157
Medial-Lateral	4	0.142 ± 0.169	0.5393 ± 0.1314	2.190 ± 2.401	0.0453 ± 0.0225

Table 4.3: The mean low-stress modulus G^E, terminating modulus G^C, and transition strain $1/\beta^s$ for squeeze obtained from the uniaxial tests on rat skin. The range next to the values is the 95% confidence intervals using t-distribution.

4.3.4 Inhomogeneity of strain field distribution

The normalized inhomogeneity of the strain fields were calculated for the three modes for all the tests, and the mean values and the standard deviations for the final frame in each test are shown in Table 4.4. Additionally, the mean and standard deviation of $max(\overline{'Test-type' \; strain})$ and the Variation Ranges for each test type (over all the tests) is shown for context.

The strain distributions are more spread out than for silicone, as is to be expected. In the uniaxial and equibiaxial tests, the shear mode had the largest spread.

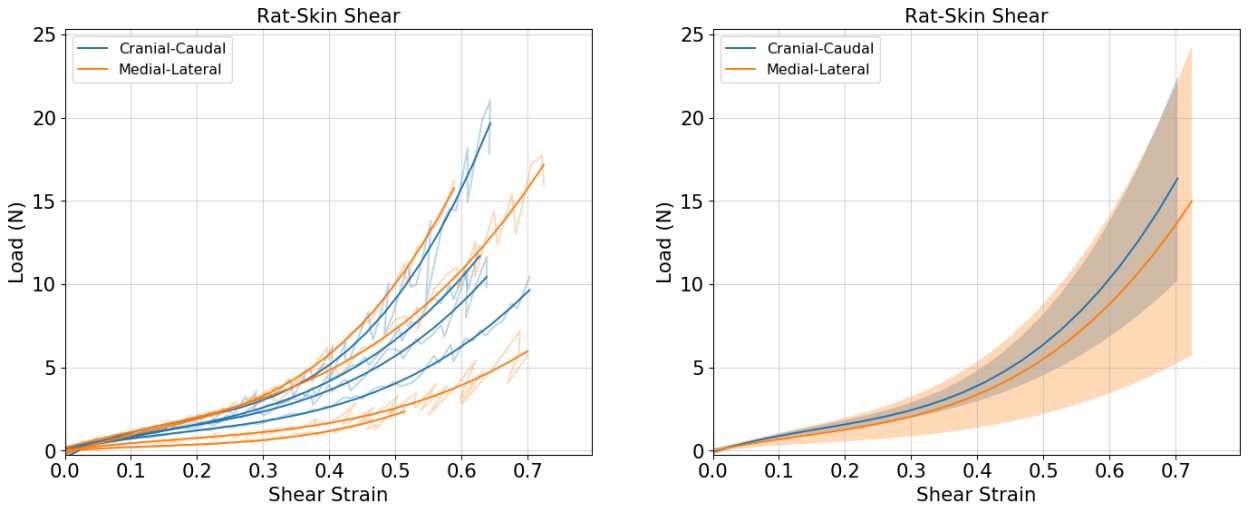

(a) Load vs Shear for all the simple shear tests

(b) Mean and standard deviations for Load vs Shear for all the simple shear tests

Figure 4.27: Load vs Shear for all the simple shear tests grouped by physiological direction

Test type	**max('Test-type' strain)**	**Strain**	**Variation Range**	**Normalized Inhomogeneity**
Equibiaxial extension (n = 8)	(Dilation) 0.0549± 0.0053	Dilation	0.0072 ± 0.0026	0.132 ± 0.047
		Squeeze	0.0128 ± 0.0052	0.236 ± 0.098
		Shear	0.0256 ± 0.0081	0.473 ± 0.163
Uniaxial extension (n = 16	(Squeeze) 0.1151 ± 0.0226	Dilation	0.0269 ± 0.0078	0.251 ± 0.128
		Squeeze	0.0343 ± 0.0078	0.319 ± 0.144
		Shear	0.0692 ± 0.0171	0.637 ± 0.263
Simple Shear (n = 8)	(Shear) 0.6339 ± 0.0786	Dilation	0.1105 ± 0.0325	0.174 ± 0.045
		Squeeze	0.1261 ± 0.0248	0.200 ± 0.039
		Shear	0.2340 ± 0.0568	0.369 ± 0.077

Table 4.4: Normalized inhomogeneity of the strain modes at the final frame of the tests.All values are mean ± standard deviation

4.4 Discussion

The Freed-Rajagopal model for planar membranes achieved a great fit across all the test types and on all samples, further emphasising it's utility for modeling biological tissues. For the squeeze and dilation curves, the NRMSE values were consistenly in the range of less than

0.015 (Tables 4.1, 4.2) and less than 0.05 for shear (Table 4.3), but there the test data was much noisier. Further, fitting the model to the data is quite intuitive, easy, and foolproof. The initial and final tangent slopes are easily obtained, along with their intersection to get the initial guess for the transition strain. Once this initial guess was obtained, it was a trivial matter to tweak the 3 parameters slightly to get the best fit.

The three parameters also give great insight into different aspects of the material behavior. Across all three tests and the respective conjugate stress-strain pair, the transition strains observed were remarkably consistent, even across the different directions and sample locations. The initial moduli differed slightly but was still comparable, while the great difference across different directions came in the terminal moduli. This may provide valuable insight into the actual physical phenomenon that cause certain aspects of the material behavior, including anisotropy. For example, in the equibiaxial tests, between the samples harvested near the shoulder vs the tail, neither K^E nor β^d were statistically significantly different, with p-values of more than 0.95 (2 tailed student's t-test). However the terminal modulus K^C was statistically different at 95% signficance with a p-value of <0.05. Similarly from the uniaxial tests, between the CC and ML direction samples, neither M^E nor β^q were statistically significantly different, with p-values of more than 0.95 (2 tailed student's t-test). However the terminal modulus M^C was statistically different at 95% signficance with a p-value of <0.0005 (Figure 4.28. These results impart physical intuition to these material parameters, and how different aspects of the material behaviour are drivers of heterogeneity or anisotropy.

The QR decomposition of the deformation gradient F gives rise to very experimentally friendly, scalar pairs of conjugate stresses and strains. These are significantly easier to understand intuitively as well as calculate in an experiment.

The method of drawing the sample shape on the rat prior to excision gave an idea of the kind of strains the material is under *in-vivo* compared to their relaxed states after excision that are used as their reference configuration. Over all the 32 samples harvested across 4 rats, the samples contracted with a mean stretch of 0.89 along the Cranial-Caudal direction and 0.86

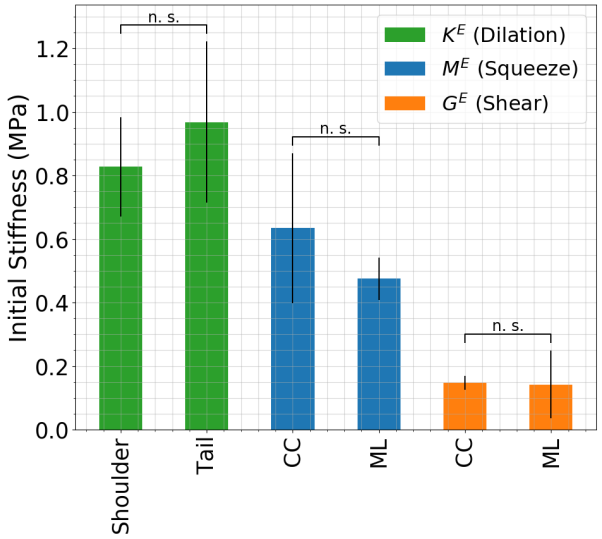

(a) Initial Stiffness

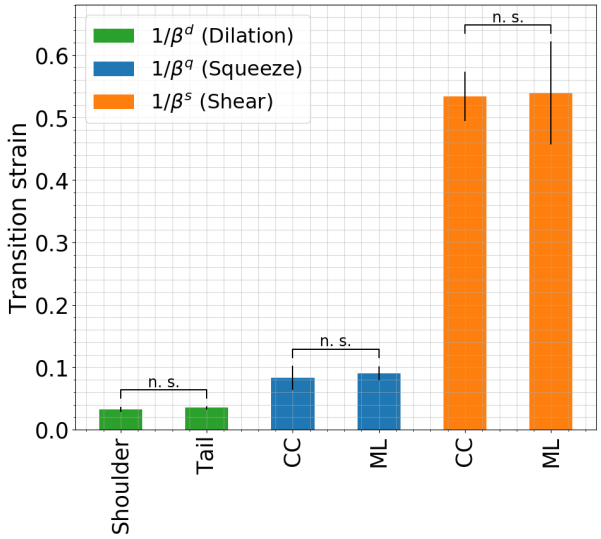

(b) Transition strain

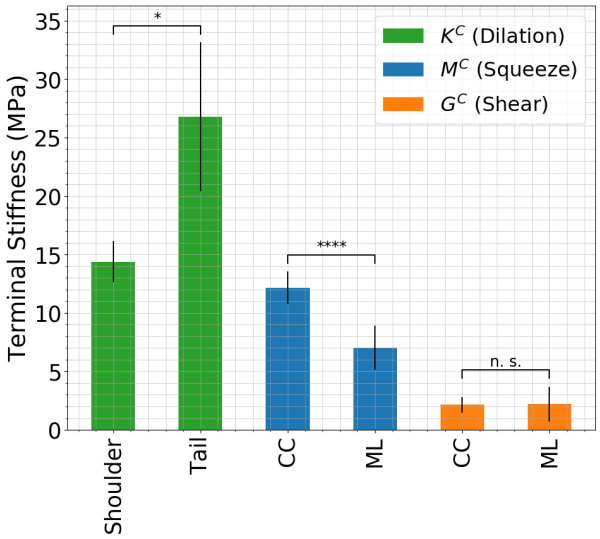

(c) Terminal Stiffness

Figure 4.28: Mean and standard deviation of the model parameters for the three modes. * indicates $p < 0.05$, **** indicates $p < 0.00005$, and n.s indicates no statistical significance for a student's t-test with a 95% significance value

along the Medial-Lateral direction. This information may be useful in recreating the residual stress in-vivo in experimental settings to improve modeling efforts.

The suture placement jig (Figure 4.4) allowed for consistent placement of sutures across all the samples, which has traditionally been quite difficult for biological tissues.

A comprehensive set of experimental data is available for further study. Tests have been

done in 3 different modes of deformation and at different locations across the body to get a sense of heterogeneity. Other researchers wanting to validate other theoretical frameworks and constituve models may potentially be able to use this data.

4.4.1 Limitations and future work

Biological tissues are viscoelastic, heterogeneous, and anisotropic. While the materials were tested in 2 different orientations and from different locations in the body, a concerted effort to quantify heterogeneity and anisotropy has not been made. The FR model has been extended to include viscoelasticty [27], and the QR decomposition to incorporate material anisotropy [28]. These can be incorporated into the modeling of this dataset to get a better picture of the material properties.

Even though all the tests were completed on the same day of excision and were kept moist with isotonic Phosphate Buffered Saline (PBS), the tests were all conducted at room temperature in ambient humidity. This may significantly affect the material properties of the tissues.

The parameters obtained for the material properties have not been used in a comprehensive modeling capacity, such as in a finite element simulation, to validate their utility in predicting material behavior. Doing this, along with a comparison of other constitutive models to describe the comprehensive set of data available here, would significantly improve the impact of this work.

The negative dilation seen in the uniaxial tension tests significantly affect the material parameters obtained here. A limitation of this framework is that even the uniaxial test has to be analysed in 2D and thus needs to have been experimental control. A stereo DIC technique might be useful in quantifying the out-of-plane curling and potentially get the true stretches on the surface, for better use of this framework.

Finally, this framework is meant for a 2D analysis of an inherently 3D material, and is so handicapped by default. Development of this framework to 3D is underway and should provide a more comprehensive description of material properties.

4.5 Conclusion

A comprehensive set of uniaxial, equibiaxial, and simple shear experiments were conducted on rat skin. The data was analysed using the QR decomposition of the deformation gradient and the conjugate stress-strain pairs of dilation, squeeze, and shear were obtained for rat skin. The Freed-Rajagopal implicit elastic constitutive model was used to obtain 3 material parameters for each mode of deformation, and their 95% confidence intervals were calculated. The FR model showed a consistently excellent fit to test data across all samples and tests. Techniques to capture *in-vivo* residual stresses in experiments and to improve the consistency of applying sutures in a biaxial tension tests were also detailed. The FR model used in conjunction with the QR decomposition of F shows great promise in capturing material behaviour with physically intuitive parameters that may significantly benefit tissue engineers in search of developing mechanically biomimetic tissues.

5.1 Background

With a better understanding and characterization of the mechanical properties of biological tissues, the tissue engineer is now faced with the problem of identifying how these mechaical environments affect cell behavior and tissue growth. There are an infinitely complex array of factors influencing the success of tissue engineered technologies, but a few have been identified as major players, including biochemical cues such as pH, osmolarity, environmental cues such as temperature, humidity, CO_2 concentration, notwithstanding the countless nutrients and enzymes specific to different cell types. Mechanical loads and deformations have also been identified as a significant contributor in the functioning of certain cell types. It is well known that some cell types respond to the mechanical cues applied to them biochemically. Consequently, many bioreactor designs can be found in literature that apply a variety of mechanical loads to cell seeded scaffolds [13]. The previous chapters looked at a novel theoretical framework that is conducive to tissue engineering approaches requiring biomimmicry. If these prove to be helpful in the design and manufacture of tissues where the mechanical properties can be tuned, the question then becomes, which aspects of the mechanical environment are critical for any particular therapeutic application. The requirements could be anywhere from inducing pluropotent stem cells to differentiate into the appropriate cell type in the engineered scaffold through the application of mechanical forces, to developing constructs that are mechanically biomimmetic to the tissue they are replacing, so that the cells will incorporate into the construct naturally *in-vivo*

For tissue engineering applications, a bioreactor is commonly used to study the response of biological cells to complex environmental cues. In this work, a bioreactor capable of applying an arbitrary displacement profile (possibly physiologic) in uniaxial tension is developed. Biocompatibility assays are done to validate the use of the bioreactor for cell culture studies, and

the bioreactor is validated by performing relatively long term cyclic stretch to biological cells.

5.2 Bioreactor construction

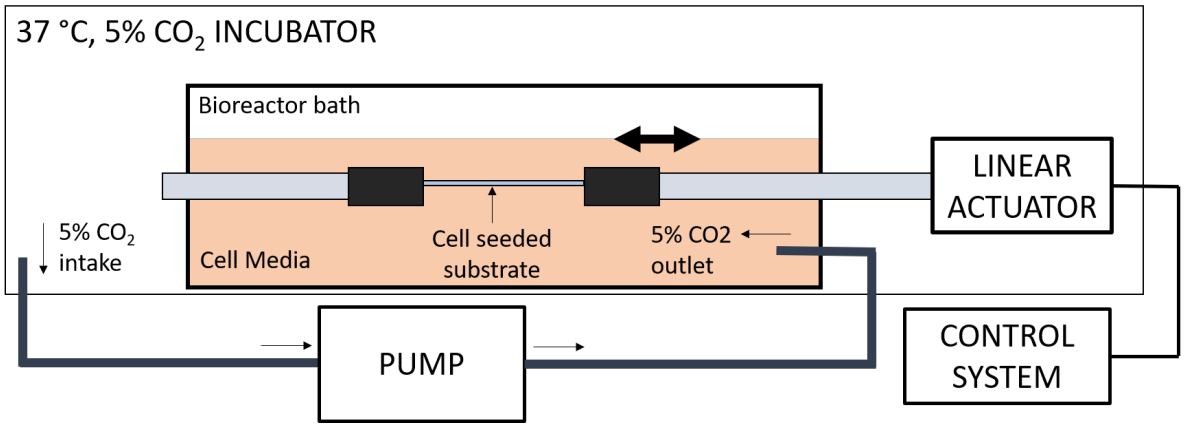

Figure 5.1: Schematic of the uniaxial bioreactor with linear actuator and media circulation system.

Figure 5.1 shows the general schematic of the bioreactor. The bath is machined out of Nylon 6,6 and sealed with a polycarbonate lid and a USP Class VI silicone o-ring. Rods and clamps made out of 316L stainless steel are used to clamp the cell seeded substrate. One end of the substrate is fixed while the other end is attached to a linear actuator (Haydon Kerk Pittman Captive Linear actuator). The sample is submerged in cell media and entire setup is mounted on a breadboard and placed inside an incubator at 37°C and 5% CO_2. Air from inside the incubator is pumped into the bioreactor to maintain the correct gas concentrations in the media. The linear actuator is connected to the control system (National Instruments cRIO) outside the incubator. Custom displacement profiles can be programmed through the control system using LabVIEW. A novel jig to ensure that the substrate is prestretched prior to seeding the cells, and then not disturbed mechanically in any way until loaded into the bioreactor was developed as well.

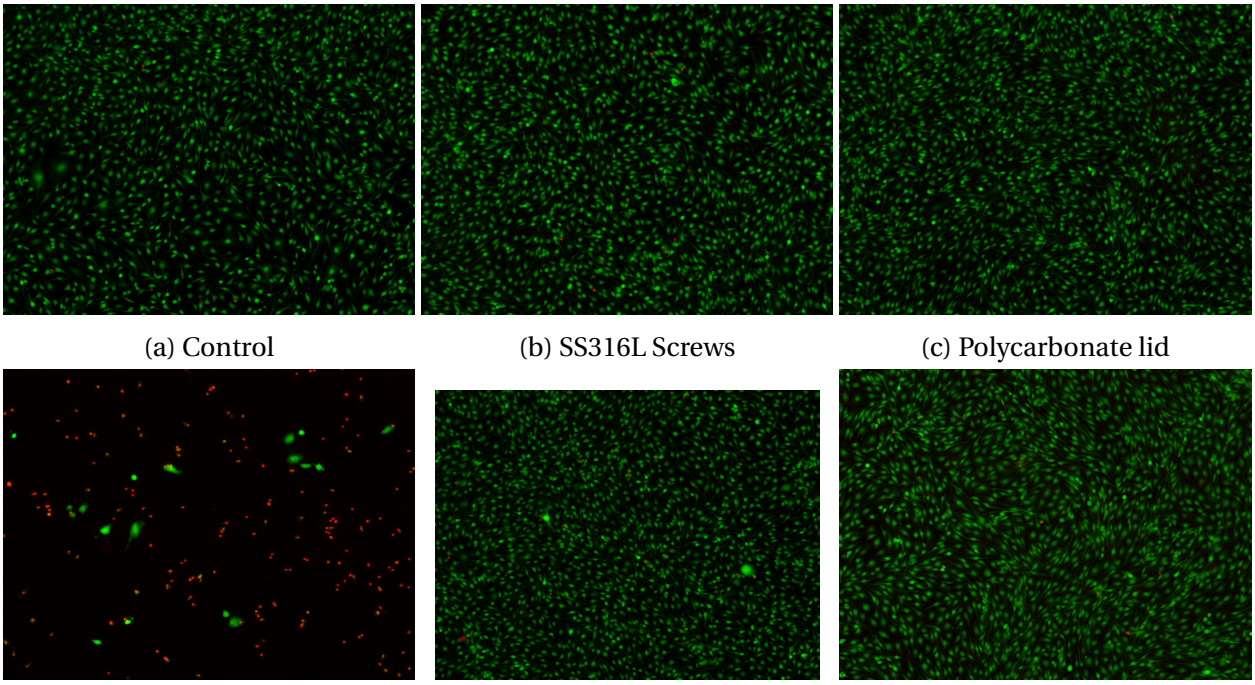

(a) Control (b) SS316L Screws (c) Polycarbonate lid

(d) Negative control (e) PTFE bearing (f) SS316L clamps

Figure 5.2: Live/dead assays from some of the biocompatibility tests. Green indicates live while red indicates dead cells

5.3 Biocompatibility testing

Biocompatibility tests were carried out for all the components coming in contact with the cells or cell media. ISO 10993-5:2009 (Biological evaluation of medical devices — Part 5: Tests for in vitro cytotoxicity) was used as a guide to design these tests. Standard 6-well plates were coated with 2% gelatin before sedding with around 75,000 NIH 3T3 fibroblasts per well. Simultaneously, samples of the materials being tested were put into a different 6-well plate and submerged with cell media. These were all incubated at 37°C and 5%CO_2 for 24 hours, at which time media was removed from the cell-seeded wells and replaced with the media conditioned by the sample being tested. After another 24 hours of incubation, live/dead assays were performed. In each 6-well plate, one of the wells was control (no sample was placed in the media), and another well served as negative control (a neodymium magnet was placed in the media). Samples from the rods, the clamps, the dowel pins used in the clamping, the urethane rod seals,

PTFE bearings, silicone o-rings, the poylcarbonate lid, the stainless steel tube fittings,etc were all tested for biocompatibility in this way, and their biocompatibility verified. Figure 5.2 contains live/dead assay images from a control, negative control, and a few of the results from the other materials as examples.

5.4 Proof-of-concept testing and results

5.4.1 Cyclical stretching study on NIH 3T3 fibroblasts

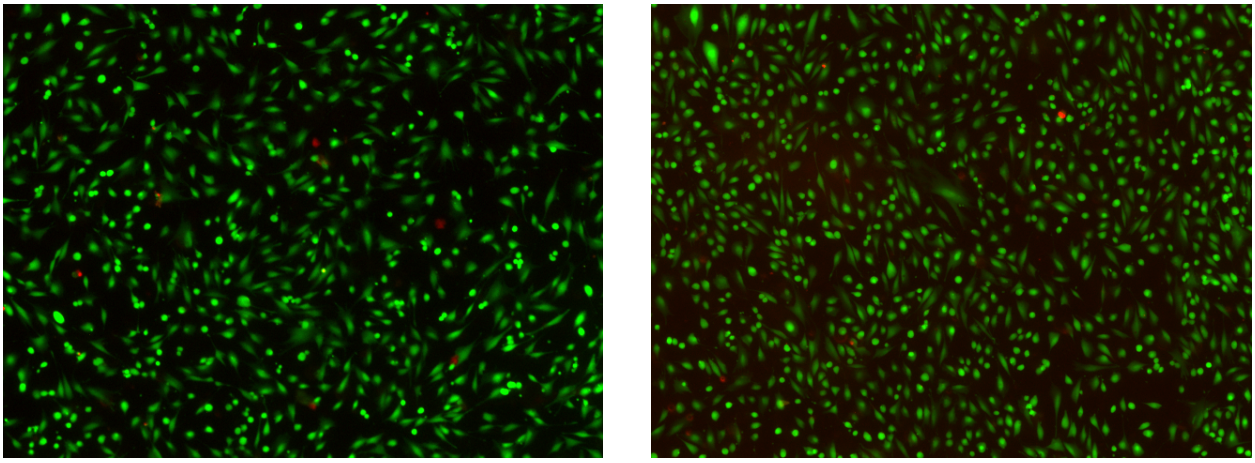

(a) Cells on control membrane

(b) Cells on membrane after stretching study

Figure 5.3: Live/Dead assay performed on 3T3 fibroblasts testing in the bioreactor. Green indicates live cells while red indicates dead cells.

NIH 3T3 fibroblasts were chosen for proof-of-concept testing due to their ease of culture and availability. 0.05" thick silicone sheets were manufactured using SYLGARD^{TM} 184 (Dow inc, MI, USA) and cut to strips of width 0.75". These were clamped at 2" gauge length, and then stretched to 2.1" prior to applying fibronectin in a 0.5"x0.5" square in the middle. Dulbecco's Modified Eagle Medium with 10% Fetal Bovine Serum and 1% antibiotic-antimycotic was used as culture media. 30,000 cells were seeded in this area and cultured under static conditions in the incubator for 10 hours. This was followed by a cyclical sinusoidal stretch of 5% amplitude (0.105") at 0.5Hz for 12 hours, followed by static culture for 5 hours. Control was cultured in

parallel in a silicone membrane placed inside a well in a 6-well plate for the entire duration of the study. Live/dead assay was performed on both the test and control specimens. As can be seen from Figure 5.3, the cells remained live after the stretching study in the bioreactor, and were comparable to the control in their cell viability.

5.4.2 Cyclical stretching studies on Human Dermal Lymphatic Endothelial Cells

The uniaxial bioreactor described here was used to study to the response of Human Dermal Lymphatic Endothelial Cells (HDLECs) to an applied large amplitude cyclical stretch. This study was part of a different project, but the results are presented here as further validation of the utility of the uniaxial bioreactor.

5.4.2.1 Methods

Three different stretching protocols were applied to the HDLECs. In all 3 experiments, initially HDLECs of passage less than 10 were seeded at 50,000cells/cm^2 on a 2.75in x 0.5in, 0.02in thick silicone membrane, in an area 0.5in x 0.5in in the middle. The membrane was mounted on to the bioreactor and filled with culture media (Endothelial Growth Medium-2 for Microvascular Cells EGM-2MV, Lonza, Basel, Switzerland) and the cells were statically cultured for 24 hours in a 5%C)^2 37 °C incubator to allow for cell attachment and proliferation.

The bioreactor control system was then used to initiate the cyclical stretching protocols. 3 different studies were done: 6 hours sinusoidal waveform, 12 hours sinusoidal waveform, and 6 hours physiological waveform. All tests were done at 0.3Hz to a strain amplitude of 40% on a gauge length of 2in. The physiological waveform was based on reported lymphatic vessel diameter measurements from Dixon, et al [29] (Figure 5.4b)

At the end of each stretching study, the membrane was removed and a Live/Dead assay was performed immediately (except for the 12 hour sinusoidal test, where phase contrast was used). Imaging was done to get the entire cell seeded area, and image analysis was performed to obtain the orientation of the cells. The distribution of alignments was measured in each case. In each of the experiments, a control membrane was simultaneously cultured at static conditions in

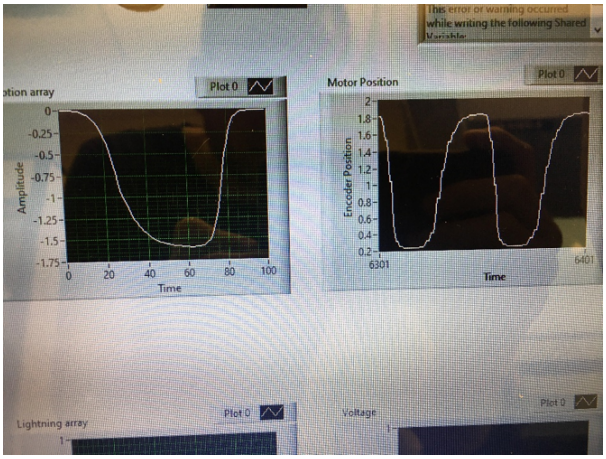

(a) Motion profile screen grab from bioreactor control system

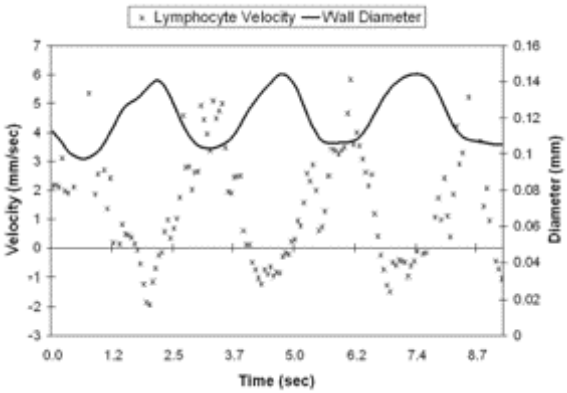

(b) Reported lymphatic vessel diameter measurements, reprinted from [29]

Figure 5.4: The physiological motion profile implemented on the bioreactor for the cyclical stretching studies on HDLECs

a 6-well plate for the same duration. Cell orientation analysis was performed on these as well, and a bootstrapped 2-sample 2-tailed Kolmogorov-Smirnov test with 10,000 samples of size 800 was performed to detect statistically significant differences between the distributions.

5.4.2.2 Results and discussion

In all three groups, cyclically-stretched cells were significantly more aligned than controls, which exhibited a more random distribution. The angle distribution in all cyclically stretched groups was centered approximately perpendicular to the direction of the stretching (direction of stretching was 0°/180°) demonstrating a bimodal angle distribution, with two peaks on either side of the perpendicular 90° angle (Figure 5.5.

While the motivation for this study is not discussed here, nor the significance of the results, it is nevertheless presented here to demonstrate the capability of the bioreactor described here. A reasonably long-term, cyclical stretching study of high strain amplitudes and physiologically relevant displacement waveforms was performed on HDLECs, a relatively more complex cell type than NIH 3T3 fibroblasts.

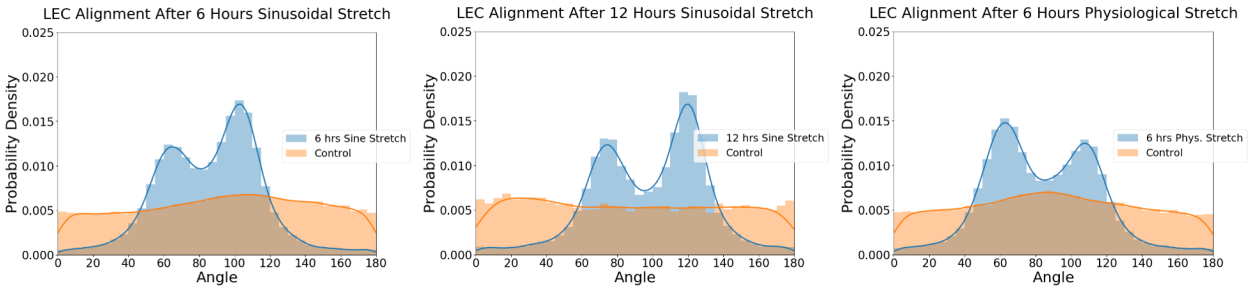

(a) Cell angle distribution for 6 hour sinusoidal stretch

(b) Cell angle distribution for 12 hour sinusoidal stretch

(c) Cell angle distribution for 6 hour physiological stretch

Figure 5.5: The normalized probability density function of the distribution of HDLEC alignment angles for the 3 cyclical stretching studies and the corresponding controls. In all tests, the test was significantly different from the controls at a 95% significance level ($p < 0.001$ for all three)

5.5 Discussion

The bioreactor has the capability of performing any custom waveform. As an example, the chordae tendineae was chosen for its predominantly 1D loading conditions *in vivo*. We consider the hypothetical situation where there is an engineered material that is said to "mimic" the chordae tendineae mechanically based on the Young's modulus calculated in the linear region. We consider the stress-strain curve of these two materials (Figure 5.6). As can be clearly seen, the material responses are different, and an applied load would produce different strains in the material. Cells seeded in these two materials would undergo an entirely different strain profile *in vivo* and this might affect whether they would respond favorably in a tissue engineering context.

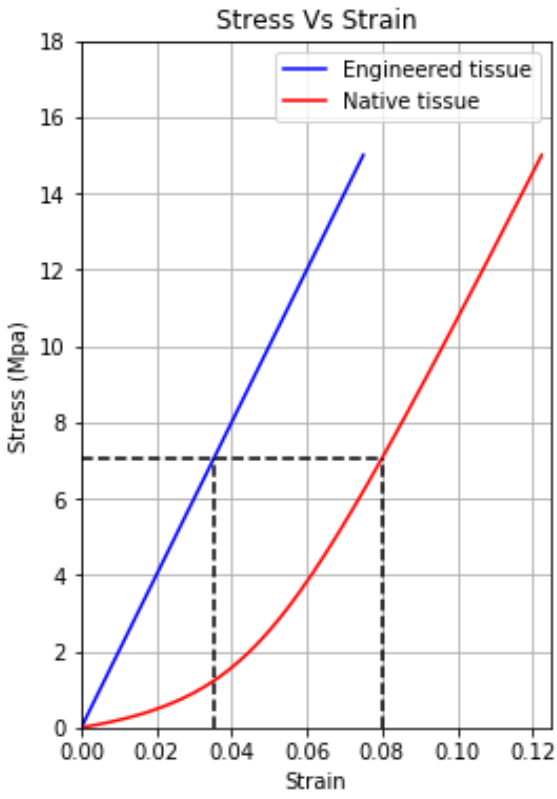

Figure 5.6: Stress-strain curves for chordae tendineae (labelled Native tissue) obtained from literature[30] compared to a hypothetical engineered material (labelled Engineered tissue) with a linear elastic response.

The loading profile of the chordae tendineae is chosen to approximately follow the Left Ventricular pressure. We then simulate the strain curves for these two materials under an applied cycling stress profile (Figure 5.7).

The LabVIEW user interface developed for this bioreactor allows the input of any arbitrary displacement profile. The two displacement profiles shown in Figure 5.7 were input into the system and it was verified that the bioreactor can produce these physiological profiles.

Jang et al[31] presented a composite material with a network structure that mimicked the strain limiting behavior of skin. Following their work, 10 mil mylar sheets were laser cut into the patterns described in [31]and encapsulated in SORTA-Clear^{TM} 40 (Smooth-On Inc.,PA, USA) silicone. The parameters used for the pattern were $R = 2mm$ and $w = 0.5mm$ (Figure 5.9b).

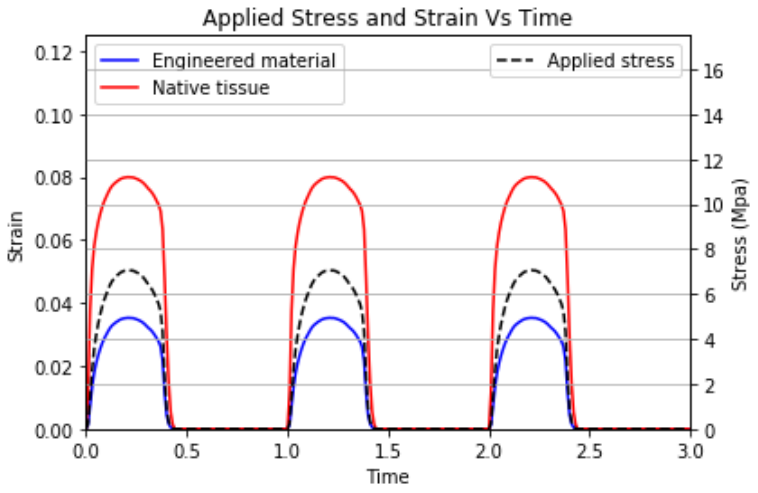

Figure 5.7: The strain profile calculate for an applied stress profile. Solid lines represent strain vs time, while dotted line represents stress vs time. Frequency chosen is 1Hz

Two different composites were made and uniaxially tested at 1% engineering strain per second, one with $\theta = 180°$ (0.031" thick, 2" gauge length and 1" width) and another with $\theta = 150°$ (0.036" thick, 2.75" gauge length and 1" width). By changing the amount of crimp in the Mylar network, the onset of the stiff region was delayed (Figure 5.9c).

The ability to tune different aspects of the mechanical behavior of these materials can be

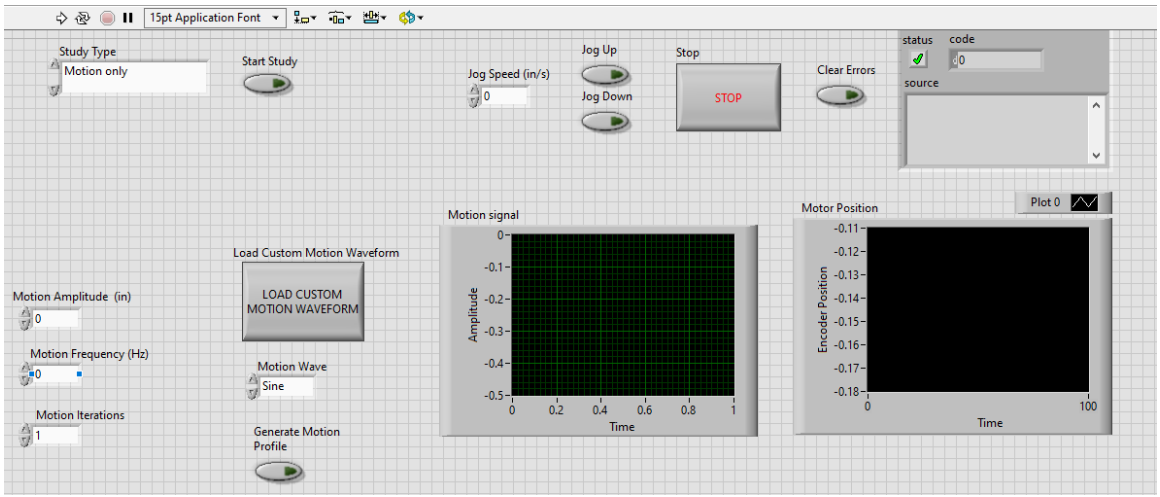

Figure 5.8: The user interface allows for sinusoidal displacement profiles as well as any arbitrary profile input through the "LOAD CUSTOM WAVEFORM" button.

(a) Laser cut mylar encapsulated in silicone

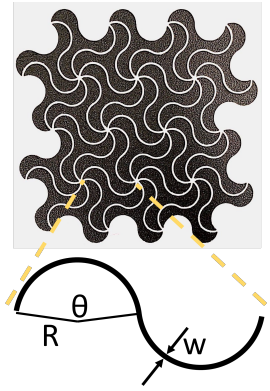

(b) R is the radius, θ is the included angle, and w is the width of strands

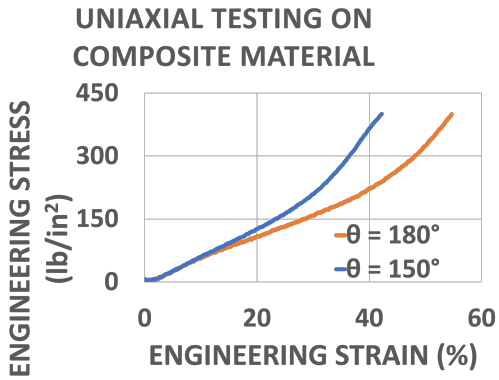

(c) Stress-strain curve from composites with two different internal angles

Figure 5.9: Mechanical testing of composites. A higher θ implies more crimp. It can be seen that the terminal stiffness did not change, but the heel region is delayed in the composite with the higher crimp

exploited in a bioreactor. These studies are examples of how the uniaxial bioreactor developed here could provide valuable information to tissue engineers about the mechanotransduction properties of different cell types and help isolate the mechanical factors that different cell types are most sensitive to.

5.6 Conclusion

A bioreactor capable of applying physiological uniaxial stretches was developed. The biocompatibility of all the components contacting the cells was verified with biocompatibility tests and the results were presented, NIH 3T3 fibroblasts were seeded on a silicone substrate and cyclically stretched inside the bioreactor to 5% engineering strain at 0.5Hz for 12 hours. A live/dead assay was performed to confirm that the cells remained viable through the course of the bioreactor study. The ability of the bioreactor to perform arbitrary physiologically relevant displacement profiles was demonstrated, and the potential uses in tissue engineering were discussed.

6. SUMMARY

The goal of the work described here was to investigate the utility of a novel theoretical framework that promised to provide physically intuitive parameters for mechanically characterizing biological tissues and engineered constructs, and developing a bioreactor capable of studying the sensitivity of cells to parameters obtained through this framework. The 4 specific aims listed for this work are repeated here, and the status of each is discussed.

Develop the ability to perform simple shear experiments on soft membranes *This aim will be considered complete when simple shear deformation is applied on 8 silicone membranes, the boundary loads are measured as defined in [19], and statistical analysis is performed on the uniformity of deformation.*

A novel apparatus has been developed that can apply shear deformations on soft membranes as well as measure the relevant boundary loads. 16 tests were performed on silicone membranes and 8 tests on rat skin, and the device was shown to be capable of applying uniform simple shear deformations. The boundary loads were measured, including the moments applied by the samples on the clamps, and the homogeneity of the strain fields developed were quantified and a statistical analysis was performed.

Perform dilation, squeeze, and shear modes of deformation in 2D *This aim will be considered complete when 8 sets of silicone membranes are deformed in the three modes of deformation arising from a QR decomposition of the deformation gradient [16], and a 95% confidence interval of the stress-strain curves for the conjugate stress/strain pairs are obtained.*

10 samples of silicone were tested in equibiaxial tension, 10 in uniaxial tension, and 16 in simple shear and the conjugate stress-strain pairs of dilation, squeeze, and shear respectively (arising from the QR decomposition of the deformation gradient F) were extracted from these tests. The 95% confidence intervals of these curves were plotted and showed good consistency,

validating that the experimental error associated with the experimental apparatus was minimal.

Mechanically characterize a biological tissue in 2D with the Freed-Rajagopal model *This aim will be considered complete when stress-strain curves for the three conjugate stress/strain pairs are generated from 8 sets of experiments performed on rat skin, a total of 9 material parameters are obtained in accordance with the Freed-Rajagopal implicit model for elastic biological tissues[16] (from the 95% confidence intervals calculated for these curves), and the model's viability for rat skin is assessed.*

8 samples of rat dorsal skin were tested in equibiaxial tension, 16 in uniaxial tension, and 8 in simple shear, and the dilation, squeeze, and shear stress-strain curves (respectively) were obtained from each test. The Freed-Rajagopal model for planar biological tissues was fitted to the test data and the 3 material parameters (per mode of deformation) and their 95% confidence intervals, were obtained. It was verified that the model fit the data very well in all cases and the utility of the framework and model in mechanical characterization of biological tissues was observed.

Develop a bioreactor that can apply uniaxial stretch on cell-seeded substrates *This aim will be considered complete when a bioreactor capable of applying physiological uniaxial stretches is developed, the biocompatibility of all the components contacting the cells is verified, and NIH 3T3 fibroblasts are seeded on a suitable substrate and cyclically stretched inside the bioreactor for at least 10 hours, with a subsequent live/dead assay to confirm that the bioreactor is cell viable.*

A uniaxial bioreactor was developed and fabricated. The biocompatibility of the components in the bioreactor were verified by performing biocompatibility studies on all the components of the system. NIH 3T3 fibroblasts were seeded on a thin silicone membrane and subjected to cyclical sinusoidal stretching for 12 hours at an amplitude of 5% engineering strain and frequency of 0.5Hz. Live/dead assays were performed after the test and were comparable to the control in terms of cell viability. It was verified that the bioreactor is capable of performing ar-

bitrary physiological displacement profiles. The use of the bioreactor in tissue engineering in conjunction with the theoretical framework studied in this work was discussed.

REFERENCES

[1] A. Khademhosseini and R. Langer, "A decade of progress in tissue engineering," *Nature protocols*, vol. 11, no. 10, p. 1775, 2016.

[2] A. French, "Mechanotransduction," *Annual review of physiology*, vol. 54, no. 1, pp. 135–152, 1992.

[3] L. G. Griffith and G. Naughton, "Tissue engineering–current challenges and expanding opportunities," *science*, vol. 295, no. 5557, pp. 1009–1014, 2002.

[4] C. J. O'Callaghan and B. Williams, "Mechanical strain–induced extracellular matrix production by human vascular smooth muscle cells: Role of tgf-β1," *Hypertension*, vol. 36, no. 3, pp. 319–324, 2000.

[5] Y.-c. Fung, *Biomechanics: mechanical properties of living tissues*. Springer Science & Business Media, 2013.

[6] G. A. Holzapfel, T. C. Gasser, and R. W. Ogden, "Comparison of a multi-layer structural model for arterial walls with a fung-type model, and issues of material stability," *J. Biomech. Eng.*, vol. 126, no. 2, pp. 264–275, 2004.

[7] H. N. Chia and B. M. Wu, "Recent advances in 3d printing of biomaterials," *Journal of biological engineering*, vol. 9, no. 1, p. 4, 2015.

[8] Q. P. Pham, U. Sharma, and A. G. Mikos, "Electrospinning of polymeric nanofibers for tissue engineering applications: a review," *Tissue engineering*, vol. 12, no. 5, pp. 1197–1211, 2006.

[9] S. F. Badylak, D. Taylor, and K. Uygun, "Whole-organ tissue engineering: decellularization and recellularization of three-dimensional matrix scaffolds," *Annual review of biomedical engineering*, vol. 13, pp. 27–53, 2011.

[10] I. M. El-Sherbiny and M. H. Yacoub, "Hydrogel scaffolds for tissue engineering: Progress and challenges," *Global Cardiology Science and Practice*, vol. 2013, no. 3, p. 38, 2013.

[11] D. B. Kolesky, R. L. Truby, A. S. Gladman, T. A. Busbee, K. A. Homan, and J. A. Lewis, "3d bioprinting of vascularized, heterogeneous cell-laden tissue constructs," *Advanced materials*, vol. 26, no. 19, pp. 3124–3130, 2014.

[12] I. Martin, D. Wendt, and M. Heberer, "The role of bioreactors in tissue engineering," *TRENDS in Biotechnology*, vol. 22, no. 2, pp. 80–86, 2004.

[13] J. Zhao, M. Griffin, J. Cai, S. Li, P. E. Bulter, and D. M. Kalaskar, "Bioreactors for tissue engineering: an update," *Biochemical engineering journal*, vol. 109, pp. 268–281, 2016.

[14] A. McLellan, "Finite strain coordinates and the stability of solid phases," *Journal of Physics C: Solid State Physics*, vol. 9, no. 22, p. 4083, 1976.

[15] A. Srinivasa, "On the use of the upper triangular (or qr) decomposition for developing constitutive equations for green-elastic materials," *International Journal of Engineering Science*, vol. 60, pp. 1–12, 2012.

[16] A. Freed, V. Erel, and M. Moreno, "Conjugate stress/strain base pairs for planar analysis of biological tissues," *Journal of Mechanics of Materials and Structures*, vol. 12, no. 2, pp. 219–247, 2016.

[17] K. R. Rajagopal, "On implicit constitutive theories," *Applications of Mathematics*, vol. 48, no. 4, pp. 279–319, 2003.

[18] A. D. Freed and K. Rajagopal, "A promising approach for modeling biological fibers," *Acta Mechanica*, vol. 227, no. 6, pp. 1609–1619, 2016.

[19] A. Freed, *Soft solids*, ch. 4, pp. 94–97. Springer, 2016.

[20] H. Saraf, K. Ramesh, A. Lennon, A. Merkle, and J. Roberts, "Mechanical properties of soft human tissues under dynamic loading," *Journal of biomechanics*, vol. 40, no. 9, pp. 1960–1967, 2007.

[21] M. Jiang, R. L. Sridhar, A. B. Robbins, A. D. Freed, and M. R. Moreno, "A versatile biaxial testing platform for soft tissues," *Journal of the Mechanical Behavior of Biomedical Materials*, vol. 114, p. 104144, 2021.

[22] M. Jiang, Z. T. Lawson, V. Erel, S. Pervere, T. Nan, A. B. Robbins, A. D. Feed, and M. R. Moreno, "Clamping soft biologic tissues for uniaxial tensile testing: A brief survey of current methods and development of a novel clamping mechanism," *Journal of the mechanical behavior of biomedical materials*, vol. 103, p. 103503, 2020.

[23] J. Blaber, B. Adair, and A. Antoniou, "Ncorr: open-source 2d digital image correlation matlab software," *Experimental Mechanics*, vol. 55, no. 6, pp. 1105–1122, 2015.

[24] M. Sacks, "A method for planar biaxial mechanical testing that includes in-plane shear.," *Journal of Biomechanical Engineering*, vol. 121, no. 5, pp. 551–555, 1999.

[25] S. Amensag and P. S. McFetridge, "Tuning scaffold mechanics by laminating native extracellular matrix membranes and effects on early cellular remodeling," *Journal of Biomedical Materials Research Part A*, vol. 102, no. 5, pp. 1325–1333, 2014.

[26] A. B. Robbins, A. D. Freed, and M. R. Moreno, "Characterizing the non-linear mechanical behavior of native and biomimetic engineered tissues in 1d with physically meaningful parameters," *Journal of the Mechanical Behavior of Biomedical Materials*, vol. 102, p. 103509, 2020.

[27] A. D. Freed and K. Rajagopal, "A viscoelastic model for describing the response of biological fibers," *Acta Mechanica*, vol. 227, no. 12, pp. 3367–3380, 2016.

[28] V. Erel and A. D. Freed, "Stress/strain basis pairs for anisotropic materials," *Composites Part B: Engineering*, vol. 120, pp. 152–158, 2017.

[29] J. B. Dixon, S. T. Greiner, A. A. Gashev, G. L. Cote, J. E. Moore Jr, and D. C. Zawieja, "Lymph flow, shear stress, and lymphocyte velocity in rat mesenteric prenodal lymphatics," *Microcirculation*, vol. 13, no. 7, pp. 597–610, 2006.

[30] K. O. Lim and D. R. Boughner, "Mechanical properties of human mitral valve chordae tendineae: variation with size and strain rate," *Canadian journal of physiology and pharmacology*, vol. 53, no. 3, pp. 330–339, 1975.

[31] K.-I. Jang, H. U. Chung, S. Xu, C. H. Lee, H. Luan, J. Jeong, H. Cheng, G.-T. Kim, S. Y. Han, J. W. Lee, *et al.*, "Soft network composite materials with deterministic and bio-inspired designs," *Nature communications*, vol. 6, no. 1, pp. 1–11, 2015.

[32] A. Freed and A. Srinivasa, "Logarithmic strain and its material derivative for a qr decomposition of the deformation gradient," *Acta Mechanica*, vol. 226, no. 8, pp. 2645–2670, 2015.

APPENDIX A

USING THE QR FRAMEWORK IN IMPLICIT ELASTICITY

In the QR framework, the deformation gradient F is decomposed using Gram-Schmidt method to get $F = \mathscr{R}\mathscr{U}$, where the so called Laplace stretch $\mathscr{U}$ represents the distortion, while $\mathscr{U}$ represents the rotation of the material coordinates (Refer [15], [16], and [32] for more details).

$$\mathscr{U} = \begin{bmatrix} a & a\gamma \\ 0 & b \end{bmatrix} \tag{A.1}$$

where a and b are the stretches in the two directions and γ is the shear strain applied on the material. The Laplace stretch can then be decomposed into a product of the three modes $\mathscr{U} = \mathscr{U}^d\mathscr{U}^q\mathscr{U}^s$ as

$$[\mathscr{U}^d][\mathscr{U}^q][\mathscr{U}^s] = \underbrace{\begin{bmatrix} \sqrt{ab} & 0 \\ 0 & \sqrt{ab} \end{bmatrix}}_{dilation} \underbrace{\begin{bmatrix} \sqrt{a/b} & 0 \\ 0 & \sqrt{a/b} \end{bmatrix}}_{squeeze} \underbrace{\begin{bmatrix} 1 & \gamma \\ 0 & 1 \end{bmatrix}}_{shear} = \begin{bmatrix} a & a\gamma \\ 0 & b \end{bmatrix} = [\mathscr{U}] \tag{A.2}$$

Section 4 already discusses using implicit elasticity with the QR framework where material response to all the three modes are considered to be decoupled. Based on personal communication with Dr. Freed, a model where there is a coupling effect between the squeeze and shear responses is recorded here. The elastic compliances for material response in the three modes is as follows:

Dilation

$$\frac{1}{K} = \left(\frac{\delta_t - \delta_1}{K^E\delta_t + \pi/2} + \frac{1}{K^C}\right), \delta_t = \delta - \frac{\pi}{4K^C} \tag{A.3}$$

Squeeze

$$\frac{1}{M} = 2\left(\frac{\varepsilon_t - |\varepsilon_1|}{M^E\varepsilon_t + 2\gamma\tau} + \frac{1}{M^C}\right), \varepsilon_t = \varepsilon - \frac{\sigma - 2\gamma\tau}{M^C} \tag{A.4}$$

Shear

$$\frac{1}{G} = \Gamma\left(\frac{\gamma_t - 2\varepsilon\gamma - |\gamma_1|}{G^E\gamma_t + 2\varepsilon\tau} + \frac{1-2\varepsilon}{G^C}\right), \gamma_t = \gamma - \frac{(1-2\varepsilon)\tau}{G^C} \tag{A.5}$$

Here, $1/K$, $1/M$, and $1/G$ are the compliances in the dilation, squeeze, and shear modes respectively. $\Gamma = a/b$. The subscript "t" denotes transition strain for all three modes. All the other symbols have the same meaning as in Section 4.

APPENDIX B

USING THE QR FRAMEWORK IN NON-LINEAR ELASTICITY

The model used for elastic membranes using explicit elasticity is given by (based on personal communication with Dr. Freed)

$$\begin{Bmatrix} d\pi \\ d\sigma \\ d\tau \end{Bmatrix} = \begin{bmatrix} 4K & 0 & 0 \\ 0 & 2M_\gamma & 2\tau \\ 0 & 2\tau & G_\varepsilon \end{bmatrix} \begin{Bmatrix} d\delta \\ d\varepsilon \\ d\gamma \end{Bmatrix} \tag{B.1}$$

where the areal modulus K, in-plane squeeze modulus M_γ, and the in-plane shear modulus G_ε are defined as

$$K := \frac{1}{4}\frac{\partial \pi}{\partial \delta}, \tag{B.2}$$

$$M_\gamma := \frac{1}{2}\frac{\partial \sigma}{\partial \varepsilon}\Big|_\gamma, \tag{B.3}$$

$$G_\varepsilon := \frac{\partial \tau}{\partial \gamma}\Big|_\varepsilon. \tag{B.4}$$

As in Section 3, $\{\pi,\delta\}$, $\{\sigma,\varepsilon\}$, and $\{\tau,\gamma\}$ are the stress/stress conjugate pairs for dilation, squeeze, and shear respectively.It can be seen from Equations B.3 and B.4 that the in-plane squeeze modulus has to be evaluated at a state of constant shear, and the in-plane shear modulus has to be evaluated at a state of constant squeeze. This requires experiments to be performed where the squeeze response of the material is studied at a variety of constant shear states, and vice versa, to get surfaces for these two moduli. The dilation response is assumed to be decoupled from the non-uniform squeeze and shear modes and can therefore be studied independently.

APPENDIX C

4-BAR SHEAR APPARATUS

The following pages contain the engineering drawings for the novel apparatus discussed in Chapter 2.

REVISION	DESCRIPTION OF CHANGE	APPROVAL
00	Initial Release	
	DCO-0052	

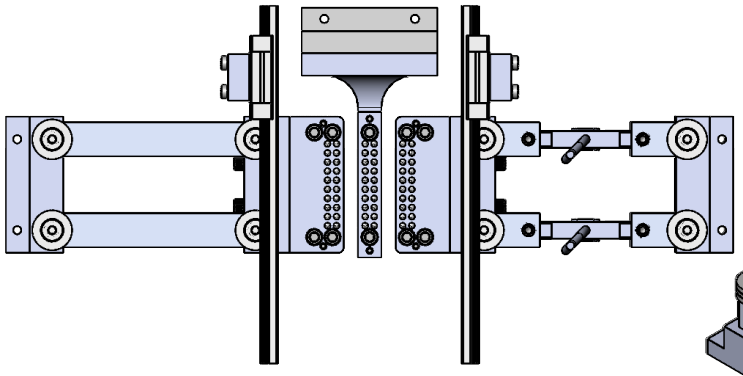

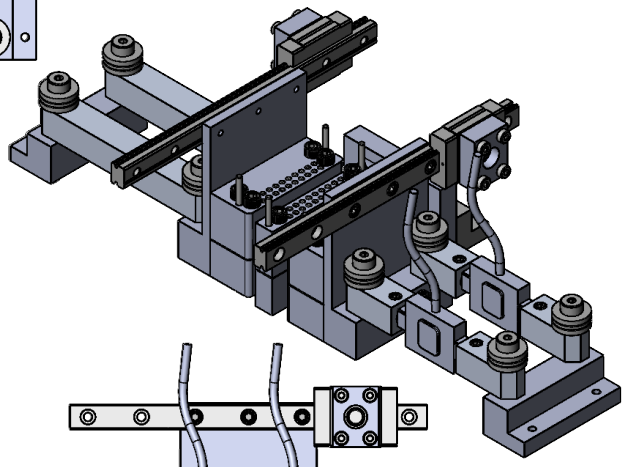

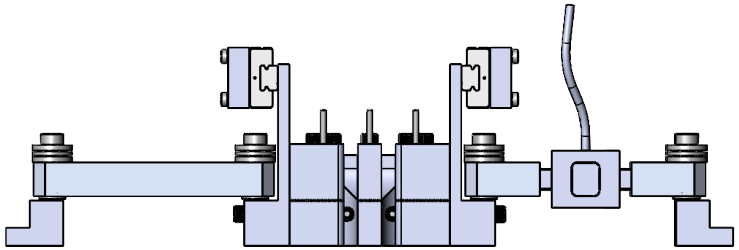

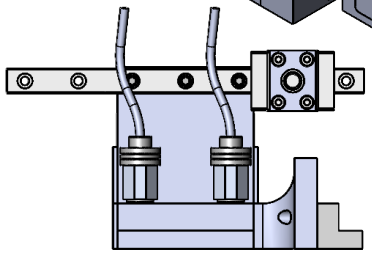

DIMENSIONS ARE IN INCHES
UNLESS OTHERWISE STATED.

TOLERANCES:
FRACTIONAL ± 1/16
ANGULE ± 1 degree
X.X ± 0.1
X.XX ± 0.01
X.XXX ± 0.005
X.XXXX ± 0.0005
CENTIMETER: ± 0.2cm
MILIMETER: ± 0.5mm

BIOMECHANICAL ENVIRONMENTS LABORATORY

DESCRIPTION	BME SPEC NUMBER	
ASSEMBLY 4BarSimpleShearSetUpAssembly	FIX-0069	
DRAWN BY:Raghuveer Lalitha Sridhar	DATE: 11/15/2021	
SCALE: 1:1.5	DO NOT SCALE DRAWING	MATERIAL: N/A

ITEM NO.	DESCRIPTION	QTY.
1	FIX-0060 00	2
2	FIX-0061 00	1
3	FIX-0062 00	1
4	4-40 Socket Head Screw - 5/16" Long	2
5	Jig to Clamp L-Adapter	2
6	4-40 Socket Head Screw - 3/4" Long	4
7	Actuator to Jig L-Adapter	2
8	Futek LSB210 Load Cell	2
9	M3 x 0.5 to 10-32 adpater	4
10	Load Cell Thread Sleeve	4
11	4-bar Link - with Load Cell	4
12	8/32 Set Screw - 1/8" Long	4
13	1/8" ID Thrust Bearing	8
14	4-40 Shoulder Screw 1/8" Dia	8
15	1/8" ID Ball Bearing	8
16	4-bar Link - without Load Cell	2
17	Linear Slide Rail	2
18	2-64 Socket Head Screw - 3/16" Long	6
19	Linear Slide Carriage	2
20	LVDT to Linear Carriage Adapter	2
21	M5 x 0.8 Thin Hex Nut	2
22	M2 x 0.4 Socket Head Screw - 8mm Long	8

REVISION	DESCRIPTION OF CHANGE	APPROVAL
00	Initial Release	
	DCO-0052	

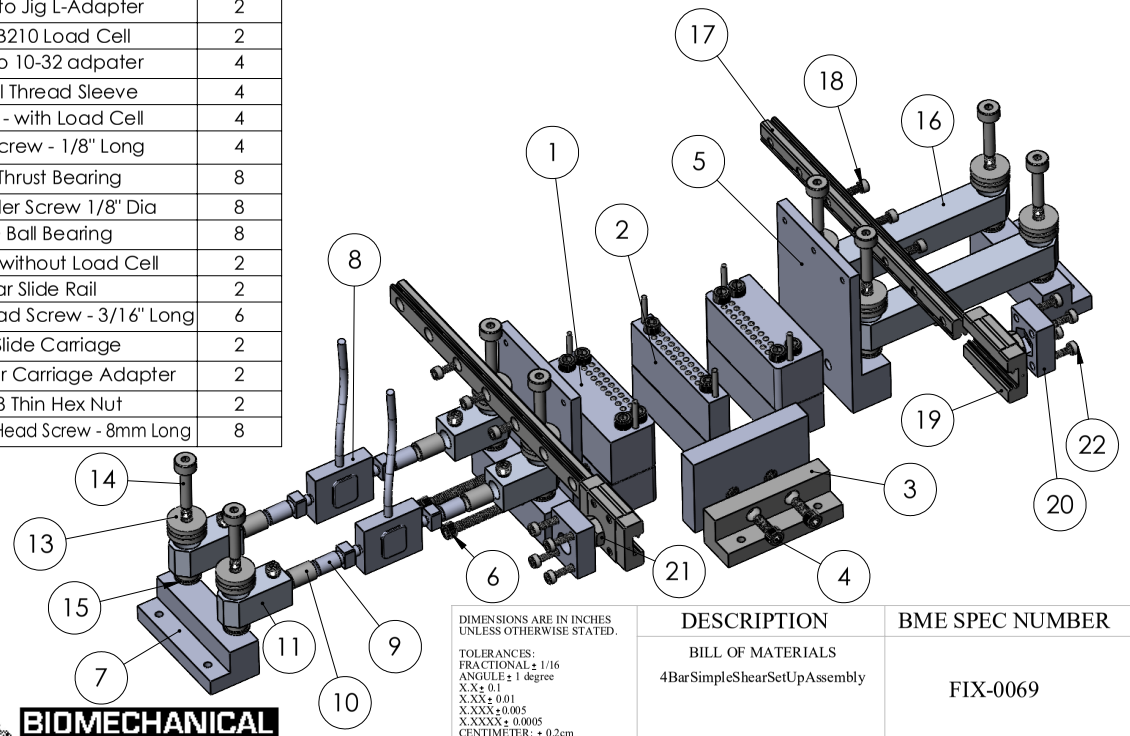

BIOMECHANICAL ENVIRONMENTS LABORATORY

DIMENSIONS ARE IN INCHES UNLESS OTHERWISE STATED.

TOLERANCES:
FRACTIONAL ± 1/16
ANGULE ± 1 degree
X.X ± 0.1
X.XX ± 0.01
X.XXX ± 0.005
X.XXXX ± 0.0005
CENTIMETER: ± 0.2cm
MILIMETER: ± 0.5mm

DESCRIPTION	BME SPEC NUMBER
BILL OF MATERIALS 4BarSimpleShearSetUpAssembly	FIX-0069
DRAWN BY:Raghuveer Lalitha Sridhar	DATE: 11/15/2021
SCALE: 1:1.5 DO NOT SCALE DRAWING	MATERIAL: N/A

REVISION	DESCRIPTION OF CHANGE	APPROVAL
00	Initial Release	
	DCO-0052	

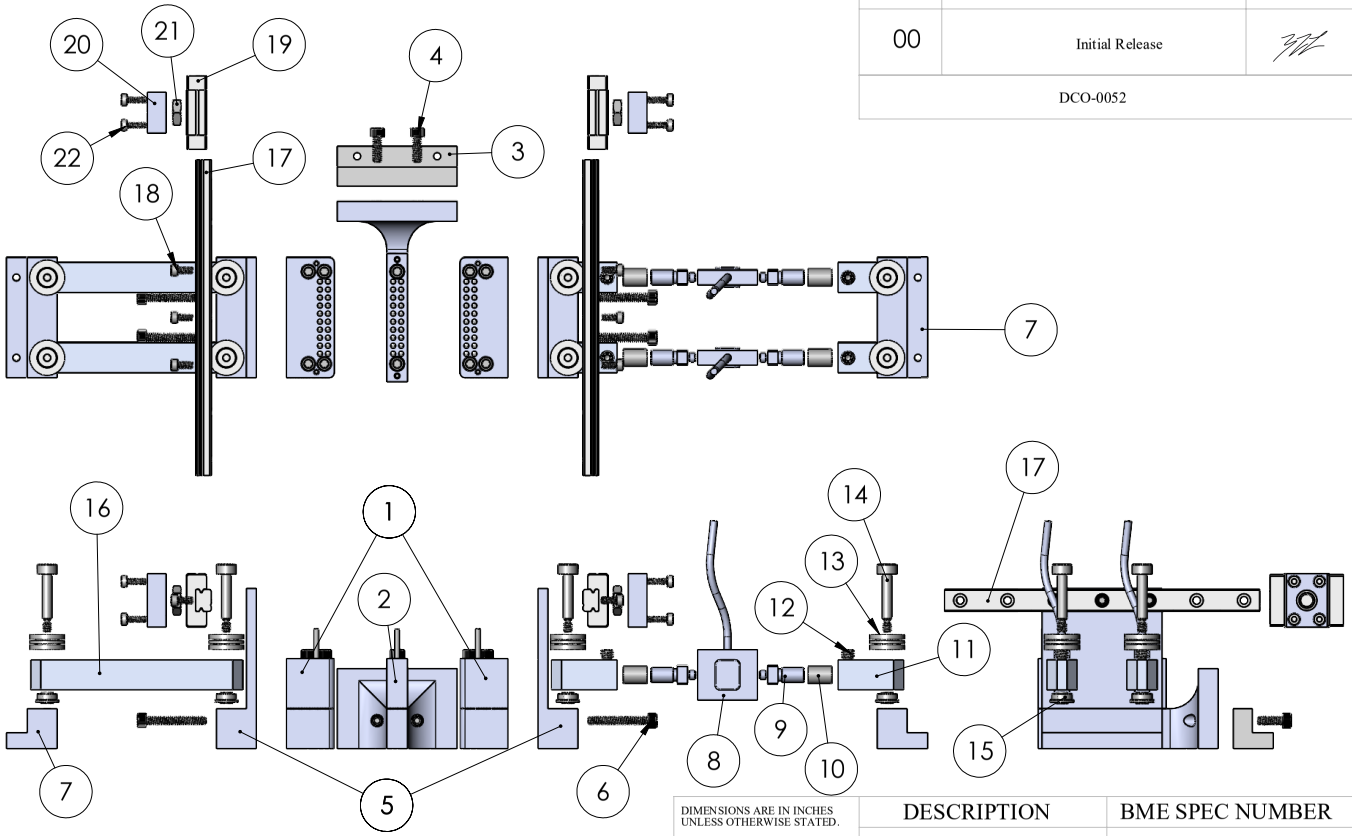

DIMENSIONS ARE IN INCHES
UNLESS OTHERWISE STATED.

TOLERANCES:
FRACTIONAL ± 1/16
ANGLE ± 1 degree
X.X ± 0.1
X.XX ± 0.01
X.XXX ± 0.005
X.XXXX ± 0.0005
CENTIMETER: ± 0.2cm
MILIMETER: ± 0.5mm

BIOMECHANICAL ENVIRONMENTS LABORATORY

DESCRIPTION	BME SPEC NUMBER
EXPLODED ASSEMBLY 4BarSimpleShearSetUpAssembly	FIX-0069
DRAWN BY:Raghuveer Lalitha Sridhar	DATE: 11/15/2021
SCALE: 1:1.7 DO NOT SCALE DRAWING	MATERIAL: N/A

Sheet: 3 of 22

REVISION	DESCRIPTION OF CHANGE	APPROVAL
00	Initial Release	
DCO-0052		

REPRESENTATIVE PURPOSES ONLY
MCMASTER-CARR #92196A107

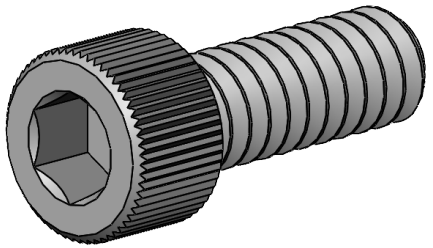

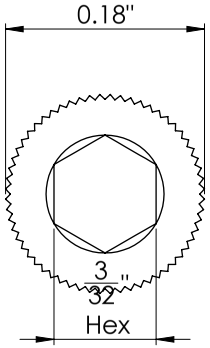

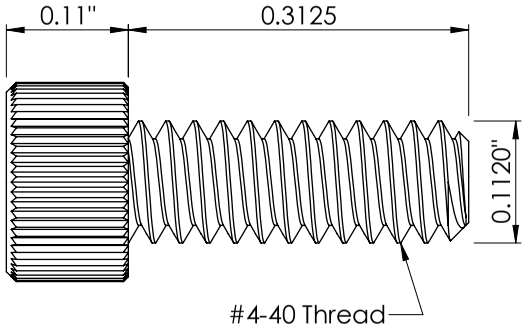

DIMENSIONS ARE IN INCHES UNLESS OTHERWISE STATED.

TOLERANCES:
FRACTIONAL ± 1/16
ANGULE ± 1 degree
X.X ± 0.1
X.XX ± 0.01
X.XXX ± 0.005
X.XXXX ± 0.0005
CENTIMETER: ± 0.2cm
MILIMETER: ± 0.5mm

DESCRIPTION	BME SPEC NUMBER
4-40 SCREW - 5/16" 92196A107_18-8 STAINLESS STEEL SOCKET HEAD SCREW	FIX-0069
DRAWN BY:Raghuveer Lalitha Sridhar	DATE: 11/15/2021
DO NOT SCALE DRAWING	MATERIAL: 18-8 Stainless Steel

SCALE: 8:1

Sheet:4 of 22

BIOMECHANICAL ENVIRONMENTS LABORATORY

REVISION	DESCRIPTION OF CHANGE	APPROVAL
00	Initial Release	
DCO-0052		

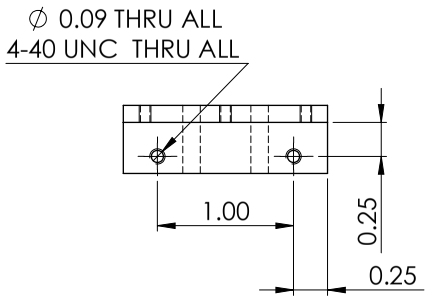

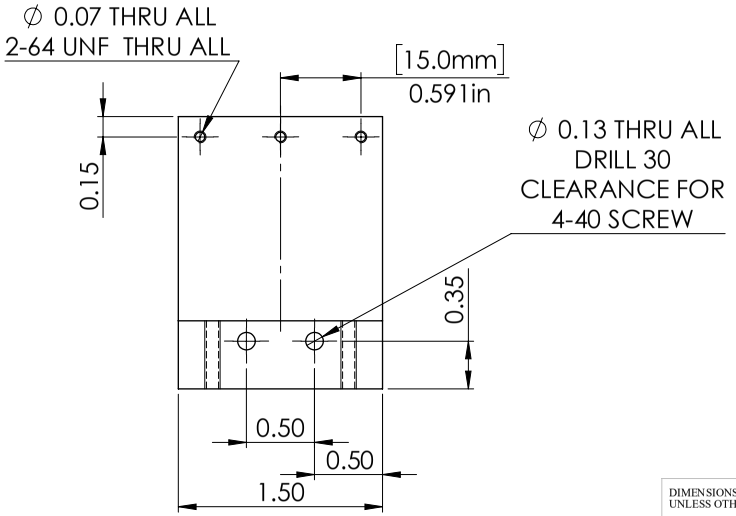

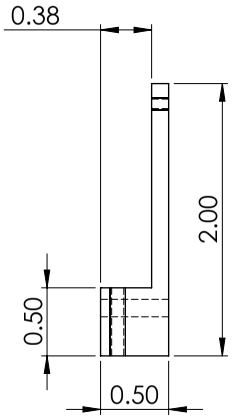

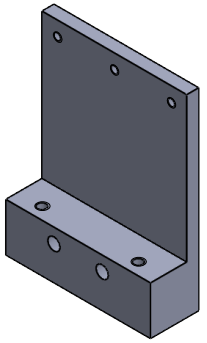

BIOMECHANICAL ENVIRONMENTS LABORATORY

DIMENSIONS ARE IN INCHES UNLESS OTHERWISE STATED.	DESCRIPTION	BME SPEC NUMBER
TOLERANCES: FRACTIONAL ± 1/16 ANGLE ± 1 degree X.X ± 0.1 X.XX ± 0.01 X.XXX ± 0.005 X.XXXX ± 0.0005 CENTIMETER: ± 0.2cm MILIMETER: ± 0.5mm	JIG TO CLAMP L-ADAPTER ActuatorToJigLAdapter	FIX-0069
	DRAWN BY:Raghuveer Lalitha Sridhar	DATE: 11/15/2021
SCALE: 1:1	DO NOT SCALE DRAWING	MATERIAL: Aluminium 6061

REVISION	DESCRIPTION OF CHANGE	APPROVAL
00	Initial Release	
DCO-0052		

REPRESENTATIVE PURPOSES ONLY
MCMASTER-CARR #92196A133

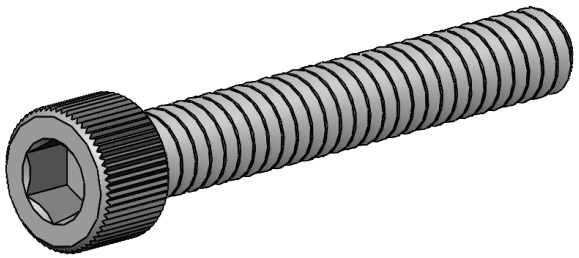

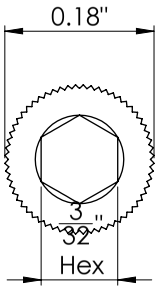

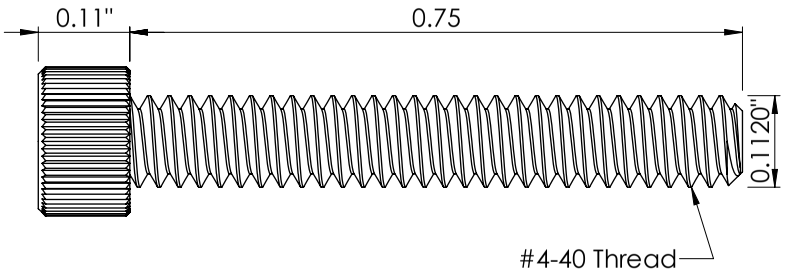

DIMENSIONS ARE IN INCHES UNLESS OTHERWISE STATED.	DESCRIPTION	BME SPEC NUMBER
TOLERANCES: FRACTIONAL ± 1/16 ANGLE ± 1 degree X.X ± 0.1 X.XX ± 0.01 X.XXX ± 0.005 X.XXXX ± 0.0005 CENTIMETER: ± 0.2cm MILIMETER: ± 0.5mm	4-40 SCREW - 3/4" 92196A113_18-8 STAINLESS STEEL SOCKET HEAD SCREW	FIX-0069
	DRAWN BY:Raghuveer Lalitha Sridhar	DATE: 11/15/2021
SCALE: 6:1	DO NOT SCALE DRAWING	MATERIAL: 18-8 Stainless Steel Sheet:6 of 22

BIOMECHANICAL ENVIRONMENTS LABORATORY

REVISION	DESCRIPTION OF CHANGE	APPROVAL
00	Initial Release	
	DCO-0052	

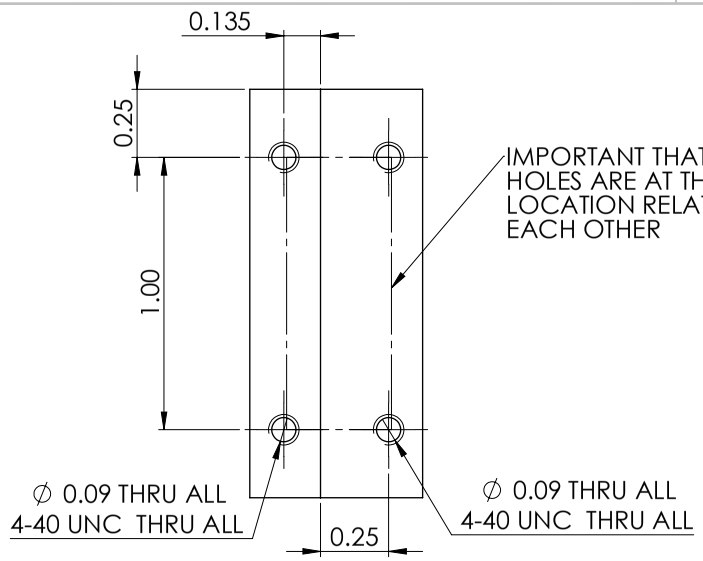

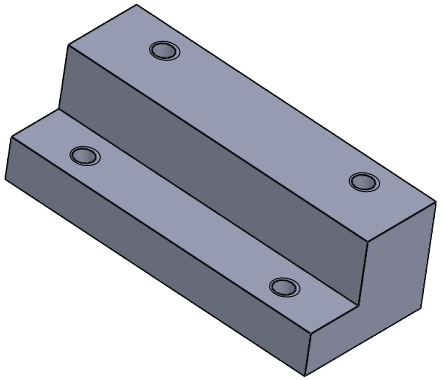

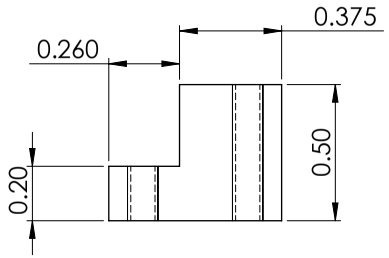

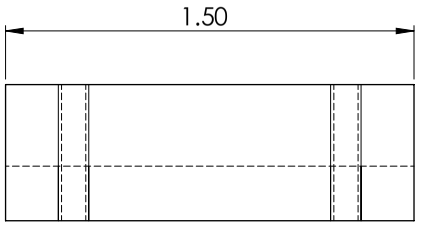

DIMENSIONS ARE IN INCHES UNLESS OTHERWISE STATED.

TOLERANCES:
FRACTIONAL ± 1/16
ANGULE ± 1 degree
X.X ± 0.1
X.XX ± 0.01
X.XXX ± 0.005
X.XXXX ± 0.0005
CENTIMETER: ± 0.2cm
MILIMETER: ± 0.5mm

DESCRIPTION	BME SPEC NUMBER
ACTUATOR TO JIG L-ADAPTER ActuatorToJigLAdapter	FIX-0069
DRAWN BY:Raghuveer Lalitha Sridhar	DATE: 11/15/2021
SCALE: 2:1	DO NOT SCALE DRAWING
MATERIAL: Aluminium 6061	Sheet: 7 of 22

BIOMECHANICAL ENVIRONMENTS LABORATORY

REVISION	DESCRIPTION OF CHANGE	APPROVAL
00	Initial Release	
DCO-0052		

REPRESENTATIVE PURPOSES ONLY

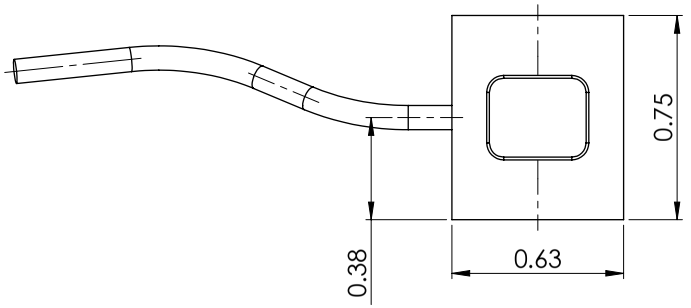

FUTEK ADVANCED SENSOR TECHNOLOGY INC
MODEL LSB210
EITHER THE 10LB OR THE 100LB MODEL MAY BE USED

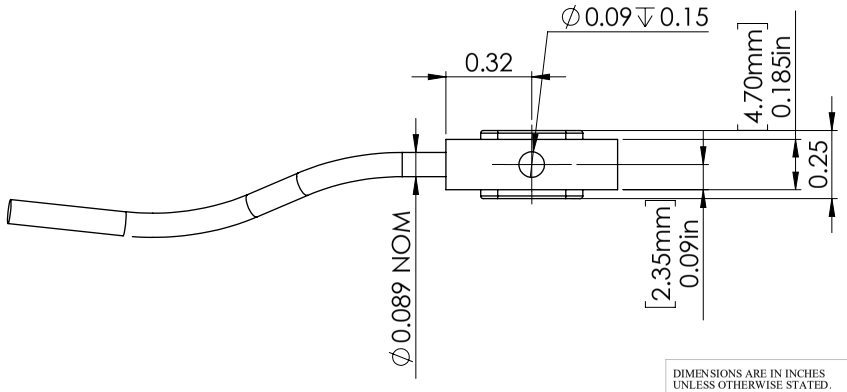

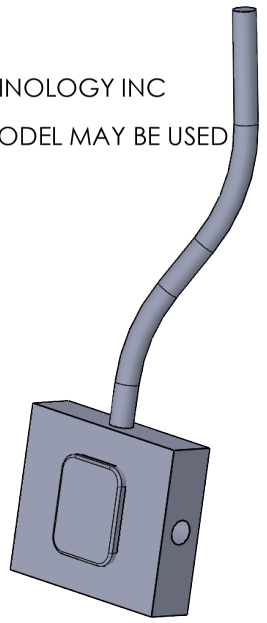

DIMENSIONS ARE IN INCHES
UNLESS OTHERWISE STATED.

TOLERANCES:
FRACTIONAL ± 1/16
ANGULE ± 1 degree
X.X ± 0.1
X.XX ± 0.01
X.XXX ± 0.005
X.XXXX ± 0.0005
CENTIMETER: ± 0.2cm
MILIMETER: ± 0.5mm

BIOMECHANICAL ENVIRONMENTS LABORATORY

DESCRIPTION	BME SPEC NUMBER
FUTEK LSB210 LOAD CELL Futek - LSB210 Submersible Jr. Miniature S-Beam Load Cell	FIX-0069
DRAWN BY:Raghuveer Lalitha Sridhar	DATE: 11/15/2021
SCALE: 2:1 / DO NOT SCALE DRAWING	MATERIAL: N/A / Sheet:8 of 22

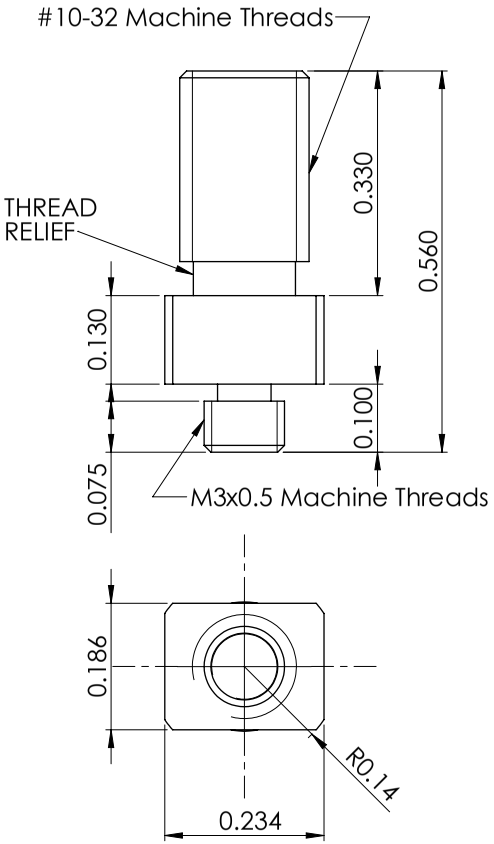

REVISION	DESCRIPTION OF CHANGE	APPROVAL
00	Initial Release	
DCO-0052		

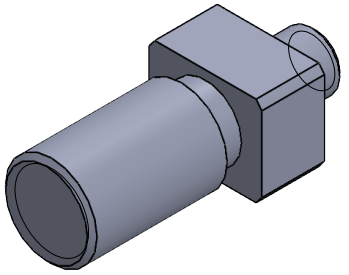

FOR REFERENCE PURPOSES ONLY
FUTEK ADVANCED SENSOR TECHNOLOGIES INC
LSB210 LOAD CELL ACCESSORY
MODEL NUMBER: MCP02498
M3 X 0.5 TO 10-32 MALE THREAD ADAPTER

BIOMECHANICAL ENVIRONMENTS LABORATORY

DIMENSIONS ARE IN INCHES UNLESS OTHERWISE STATED. TOLERANCES: FRACTIONAL ± 1/16 ANGULE ± 1 degree X.X ± 0.1 X.XX ± 0.01 X.XXX ± 0.005 X.XXXX ± 0.0005 CENTIMETER: ± 0.2cm MILIMETER: ± 0.5mm	DESCRIPTION	BME SPEC NUMBER
	M3 X 0.5 TO 10-32 ADAPTER Futek - LSB210 Adapter 10-32 MCP02498	FIX-0069
	DRAWN BY:Raghuveer Lalitha Sridhar	DATE: 11/15/2021
SCALE: 5:1	DO NOT SCALE DRAWING	MATERIAL: 303 SS Cold Drawn

REVISION	DESCRIPTION OF CHANGE	APPROVAL
00	Initial Release	
DCO-0052		

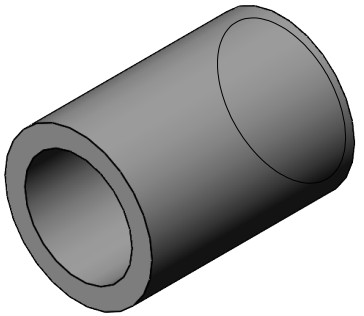

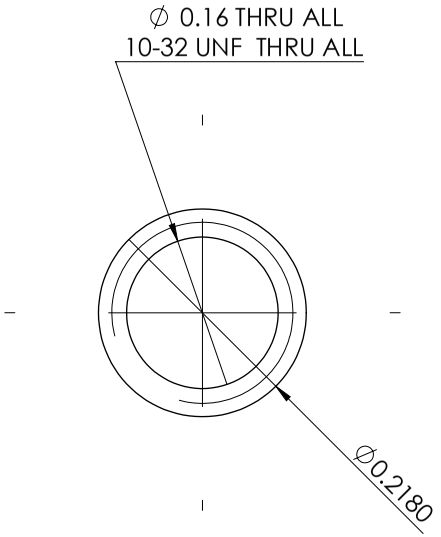

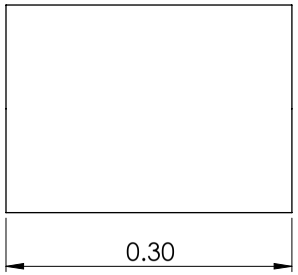

DIMENSIONS ARE IN INCHES
UNLESS OTHERWISE STATED.

TOLERANCES:
FRACTIONAL ± 1/16
ANGLE ± 1 degree
X.X ± 0.1
X.XX ± 0.01
X.XXX ± 0.005
X.XXXX ± 0.0005
CENTIMETER: ± 0.2cm
MILIMETER: ± 0.5mm

DESCRIPTION	BME SPEC NUMBER
LOAD CELL THREAD SLEEVE LoadCellThreadSleeve	FIX-0069
DRAWN BY:Raghuveer Lalitha Sridhar	DATE: 11/15/2021
SCALE: 7:1	DO NOT SCALE DRAWING	MATERIAL: Stainless Steel	Sheet: 10

BIOMECHANICAL ENVIRONMENTS LABORATORY

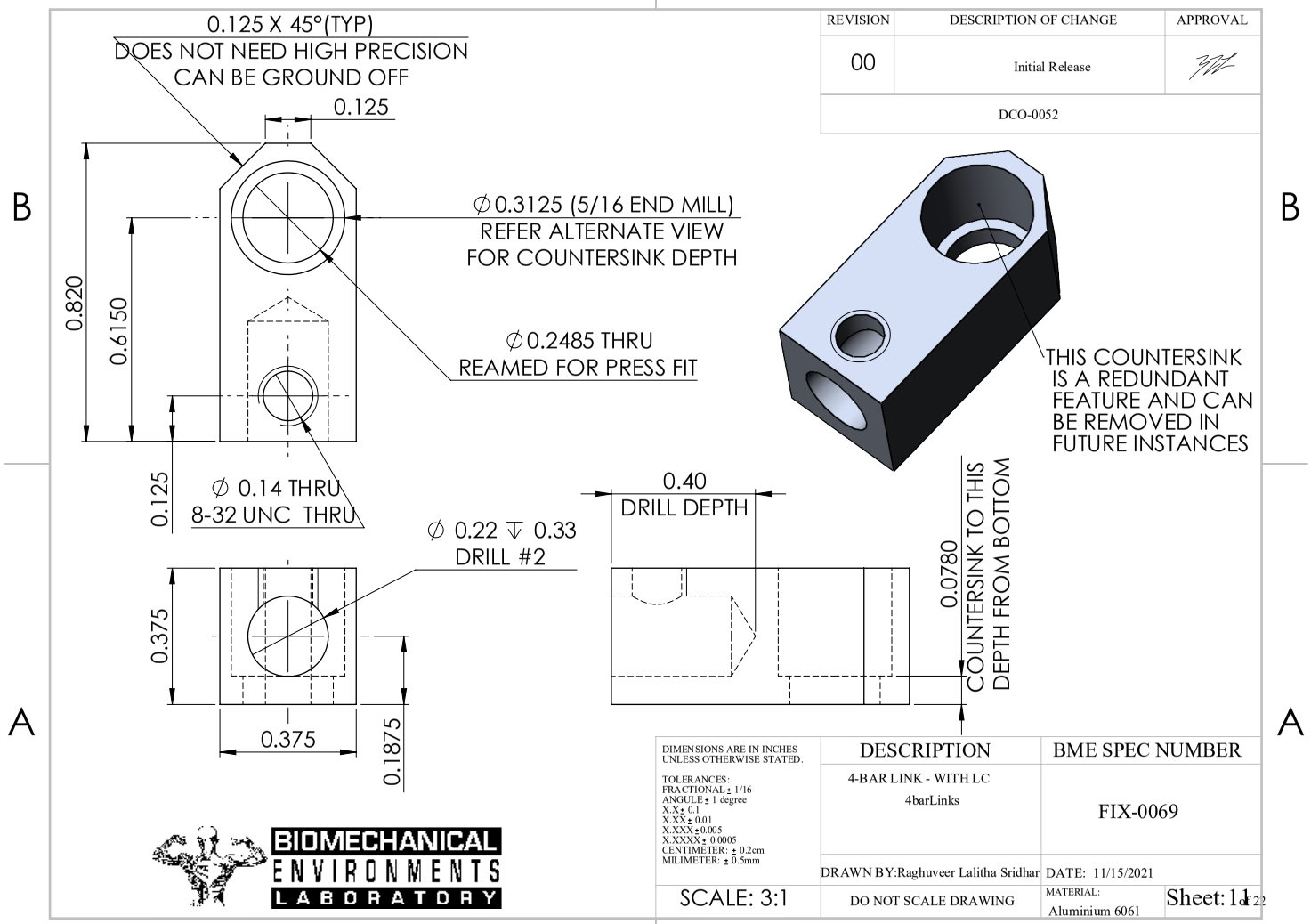

REVISION	DESCRIPTION OF CHANGE	APPROVAL
00	Initial Release	
DCO-0052		

REPRESENTATIVE PURPOSES ONLY
MCMASTER-CARR #92311A188

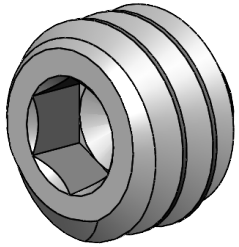

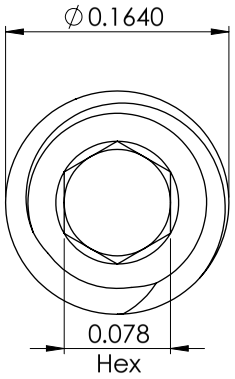

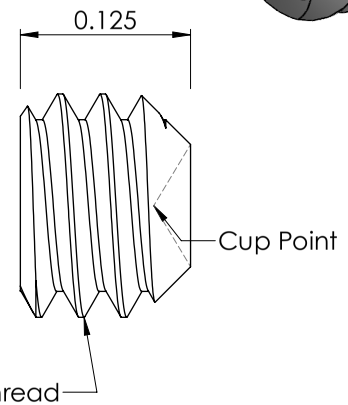

DIMENSIONS ARE IN INCHES UNLESS OTHERWISE STATED.

TOLERANCES:
FRACTIONAL ± 1/16
ANGLE ± 1 degree
X.X ± 0.1
X.XX ± 0.01
X.XXX ± 0.005
X.XXXX ± 0.0005
CENTIMETER: ± 0.2cm
MILIMETER: ± 0.5mm

BIOMECHANICAL ENVIRONMENTS LABORATORY

DESCRIPTION	BME SPEC NUMBER
8-32 SET SCREW - 1/8" 92311A188_18-8 SS CUP POINT SET SCREW	FIX-0069
DRAWN BY:Raghuveer Lalitha Sridhar	DATE: 11/15/2021
DO NOT SCALE DRAWING	MATERIAL: 18-8 Stainless Steel

SCALE: 10:1

Sheet:12 of 22

REVISION	DESCRIPTION OF CHANGE	APPROVAL
00	Initial Release	
	DCO-0052	

REPRESENTATIVE PURPOSES ONLY
MCMASTER-CARR #6655K310

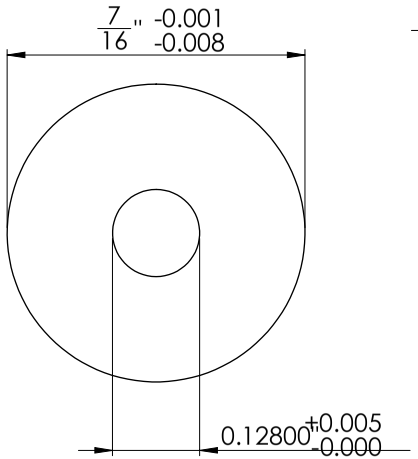

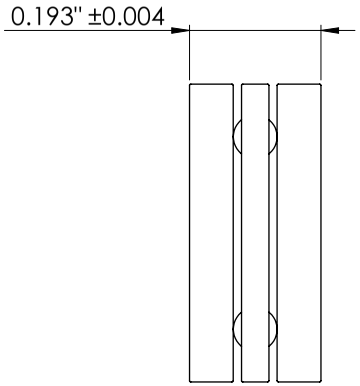

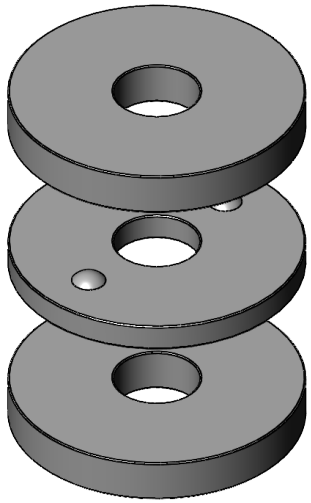

DIMENSIONS ARE IN INCHES UNLESS OTHERWISE STATED.

TOLERANCES:
FRACTIONAL ± 1/16
ANGLE ± 1 degree
X.X ± 0.1
X.XX ± 0.01
X.XXX ± 0.005
X.XXXX ± 0.0005
CENTIMETER: ± 0.2cm
MILIMETER: ± 0.5mm

BIOMECHANICAL ENVIRONMENTS LABORATORY

DESCRIPTION	BME SPEC NUMBER
1/8" ID THRUST BEARING 6655K310_PLASTIC THRUST BALL BEARING	FIX-0069
DRAWN BY:Raghuveer Lalitha Sridhar	DATE: 11/15/2021
SCALE: 5:1 DO NOT SCALE DRAWING	MATERIAL: Multiple

REVISION	DESCRIPTION OF CHANGE	APPROVAL
00	Initial Release	
DCO-0052		

REPRESENTATIVE PURPOSES ONLY
MCMASTER-CARR #94035A135

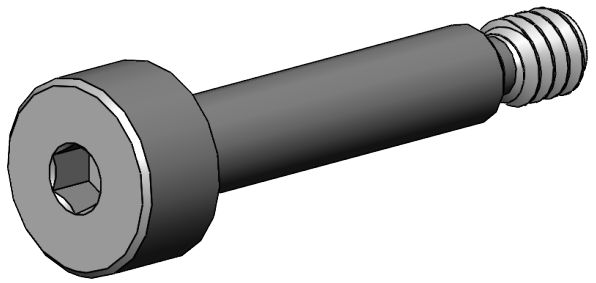

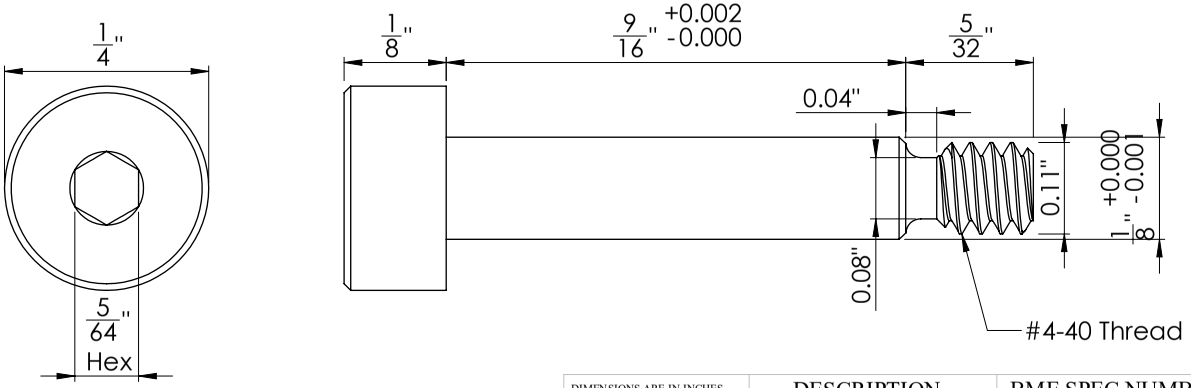

DIMENSIONS ARE IN INCHES UNLESS OTHERWISE STATED.

TOLERANCES:
FRACTIONAL ± 1/16
ANGLE ± 1 degree
X.X ± 0.1
X.XX ± 0.01
X.XXX ± 0.005
X.XXXX ± 0.0005
CENTIMETER: ± 0.2cm
MILIMETER: ± 0.5mm

DESCRIPTION	BME SPEC NUMBER
4-40 SHOULDER SCREW - 9/16" 94035A135_18-8 STAINLESS STEEL PRECISION SHOULDER SCREW	FIX-0069
DRAWN BY:Raghuveer Lalitha Sridhar	DATE: 11/15/2021
SCALE: 6:1 DO NOT SCALE DRAWING	MATERIAL: 18-8 Stainless Steel Sheet:14 of 22

BIOMECHANICAL ENVIRONMENTS LABORATORY

REVISION	DESCRIPTION OF CHANGE	APPROVAL
00	Initial Release	
DCO-0052		

REPRESENTATIVE PURPOSES ONLY
MCMASTER-CARR #57155k329

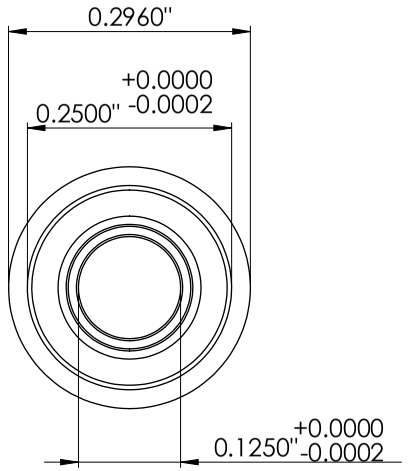

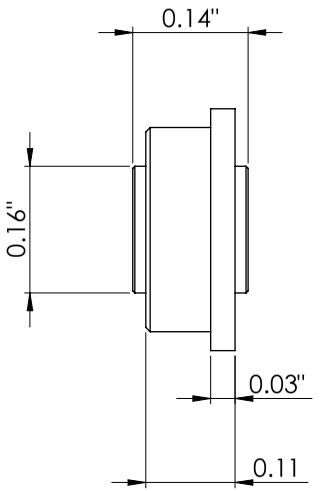

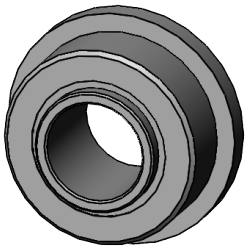

Trade Number: R144-2Z

DIMENSIONS ARE IN INCHES UNLESS OTHERWISE STATED.	DESCRIPTION	BME SPEC NUMBER
TOLERANCES: FRACTIONAL ± 1/16 ANGLE ± 1 degree X.X ± 0.1 X.XX ± 0.01 X.XXX ± 0.005 X.XXXX ± 0.0005 CENTIMETER: ± 0.2cm MILIMETER: ± 0.5mm	1/8" ID BALL BEARING 57155K329_STAINLESS STEEL BALL BEARING	FIX-0069
	DRAWN BY:Raghuveer Lalitha Sridhar	DATE: 11/15/2021
SCALE: 6:1	DO NOT SCALE DRAWING	MATERIAL: Stainless Steel

BIOMECHANICAL ENVIRONMENTS LABORATORY

REVISION	DESCRIPTION OF CHANGE	APPROVAL
00	Initial Release	
DCO-0052		

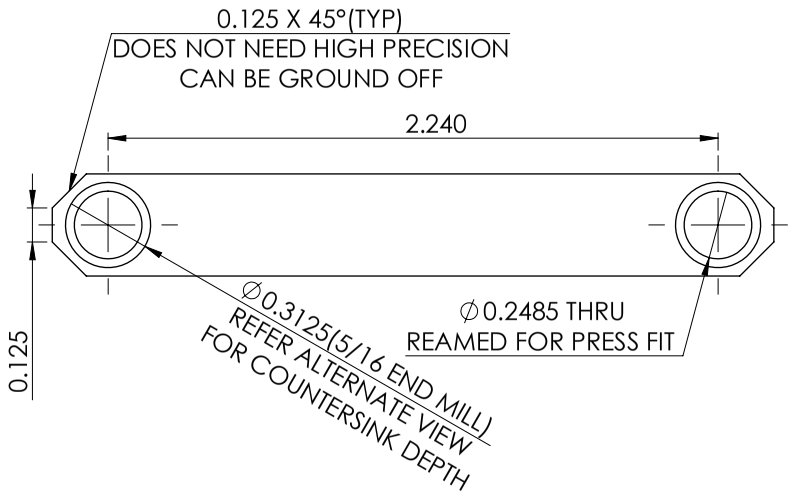

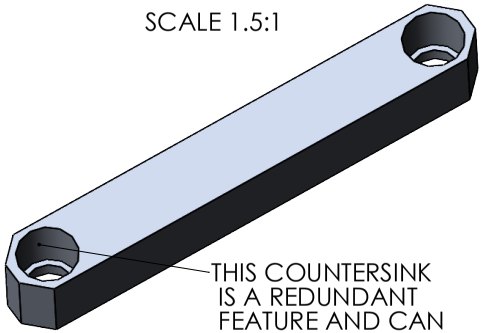

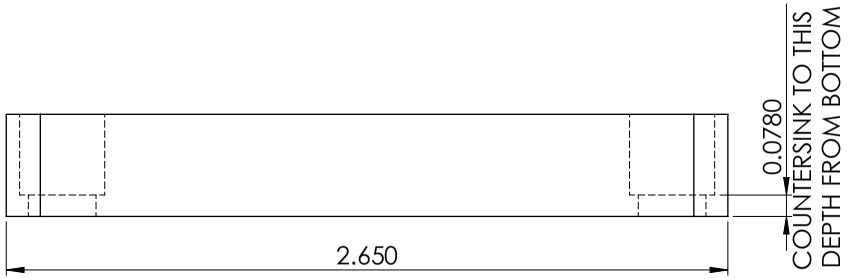

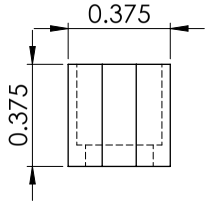

DIMENSIONS ARE IN INCHES
UNLESS OTHERWISE STATED.

TOLERANCES:
FRACTIONAL ± 1/16
ANGLE ± 1 degree
X.X ± 0.1
X.XX ± 0.01
X.XXX ± 0.005
X.XXXX ± 0.0005
CENTIMETER: ± 0.2cm
MILIMETER: ± 0.5mm

DESCRIPTION	BME SPEC NUMBER
4-BAR LINK - WITHOUT LC 4barLinks	FIX-0069
DRAWN BY:Raghuveer Lalitha Sridhar	DATE: 11/15/2021
SCALE: 2:1 / DO NOT SCALE DRAWING	MATERIAL: Aluminium 6061 / Sheet: 16 of 22

BIOMECHANICAL ENVIRONMENTS LABORATORY

REVISION	DESCRIPTION OF CHANGE	APPROVAL
00	Initial Release	
	DCO-0052	

REPRESENTATIVE PURPOSES ONLY

ORIGINAL PART FOR THIS FIXTURE WAS PURCHASED FROM AMAZON
CNC INC - MODEL MGN7C
MCMASTER-CARR #6725K33 HAS FUNCTIONALLY IDENTICAL DIMENSIONS AND MAY ALSO BE USED
DRAWING AND CAD FILE WERE MODIFIED FROM MCMASTER-CARR PART
ONLY DIFFERENCES BETWEEN MCMASTER-CARR AND CNC INC PARTS ARE:

1. LENGTH OF THE RAIL IS 100MM FOR CNC INC, 90MM OR 120MM FOR MCMASTER-CARR
2. THE DISTANCE BETWEEN THE FIRST MOUNTING HOLE AND THE EDGE OF THE RAIL IS
    1. 5MM FOR THE CNC INC PART
    2. 7.5MM FOR THE MCMASTER-CARR PART

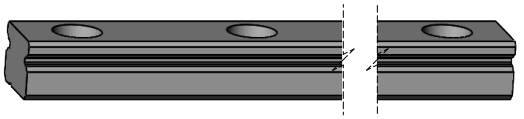

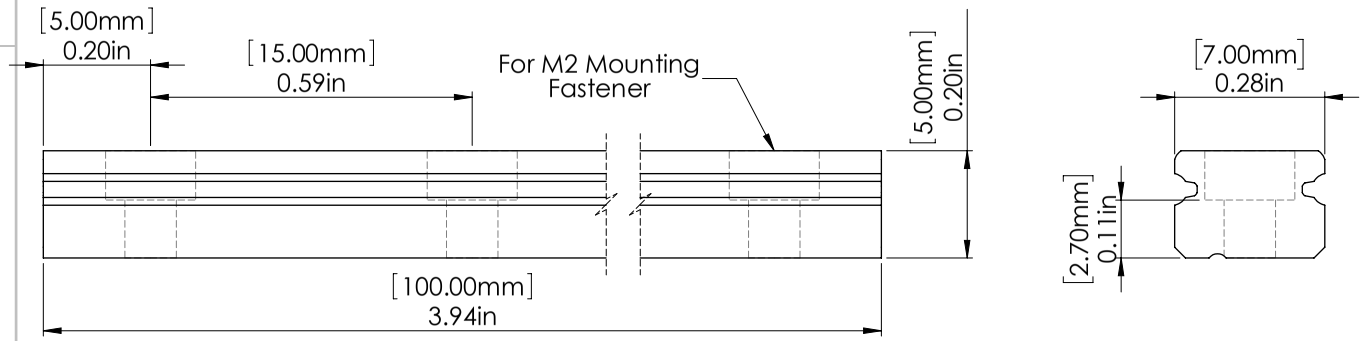

DIMENSIONS ARE IN INCHES UNLESS OTHERWISE STATED.

TOLERANCES:
FRACTIONAL ± 1/16
ANGLE ± 1 degree
X.X ± 0.1
X.XX ± 0.01
X.XXX ± 0.005
X.XXXX ± 0.0005
CENTIMETER: ± 0.2cm
MILIMETER: ± 0.5mm

BIOMECHANICAL ENVIRONMENTS LABORATORY

DESCRIPTION	BME SPEC NUMBER	
LINEAR SLIDE RAIL 7m Wide Linear Guide Rail for Ball Bearing Carriage	FIX-0069	
DRAWN BY:Raghuveer Lalitha Sridhar	DATE: 11/15/2021	
SCALE: 4:1	DO NOT SCALE DRAWING	MATERIAL: 440 Stainless Steel

REVISION	DESCRIPTION OF CHANGE	APPROVAL
00	Initial Release	
DCO-0052		

REPRESENTATIVE PURPOSES ONLY
MCMASTER-CARR #92196A099

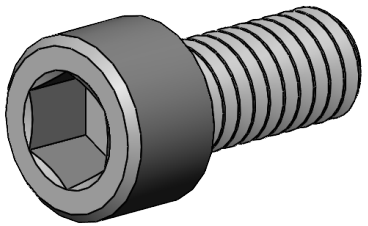

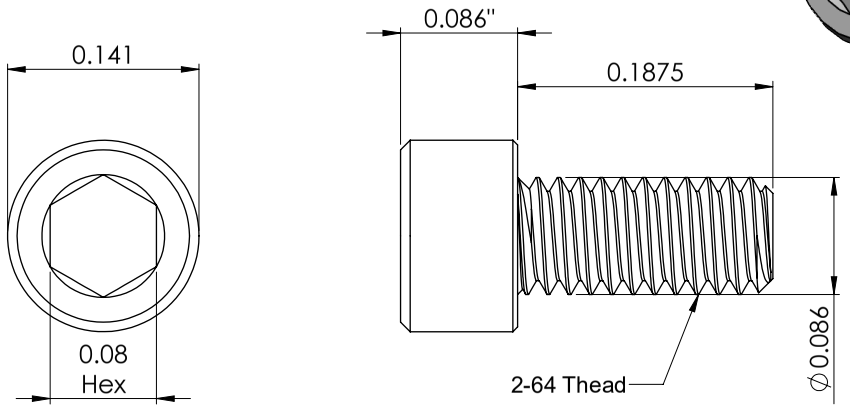

DIMENSIONS ARE IN INCHES
UNLESS OTHERWISE STATED.

TOLERANCES:
FRACTIONAL ± 1/16
ANGULE ± 1 degree
X.X ± 0.1
X.XX ± 0.01
X.XXX ± 0.005
X.XXXX ± 0.0005
CENTIMETER: ± 0.2cm
MILIMETER: ± 0.5mm

BIOMECHANICAL ENVIRONMENTS LABORATORY

DESCRIPTION	BME SPEC NUMBER
2-64 SCREW - 3/16" 92196A099_18-8 STAINLESS STEEL SOCKET HEAD SCREW	FIX-0069
DRAWN BY:Raghuveer Lalitha Sridhar	DATE: 11/15/2021
SCALE: 10:1 DO NOT SCALE DRAWING	MATERIAL: 18-8 Stainless Steel Sheet:18 of 22

REVISION	DESCRIPTION OF CHANGE	APPROVAL
00	Initial Release	
DCO-0052		

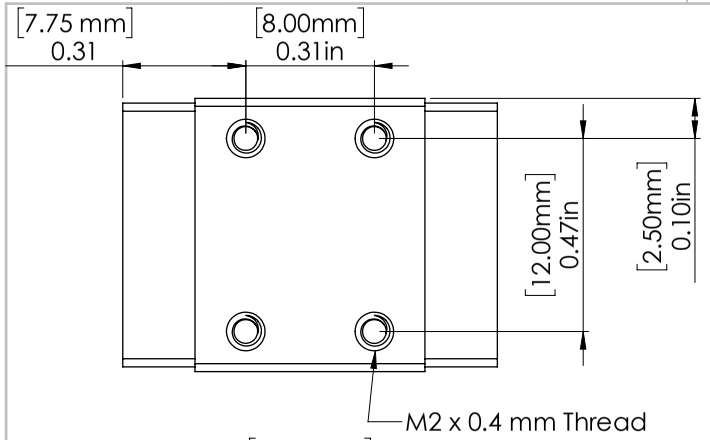

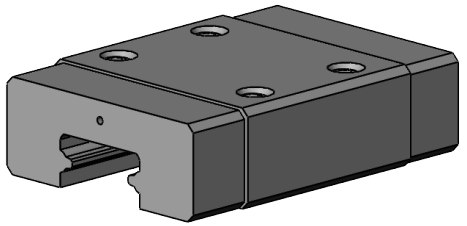

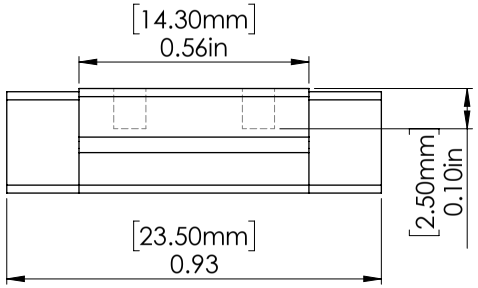

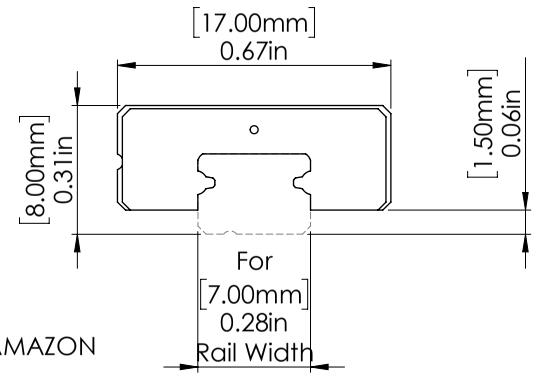

REPRESENTATIVE PURPOSES ONLY
ORIGINAL PART FOR THIS FIXTURE WAS PURCHASED FROM AMAZON
CNC INC - MODEL MGN7C
MCMASTER-CARR #8438K2 HAS IDENTICALDIMENSIONS
AND MAY ALSO BE USED
DRAWING AND CAD FILE FROM MCMASTER-CARR PART

BIOMECHANICAL ENVIRONMENTS LABORATORY

DIMENSIONS ARE IN INCHES UNLESS OTHERWISE STATED.

TOLERANCES:
FRACTIONAL ± 1/16
ANGULE ± 1 degree
X.X ± 0.1
X.XX ± 0.01
X.XXX ± 0.005
X.XXXX ± 0.0005
CENTIMETER: ± 0.2cm
MILIMETER: ± 0.5mm

DESCRIPTION	BME SPEC NUMBER
LINEAR SLIDE CARRIAGE Ball Bearing Carriage for 7mm Wide Guide Rail	FIX-0069
DRAWN BY:Raghuveer Lalitha Sridhar	DATE: 11/15/2021
SCALE: 3:1 DO NOT SCALE DRAWING	MATERIAL: 440 Stainless Steel

PREFERRED MANUFACTURING METHOD: FILAMENT FDM PRINTING

REVISION	DESCRIPTION OF CHANGE	APPROVAL
00	Initial Release	
DCO-0052		

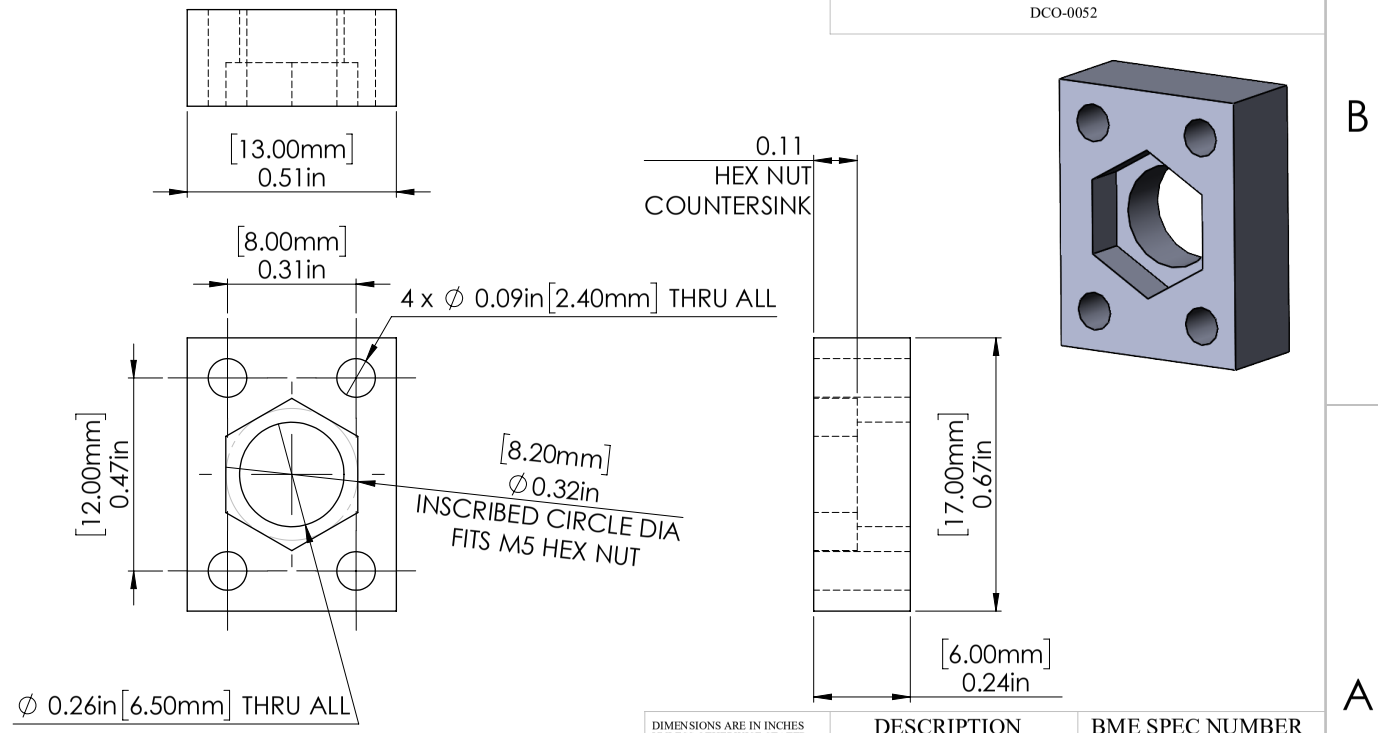

DIMENSIONS ARE IN INCHES UNLESS OTHERWISE STATED.	DESCRIPTION	BME SPEC NUMBER
TOLERANCES: FRACTIONAL ± 1/16 ANGULE ± 1 degree X.X ± 0.1 X.XX ± 0.01 X.XXX ± 0.005 X.XXXX ± 0.0005 CENTIMETER: ± 0.2cm MILIMETER: ± 0.5mm	LVDT TO LINEAR CARRRIAGE LinearCarriageToLVDTAdapter	FIX-0069
	DRAWN BY:Raghuveer Lalitha Sridhar	DATE: 11/15/2021
SCALE: 3:1	DO NOT SCALE DRAWING	MATERIAL: ABS or PLA

BIOMECHANICAL ENVIRONMENTS LABORATORY

Sheet:20 of 22

REVISION	DESCRIPTION OF CHANGE	APPROVAL
00	Initial Release	
	DCO-0052	

REPRESENTATIVE PURPOSES ONLY
MCMASTER-CARR #90710A037

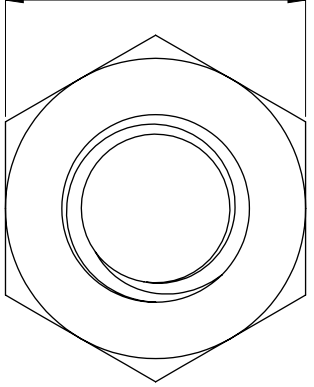

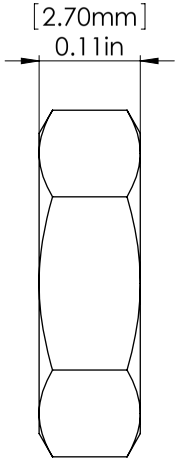

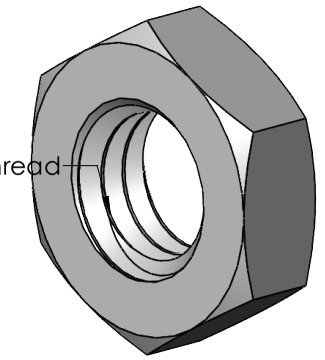

BIOMECHANICAL ENVIRONMENTS LABORATORY

DIMENSIONS ARE IN INCHES UNLESS OTHERWISE STATED. TOLERANCES: FRACTIONAL ± 1/16 ANGLE ± 1 degree X.X ± 0.1 X.XX ± 0.01 X.XXX ± 0.005 X.XXXX ± 0.0005 CENTIMETER: ± 0.2cm MILIMETER: ± 0.5mm	DESCRIPTION M5 X 0.8 THIN HEX NUT 90710A037_TYPE 18-8 SS THIN HEX NUT - DIN 439B	BME SPEC NUMBER FIX-0069
	DRAWN BY:Raghuveer Lalitha Sridhar	DATE: 11/15/2021
SCALE: 7:1	DO NOT SCALE DRAWING	MATERIAL: 18-8 Stainless Steel Sheet:21 of 22

REVISION	DESCRIPTION OF CHANGE	APPROVAL
00	Initial Release	
	DCO-0052	

REPRESENTATIVE PURPOSES ONLY
MCMASTER-CARR #91292A832

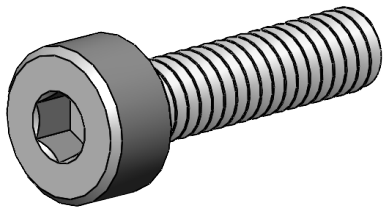

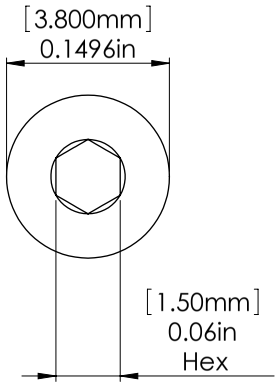

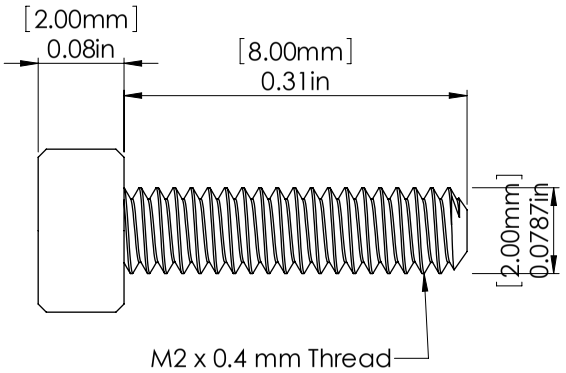

BIOMECHANICAL ENVIRONMENTS LABORATORY

DIMENSIONS ARE IN INCHES UNLESS OTHERWISE STATED. TOLERANCES: FRACTIONAL ± 1/16 ANGLE ± 1 degree X.X ± 0.1 X.XX ± 0.01 X.XXX ± 0.005 X.XXXX ± 0.0005 CENTIMETER: ± 0.2cm MILIMETER: ± 0.5mm	DESCRIPTION	BME SPEC NUMBER	
	M2 X 0.4 SCREW - 8mm 91292A832_TYPE 18-8 SS SOCKET HEAD CAP SCREW	FIX-0069	
	DRAWN BY:Raghuveer Lalitha Sridhar	DATE: 11/15/2021	
SCALE: 8:1	DO NOT SCALE DRAWING	MATERIAL: 18-8 Stainless Steel	Sheet:22 of 22